UCONN LIBRARY

University of Connecticut
OpenCommons@UConn

Doctoral Dissertations | University of Connecticut Graduate School

8-21-2015

I. Rules of Macrocycle Topology: a [13]-Macrodilactone Case Study II. A Cardiac Glycoside Activities Link the Ion-transport Function of Na+/K+ ATPase to Breast Cancer Migration Via Correlative SAR

Anniefer N. Magpusao
anniefer.magpusao@uconn.edu

Follow this and additional works at: https://opencommons.uconn.edu/dissertations

Recommended Citation
Magpusao, Anniefer N., "I. Rules of Macrocycle Topology: a [13]-Macrodilactone Case Study II. A Cardiac Glycoside Activities Link the Ion-transport Function of Na+/K+ ATPase to Breast Cancer Migration Via Correlative SAR" (2015). *Doctoral Dissertations*. 906.
https://opencommons.uconn.edu/dissertations/906

I. Rules of Macrocycle Topology: a [13]-Macrodilactone Case Study

II. A Cardiac Glycoside Activities Link the Ion-transport Function of Na^+/K^+ ATPase to Breast Cancer Migration Via Correlative SAR

Anniefer Magpusao, Ph.D

University of Connecticut, 2015

The overall structure of macrocycles is intimately linked to its biological activities and chemical reactivities. Delineating the factors that control the macrocycle structure will be very useful in developing novel probes, therapeutics and chemical transformations. Using a systematic strategy with the [13]-macrodilactones as model system and a combinational of X-ray crystallography and computational methods, a general model that explains the effect of stereogenic elements (stereogenic centers and stereogenic plane) on the overall structure (planar chirality, shape and topology) of the [13]-macrodilactone was constructed. A specific geometrical arrangement in the stereogenic centers set the planar chirality (either p*S* or p*R*), shape (either ribbon or alternate) and consequently, the overall topology of substituted [13]-macrodilactones. This specific geometrical arrangement is fundamentally governed by the preference of the substituents to be in pseudo-equatorial position. The general model constructed has useful implications in synthesizing macrocycles with designed structural properties and in optimizing the biological and pharmacological activities of bioactive macrocycles.

The cardiac glycosides ouabain and digitoxin, established Na^+/K^+ ATPase inhibitors, were found to inhibit MDA-MB-231 breast cancer cell migration through an

unbiased chemical genetics screen for cell motility. The Na^+/K^+ ATPase acts both as an ion-transporter and as a receptor for cardiac glycosides. To delineate which function is related to breast cancer cell migration, structure–activity relationship (SAR) profiles of cardiac glycosides were established at the cellular (cell migration inhibition), molecular (Na^+/K^+ ATPase inhibition), and atomic (computational docking) levels. Correlation of SAR profiles across these assays established links between cellular activity and specific protein–small molecule interactions. The antimigratory effect in MDA-MB-231 breast cancer cells are directly related to the inhibition of Na^+/K^+ transport. Specifically, the orientation of cardiac glycosides at the putative cation permeation path correlates with the Na^+ pump activity and cell migration. Other Na^+/K^+ ATPase inhibitors that are structurally distinct from cardiac glycosides also exhibit antimigratory activity, corroborating the conclusion that the antiport function of Na^+/K^+ ATPase and not the receptor function is important for supporting the motility of MDA-MB-231 breast cancer cells. Correlative SAR can establish new relationships between specific biochemical functions and higher-level cellular processes.

I. Rules of Macrocycle Topology: a [13]-Macrodilactone Case Study

II. A Cardiac Glycoside Activities Link the Ion-transport Function of Na^+/K^+ ATPase to Breast Cancer Migration Via Correlative SAR

Anniefer Magpusao

A Dissertation

Submitted in Partial Fulfillment of the

Requirements for the Degree of

Doctor of Philosophy

at the

University of Connecticut

2015

Copyright © by

Anniefer Magpusao

2015

Approval Page

Doctor of Philosophy Dissertation

I. Rules of Macrocycle Topology: a [13]-Macrodilactone Case Study

II. A Cardiac Glycoside Activities Link the Ion-transport Function of Na^+/K^+ ATPase to Breast Cancer Migration Via Correlative SAR

Presented by

Anniefer Magpusao

Major Advisor _____

Dr. Mark W. Peczuh

Associate Advisor _____

Dr. Xudong Yao

Associate Advisor _____

Dr. Alfredo Angeles-Boza

University of Connecticut

2015

Acknowledgements

My sincerest gratitude to my advisor, mentor and sensei, Dr. Mark W. Peczuh, for his exceptional guidance through out my training as a chemical biologist. His unbelievable patience, valuable insights and kind heart allowed me to hear and explore my own voice as a scientist. Who I currently am and who I will be as a scientist and as a person is a strong testament of his teaching philosophies. I will forever be indebted to this man, who I greatly admire for being both a talented scientist and an incredible human being.

I am also very thankful for my committee. To Dr. Yao and Dr. Angeles-Boza, for taking the time to write a recommendation letter for me and to Dr. Brueckner for his valuable insights on the macrocycle project. To my former advisor, Dr. Gabriel Fenteany, with whom I learned a lot about chemical biology, thank you.

The people I met and worked with have tremendously enriched my graduate school experience and for that, I will always be thankful. To the former PZ lab members: Jaideep, Rich, Chris and Debjani and to the current PZ lab members: Raghu, Aditya, Zach, JM and Kelli – these guys are some of the kindest and most helpful people I have worked with. I specially would like to thank JM and Kelli for all their help in the macrocycle project. I am grateful for the chance to work with the former Fenteany lab members: Anwar, Christian, Matt, Junru and Nick. I am very thankful as well to the collaborators I worked with in all of my projects: George and Dr. Gascon for the cardiac glycoside project, Trevor and Brandon for the macrocycle project. The most fun I had in graduate school are the moments I shared with friends I met at UConn. I am sincerely thankful to Christian, Joan, Daben, Gill, Inus, Kaddie and Ken.

One of the most fulfilling experiences I had in graduate school is the opportunity to mentor undergraduate students. Being able to contribute in helping students recognize their potential and watch them grow as a scientist is an experience that I sincerely find very fulfilling. With that, I would like to thank my previous undergraduate students: Shannon and Jenaya, for all their help in the screening project; Josh for his contributions in the cardiac glycoside project; John, for his help in the carbohydrate-fused [13]-macrodilactone project and Katie, for a fun summer research on [13]-macrodilactones.

Sometimes, my imagination takes me to a dark place that blurs my perception of the beauty of life. I am forever indebted to ‘the men’: PZ, Anwar, Fred and Patrick, who helped me breathe a little easier when I’m drowning in my own thoughts. You have been the light in my life.

I would like to extend my sincerest gratitude to my parents and family, who have been my infinite source of love, support and inspiration.

Finally, my deepest gratitude to Patrick Taylor for his unconditional love and support. For someone who knows me more than I know my self and believes in me when I fail to see my own worth, I can’t thank you enough. I’m looking forward to spending my life with you.

Table of contents

List of Figures

List of Figures

List of Figures

List of Figures

List of Tables

List of Schemes

Chapter 1

Rules of macrocycle topology: a [13]-macrodilactone case study

1.1 Introduction

Macrocyles – cyclic molecules of 12 or more atoms – have a staggering array of structural diversity and biological activities (Fig. 1-1). Ring size can range from 12 to 50+ atoms with chemical composition that can vary from simple repeating units (i.e. ether linkages and amides) to complex combinations of various functional groups (alkenes, carbonyls, ethers etc.) in the ring and substituents. This huge structural diversity (both natural product and synthetic) is reflected to the wide-range of biological activities (anticancer, antibiotic, antifungal, antiparasitic, antiviral, immunomodulatory) that macrocycles can modulate as well as the enormous protein families it can target with disparate mechanisms of action. As evidenced by the long-standing history of the utility of natural product and synthetic macrocyles as drugs and their unique ability to modulate various biological activities, macrocycles hold real promise for developing new chemical probes and novel therapeutics[1].

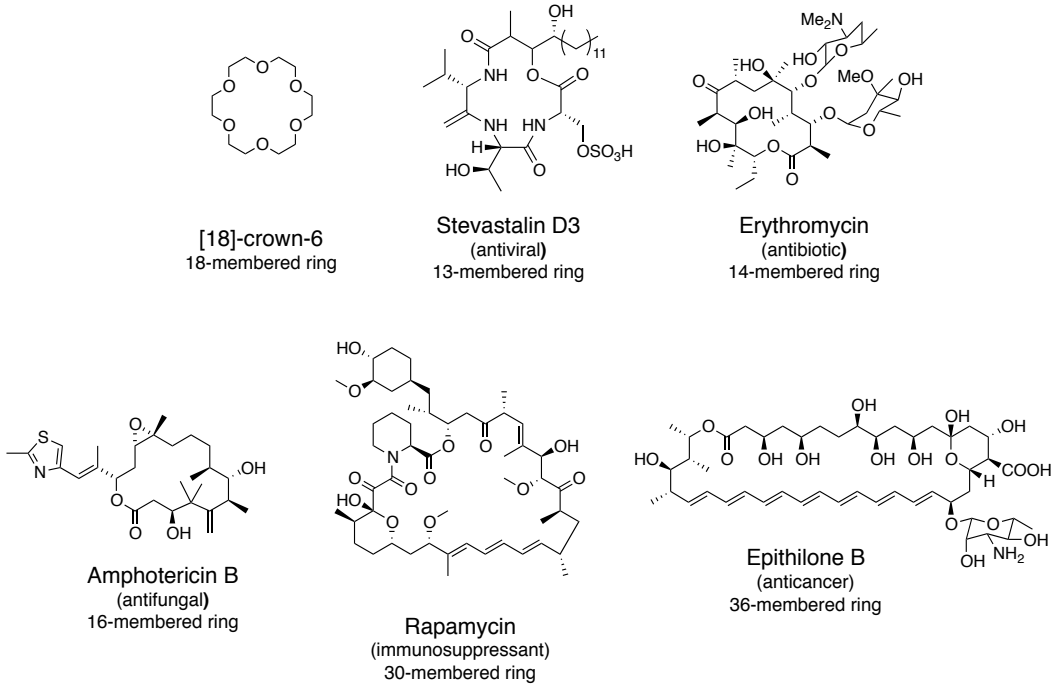

Fig. 1-1. Examples of macrocycles

1.2 Macrocycle and its unique chemical space

As a direct consequence of the lower number of freely rotatable bonds, the macrocyclic ring provides a high degree of conformational pre-organization - one of the unique and key structural features of macrocycles. With respect to target engagement of biologically active macrocyles, the conformational pre-organization of the ring can be used to strategically orient pharmacophoric groups[3] and limit conformational entropy loss upon target binding[4]. This results in higher affinity and better selectivity towards specific members of a protein family or even between different isozymes. Macrocycles also display drug-like physicochemical and pharmacokinetic properties despite deviating from conventional rules of drug-likeness. The next few paragraphs explain how conformational pre-organization brought about by macrocyclization can generate ligand efficient molecules with enhanced biological and pharmacokinetic properties.

1.2.1 The effect of macrocyclization on potency

Conformational pre-organization that results from macrocyclization can improve the potency of acyclic molecules primarily through limitation of the entropic penalty of forming an inhibitor-protein complex. A molecule needs to adopt a specific conformation to successfully bind to a protein. Both acyclic and cyclic molecules can adopt such a bioactive conformation and thus the difference in the enthalpic contribution to binding is relatively small. However, in contrast to acyclic molecules, macrocyles have a limited number of conformations (due to restricted internal bond rotation) and thus have lower entropic penalties when

changing from unbound to bound state. This contributes to a higher affinity and better potency. One compelling example of the effect on potency enhancement of macrocyclization is the macrocyclization of an acyclic small molecule **1-1** – a close analog of an inhibitor of farnesyltransferase that is in clinical trial as an anticancer drug[5] (Fig. 1-2). Using transfer nuclear Overhouser effect (trNOE) NMR, it was observed to be in a folded conformation, which suggests that macrocyclization, might be beneficial for improving its potency. Indeed, the cyclized analog **1-3** is 20-fold more potent than the lead **1-1** and impressively 55,000-fold more potent than its direct acyclic counterpart **1-2**.

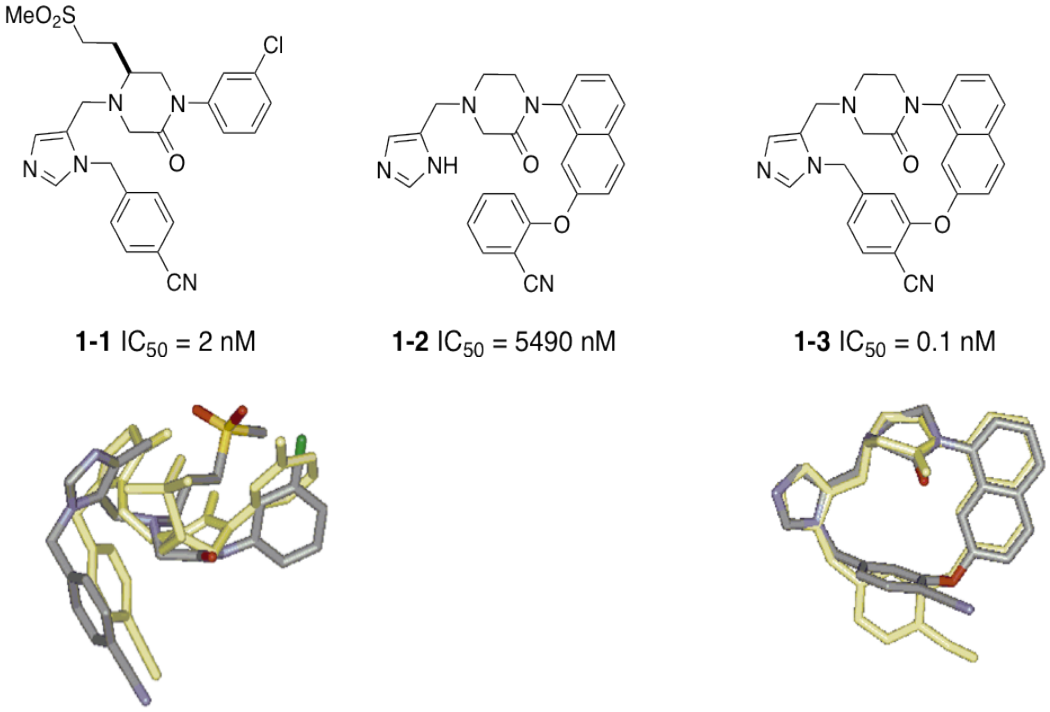

1-1 IC_{50} = 2 nM **1-2** IC_{50} = 5490 nM **1-3** IC_{50} = 0.1 nM

Fig. 1-2. Improving potency through macrocyclization. Two lowest energy conformations of **1-1** (lower left), consistent with trNOE NMR structure of its complex with farnesyttransferase, showed it exist in folded form. Rigidification through macrocyclization (lower right) greatly improved its potency where the macrocycle **1-3** is 50,000-fold more potent than its direct acyclic counterpart **1-2**. The two figures for the macrocycle conformation were reused with permission.

1.2.2 The effect of macrocyclization on selectivity

Besides improvement in potency, macrocyclization can also vary the selectivity profiles of acyclic molecules by fixing or at least reducing the number of target-specific conformations. By taking advantage of the small difference in binding site topology between specific members of a protein family or between various isozymes[6], an enhancement in selectivity can be obtained by using the macrocyclic ring as a scaffold to strategically orient pharmacophoric functionalities at specific three-dimensional locations. A great example is the development of selective kinase inihibitors (Fig. 1-3)[7], one of the most challenging goals in drug discovery. The notoriously non-selective pan ATPase inihibitors staurosporine **1-4** and rebeccamycin **1-5** can be made selective by disrupting the planarity of indolocarbazole lactam ring system - the key pharmacophore of kinase inhibitors which acts as a mimic of ATP adenine ring. By breaking the central aromatic ring and controlling the kinase inhibitor's conformation using various ring size, Warriner and colleagues developed selective kinase inhibitors with a C2-symmetric *anti* conformation **1-6 (**selective towards cAMP-dependent protein kinase/ protein kinase G/ protein kinase C (AGC) group of protein kinases such as PKCs) and distorted *syn* conformation **1-7** (selective towards GSK3β)[7].

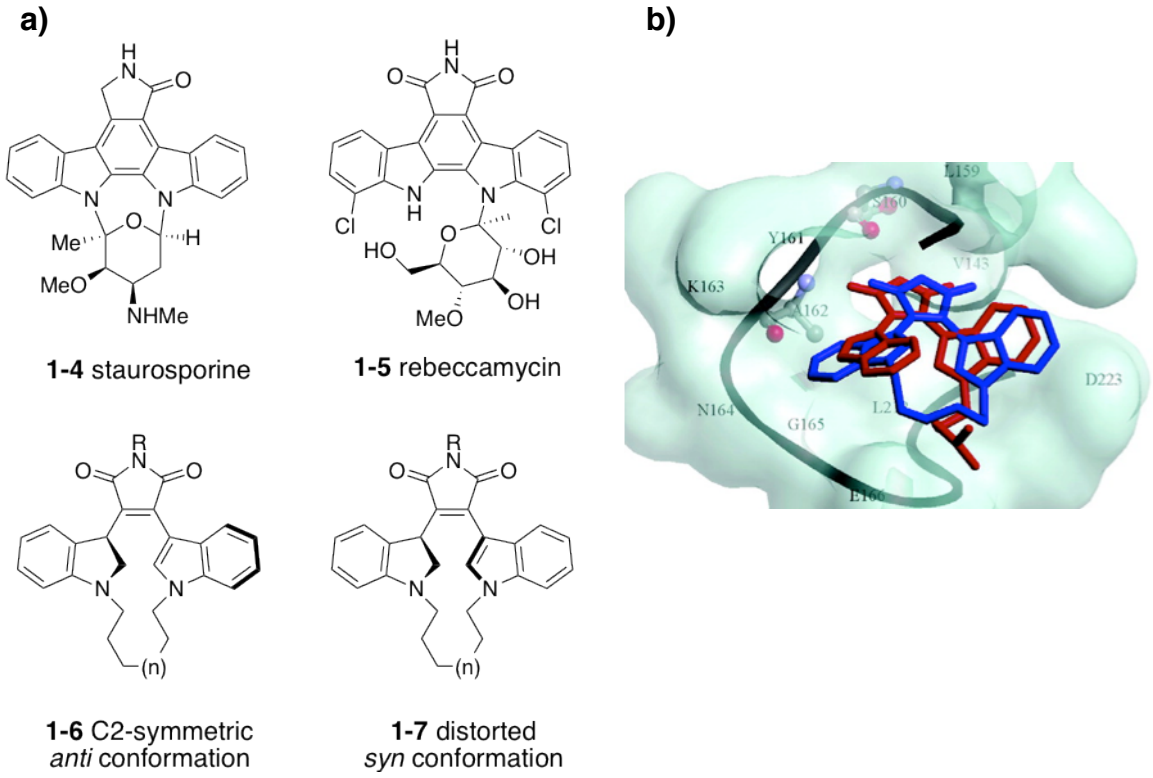

Fig. 1-3. Improving selectivity and controlling small molecule conformation through macrocyclization. (**a**) Pan ATPase inhitors staurosporine **1-4** and rebeccamycin **1-5** were made selective through macrocyclization. Ring size controls the ratio of *anti* **1-6** and *syn* **1-7** conformations, which then controls its selectivity towards specific members of kinases. (**b**) Docked complex formed by a protein kinase with inhibitors in various conformations showing how fine-tuning of macrocyclic conformation can allow access to selective inhibitors. The macrocycle-protein complex was reused with permission.

1.2.3 Improving pharmacological and pharmacokinetic properties through macrocyclization

Since poor membrane permeability and metabolic instability are primarily due to conformational flexibility, restricting the conformational landscape and fine-tuning the orientation of H-bonding functionalities can significantly enhance

the pharmacological and pharmacokinetic properties of bioactive molecules. As an example, for diasteromeric cyclic peptides **1-8** and **1-9** (Fig. 1-4), the most permeable diastereomer **1-8** adopts a pseudo-symmetric conformation with internally satisfied hydrogen bonds while the less permeable diastereomer **1-9** adopts a twisted conformation with some H-bonding groups oriented toward the solvent[8]. This demonstrates the effect of macrocyclic conformation in membrane permeability where molecules that can adopt conformations with internal H-bonds have better passive membrane permeability. Besides locking a specific conformation, macrocyclization of linear peptides can lead to structural changes that result in endopeptidase-resistant molecules[9]. This addresses one of the major limitations of linear peptides: their susceptibility to undergo proteolysis in the cell and in the blood.

These are but a few examples (among many reported in the literature)[1a, 1d] of the potential of macrocycles and the advantages of macrocyclization for drug development. Surprisingly, orally administered macrocyclic drugs such as cyclosporine A, tacrolimus and rapamycin are outside the window of what is generally considered to be drug-like properties[10] i.e. their molecular weights are often > 500-900 g/mol and their number of H-bond donors (>5) and acceptors (>10) and polar surface area (>140) are beyond the accepted drug-like spectrum[11] (Table 1). Either these bioactive macrocycles are exceptions to the current standard for drug-like molecules or understanding the unique properties of macrocycles that brought about these favorable overall pharmacokinetic properties could open up new rules for developing therapeutic molecules. This avenue has been recently

explored by Whitty and colleague who analyzed the binding modes of various macrocycle-protein complexes and proposed some useful guidelines for designing synthetic macrocycle libraries with structural and physicochemical features that will likely have high affinity to protein targets and good bioavailability[12].

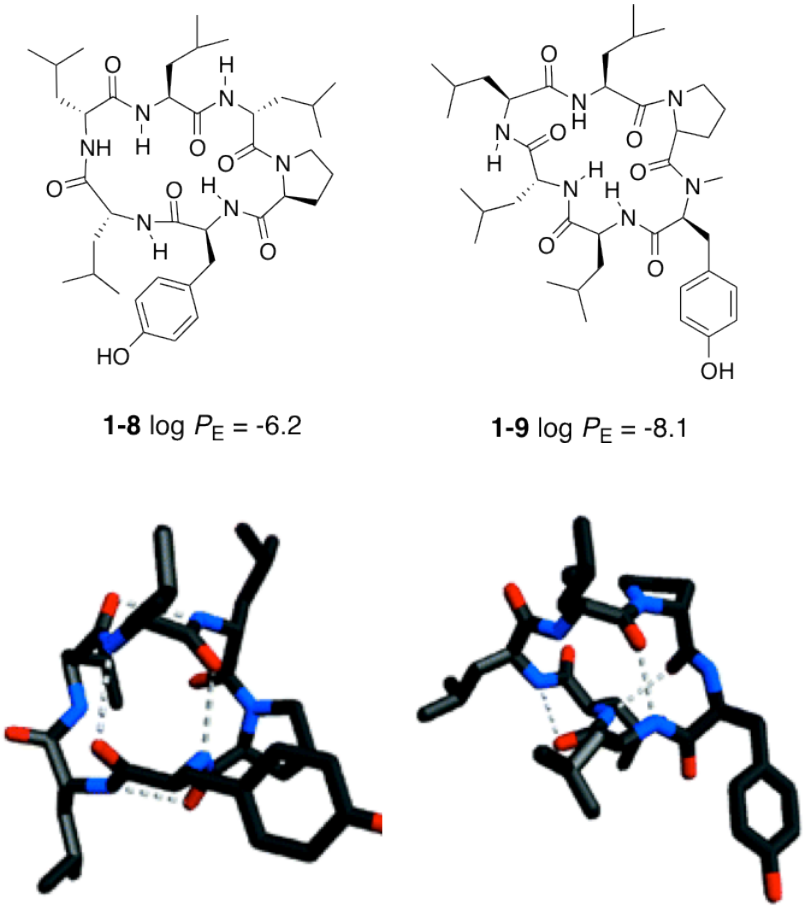

Fig. 1-4. Effect of macrocyclic conformations in membrane permeability. NMR structural analysis showed that the hydrogen-bonding network in diastereomer **1-8** (H-bonds are internally satisfied due to a pseudo-symmetric conformation) made it more permeable than distereomer **1-9** (some hydrogen-bondng groups are oriented to the solvent due to an irregular twisted conformation). The macrocycle conformations are reused with permission.

Table 1-1. Examples of orally-administered macrocyclic drugs that don't have drug-like properties.

Orally-administered macrocyclic drug	MW (da)	H-bond donor	H-bond acceptor	Polar surface area
Cyclosporin A	1203	5.2	12	279
Tacrolimus	804	3.3	3	178
Rapamycin	914	4.3	13	195

1.2.4 Macrocyles can modulate difficult therapeutic targets

In addition to the upsides of macrocyclization in optimization of biological and pharmacological properties of molecules, the huge interest in macrocycles is motivated by their ability to address targets often inaccessible to both standard small molecules and biologics - the most highly studied of which is the protein-protein interaction[13]. One of the various mechanisms by which macrocyles modulate protein-protein interactions is through either stabilization or destabilization of protein complexes. For example, epothilone B and its lactam analog Ixabepilone (an antibreastcancer metastasis drug) *stabilize* the α-β tubulin dimer[14] while halichondin B and its analogs *disrupt* the microtubule dynamics by destabilizing these tubulin dimers[15]. Another mechanism is through direct structural modification of protein topologies. For example, the cyclic peptide spiramycin and the macrolide antibiotics erythromycin and carbamycin narrow the ribosome's exit tunnel by binding to the inner surface of the ribosomal tunnel[16].

1.2.5 Summary

Clearly, the unique structural properties of a macrocycle allow it to occupy a chemical space distinct from other molecules or its acyclic counterpart. Conformational pre-organization provided by limited bond rotation of the ring can be harnessed to significantly improve not just the potency and selectivity of biologically active molecules but its pharmacological and overall pharmacokinetic properties as well. Macrocylization has provided an alternative strategy that medicinal chemists can use to optimize compound structure more suitable for development as pharmaceuticals. Most macrocyclic drugs do not fall into the standard categories of drug-like molecules. Understanding how these macrocycles work can introduce new parameters or rules for developing drugs as well as deepen our understanding of basic cellular processes such as the mechanisms of cell permeability. Macrocycles have successfully demonstrated their ability to modulate difficult targets inaccessible to either standard small molecules or biologics. Besides expanding the repertoire of chemical space available for development of probe molecules or drugs in the otherwise crowded-area of enzymatic inhibition, macrocycles also opened up new biological targets such as protein-protein interaction surfaces. This provided more options for therapeutic interventions and more areas to explore for mining information on basic biological and cellular processes. Moreover, the initial efforts in drug discovery programs such as screening for biologically active molecules can greatly benefit from the inclusion of macrocyles with various ring scaffoldings in the chemical library screened. At the heart of all the benefits of macrocyle in medicinal chemistry, basic biology and drug discovery is the ability to use the macrocyclic ring as a scaffold to strategically orient pharmacophoric moieties and H-bonding functionality in three-dimensional space.

If macrocycles as a class is to live up to all its potential, deeper understanding of all the factors that contribute to the conformational pre-organization of macrocyclic ring needs to be clearly established. The next sections will specifically discuss the (1) implications of macrocyclic conformation to its biological activities and chemical reactivities and (2) the factors that affect macrocylic conformations.

1.3. Biological and chemical consequence of macrocycle conformation

The overall structure of a macrocycle, specifically its ring conformation, is critical to its biological activity and chemical reactivites. The conformation of the ring controls the orientation of reactive functionalities and H-bonding groups in the macrocycle[8]. Thus, the upsides of macrocylization mentioned in the previous subsections, i.e. improved binding affinity, better selectivity and paharmakokinetic properties are intimately linked to ring conformation. In fact, macrocyclization of acyclic small molecules is only effective if the cyclization results to ground state cyclized conformation that approximates the optimal bound conformation[5]. In addition to the importance of ring conformation to the biological activities of macrocycles, the overall topology (ring conformation and planar chirality) of macrocyles is also critical to the stereoselectivity of reactions involving its functional groups. This is illustrated by examples of macrocyclic diasstereocontrol and transannular transformations – two useful tools for asymmetric synthesis of macrocycles and polycyclic compounds. Understanding the factors that affect the conformation of macrocycles, therefore, is highly important. The next paragraphs

will discuss, in more detail, the contribution of macrocyclic ring conformation to the biological activities and chemical reactivities of macrocycles.

1.3.1 Effect of macrocyclic conformations to biological activities

The majority of the improvement in potency, selectivity and overall pharmacological and pharmacokinetic profile brought about by macrocyclization can be attributed to macrocyclic ring conformation. Macrocyclization of acyclic, biologically active molecules is only effective if the correct spatial arrangement of key binding groups or reactive functionalities is maintained. A direct example of the effect of conformation in selectivity is illustrated by the macrocyclization of the pan-ATPase inhibitors staurosporine and rebeccamycin described previously. Upon, macrocyclization, the C2-symmetric *anti* conformation is selective towards the AGC protein kinase group such as PKC while the distorted *syn* conformation is selective towards glycogen synthase kinase 3β (GSK3β). Another compelling example of the contribution of macrocyclic ring conformation in both biological and physicochemical properties is illustrated by a comprehensive SAR study of a HSP-90 inhibitor by a group of scientists from Pfizer[17] (Fig. 1-5). Macrocyclization **1-11** of an anticancer clinical candidate **1-10** gave better biological activity. Furthermore, simple addition of a methyl group **1-12** resulted in better pharmacological activities. There are plenty more reports in the literature that demonstrates the huge contribution of the structural features of macrocyclic ring to the biological activities of macrocycles[1a]. What is not clear though is how specific structural features such as the stereogenic elements on the ring (i.e

stereogenic centers and stereogenic axis and planes) affect the conformation of bioactive macrocycles.

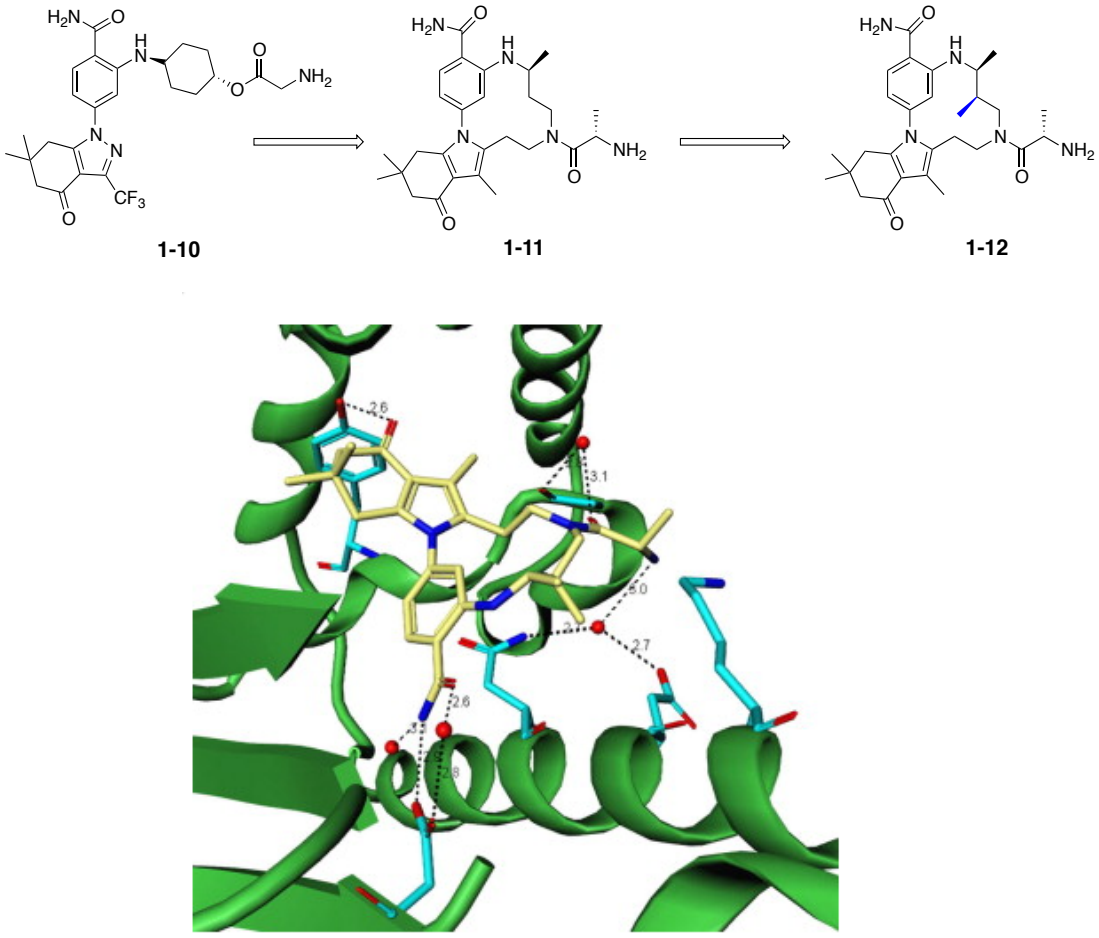

Fig. 1-5. The shape of the macrocycle is important to its biological activity. Rigidified version **1-11** of acyclic anticancer clinical candidate **1-10** improved its biological activity. Simple addition of a methyl group **1-12** with a specific chirality improved its physiological activity. The methyl group does not seem to interact with any key amino acids around the binding site (as shown by the co-crystal structure of **1-12** bound to HSP-90) suggesting that the improvement in pharmacological activity might be due to changes in ring conformation induced by the added methyl group. The co-crystal structure was reused with permission.

1.3.2 Effect of macrocycle conformation on its chemical reactivities

Macrocycles undergo unique chemical transformations such as macrocyclic diastereocontrol and various transannular reactions where the fate of the transformation is governed by the ground state conformation of the macrocycle.

1.3.2.1 Macrocyclic stereocontrol

In Still's pioneering work, alkene-containing macrocycles undergo highly stereoselective reactions termed macrocyclic stereocontrol[18]. This control is primarily due to the orientation of alkene plane (which is perpendicular to the molecular plane) and thus only one face is accessible to reagents leading to highly stereoselective reactions (Figure 1-6a). Furthermore, addition of one or two methyl groups at different positions around the ring can significantly affect the stereochemical outcome of the reactive functionalities on the ring. Macrocyclic stereocontrol has been used in a number of key transformations in the synthesis of natural products. Examples include the total synthesis of cladiellin, a marine natural product where the key transformation is the diastereoselective dihydroxylation of trisubstituted olefin without the use of assymetric reagent[19]. Another example is the synthesis of neopeltolide in which the key transformation is the stereoselective hydrogenation controlled by the ground state conformation of the macrocycle[20] (Fig. 1-6b).

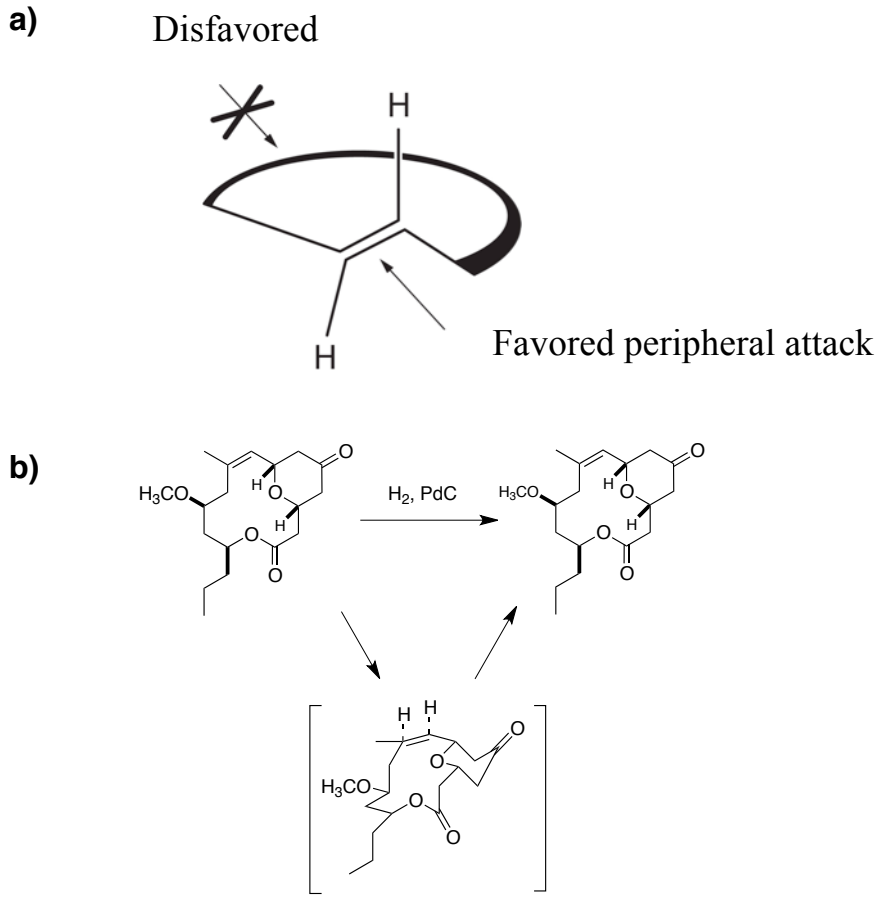

Fig. 1-6. The shape of the macrocycle is important to its chemical reactivity as illustrated by macrocyclic stereocontrol. (**a**) Macrocycyclic stereocontrol is brought about by the perpendicular orientation of the alkene plane relative to the molecular plane. (**b**) Synthesis of neopeltolide natural product showing the macrocyclic diasstereocontrol as the key transformation.

1.3.2.2 Transannular transformations

Relatively flexible macrocycles on the other hand, can undergo transannular interactions leading to intramolecular collapse to form polycyclic molecules (Fig. 1-7). One example is Baran and colleague's Palau'amine synthesis in which the macrocycle conformation of macropalau'amine allowed for the desired transannular reaction leading to the hallmark trans-5,5 ring system[21] (Fig. 1-7a).

Another example is the olefin isomerisation/intramolecular conjugate addition reported by Porco and colleague to get a tricyclic ring systems accessed via transannular cyclization of macrocyclic bis-lactams[22] (Fig. 1-7b). The last example in Fig. 1-7 shows the tandem oxy-Cope/ene reaction reported by Bariault and co-worker where the *E*-olefin geometry of the macrolactone intermediate gave an exclusive trans ring junction. Furthermore, the more stable ground-state chair-like conformation of the trans-annular ene reaction transition state resulted to the preferential formation of the observed tricyclic product[23] (Fig. 1-7c).

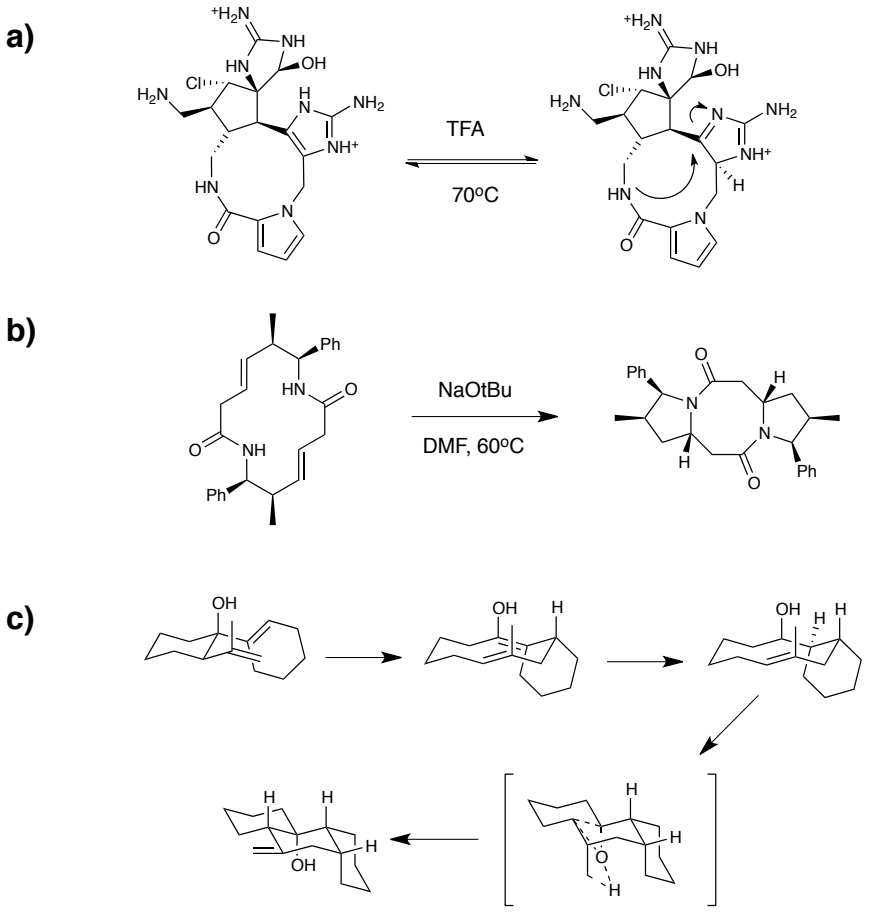

Fig. 1-7. The shape of the macrocycle is important to its chemical reactivity as illustrated by transannular interactions.

1.4 Factors that affect the conformation of macrocycles

The previous two sections illustrated the contribution of the unique structural features of macrocycles to its biological and chemical reactivities with emphasis on the ring conformation as a critical structural feature. The discussion was meant to explain the motivation behind the importance of understanding, at a fundamental level, all the factors that affect the stable conformation adopted by the macrocyclic ring, which is the main goal of our investigation. To put our work into proper perspective in the field of structural analysis of macroycles, this subsection will review the current understanding of the factors that control macrocyclic structure.

A given macrocycle can exist in various stable conformations but only a few are low enough in energy to be accessible at room temperature. In general, conformational biasing in macrocycles is governed by their tendency to minimize transannular nonbonded repulsions. For macrocycles with various substitutions and unsaturated groups such as alkenes, esters and amides, the rules with respect to stable conformations adopted by the skeleton are more complex. Factors such as ring size, chemical composition of the ring skeleton (type and arrangement of functional groups, unsaturation, and planar units) and configuration of stereogenic elements (stereogenic planes and stereogenic centers around the ring) exert considerable contributions to the macrocycle conformation.

1.4.1 Conformational analysis of 14-membered macrocyles

The 14-membered macrocycles are one of the most highly studied systems due to the prevalence of 14-membered bioactive natural products[24]. According to Dale's pioneering work, 14-membered macrocycles should exist predominantly in a 'rectangular' diamond-lattice [3434] conformation[25] (Fig. 1-8b,c). Dale's analysis showed that cyclotetradecane is the first cycloalkane after cyclohexane that can have a strain-free conformation in the form of a diamond-lattice [3434]. It is composed of two 'three-bond' sides and two 'four-bond' sides, hence the name [3434]. Indeed, cyclotetradecane exists only in this [3434] conformation in solid state as supported by XRD[26] and solid state ^{13}C NMR[27]. In liquid state however, it loses its conformational homogeneity and exists in several conformations with the [3434] conformation being the most predominant one as supported by low temp NMR analysis[28], and vibrational spectroscopy[29].

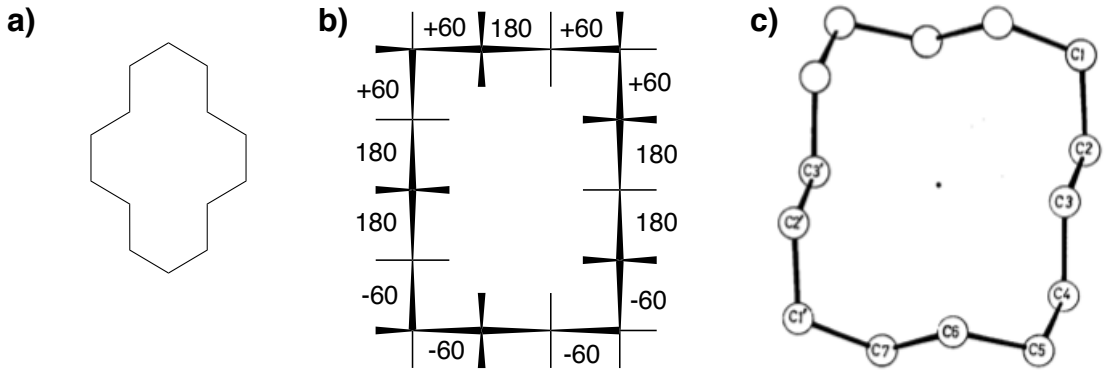

Fig. 1-8. Representations of cyclotetradecane. (**a**) Chemdraw 2D representation. (**b**) Dale's [3434] representation of triangular diamond-lattice conformation where torsion angles are represented as positive and negative numbers. (**c**) Schematic drawing of the actual crystal structure of cyclotetradecane from reference 25.

Dale also predicted that replacing the methylene groups in the cyclotetradecane ring with an oxygen atom or groups such as an amine, carbonyl or imine would cause only minimal perturbation on the diamond-lattice conformation. Indeed, 1-oxa-[30], 1,3,8,10-tetraoxa-[31], 1,8-diaza-[32], cyclotetradecanone[33], cyclotetradecane-1,8-dione[34], and tridecanolactone[34] gave the same [3434] diamond-lattice conformation. Moreover, insertion of either a ester[35] or amide[36] group into the ring gave the same [3434] conformation as the most stable conformation and with the lactam and lactone groups in s-trans conformation[25] in both solution[35] and solid state[36b].

More complex 14-memebered macrocycles with various substitutions and in combination with either a amide[28] or ester[35] group in the ring gave a more complicated correlation between substitution pattern, planar units (lactam or lactone) and macrocyclic conformation. Dale's analysis predicted that substitutions on 14-memberd macrocycles would not affect the preferred diamond-lattice [3434] conformation. Moreover, he predicted that the substituents could only occupy exterior (pseudo-equatorial) positions due to large transannular interaction associated with interior (pseudo-axial) position. Indeed, substituents around 14-membered macrocycles only occupy exterior positions. However, certain substituted 14-membered macrocycles did not adopt the [3434] conformation[28, 35]. Highly substituted 14-macrolides gave a different lowest energy conformation (i.e., [3335], [3344] etc.) distinct from the predicted [3434] conformation as supported by both XRD and molecular mechanics calculation[35] (Fig. 1-9). The conformation seemed to depend on the number and configuration of substitutions and the

substitution pattern. Similarly, using various techniques in both solid and liquid state, conformational analysis of 14-membered diketal dilactam[36a] painted a more complex relationship between planar units, stereogenic centers and conformation. In this ring system, the conformations depend on whether the macrocycle is chiral or achiral and on the stereochemistry of the substituents. Based on these reports, the rules governing the conformational preference of highly substituted 14-macrocycles are more complex than what Dale's analysis predicted. The substituents around the ring clearly affect the stable conformation adopted by the 14-membered macrocycle where various conformations distinct from the diamond-lattice [3434] conformation can be accessed depending on the number and configuration of stereogenic centers and the substitution pattern. How these stereogenic elements control the conformation of macrocycles, however, is not currently understood.

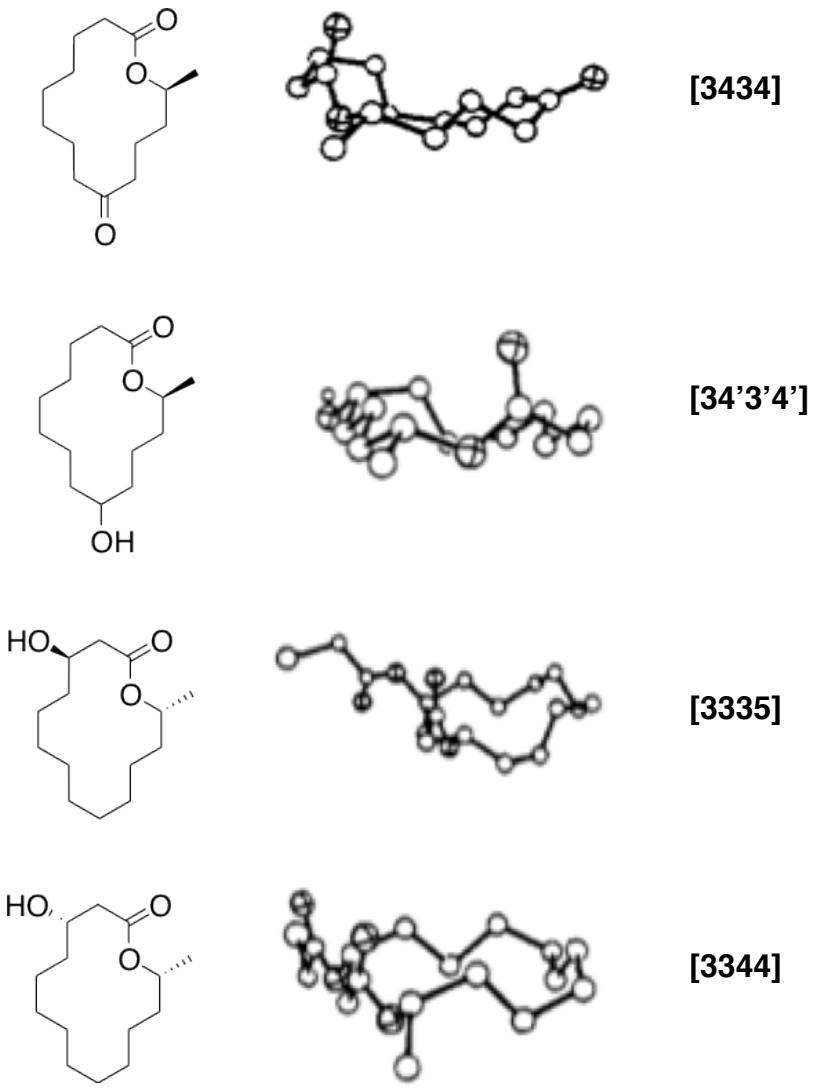

Fig. 1-9. Chemdraw and Ortep diagram of substituted 14-macrolides that adopted various conformations, with some that are distinct from the diamaond-lacttice [3434] conformation. The conformation seemed to depend on the number and configurations of stereogenic center around the ring and the substitution pattern.

1.4.2. Structural properties and conformational analysis of 13-membered macrocyles

Although they have not been investigated as thoroughly as 14-membered ring systems, 13-membered macrocyles have unique structural features. One report (among few) showed that in contrast to strained 12-membered cyclic tetrapeptides (CTPs), 13-membered CTPs can adopt a unique architecture that is more rigid, easier to cyclize, hydrolytically more stable and are conformationally homogenous in polar solvents[37] (Fig. 1-10). 12-membered CTPs have unfavorable strain due to the four trans-amide bond restraints. Addition of a methylene to a 12-membered ring CTPs by using a β-amino acid rotates one of the amide bonds that results to a more rigid structure. Because of the conformational homogeneity of 13-membered CTPs, 13-membered versions of the 12-membered natural product apacidin (HDAC inhibitor) were used to mine three-dimensional pharmacophoric features necessary for designing isoform-selective HDAC inhibitors[38]. These studies illustrate the potentials of the unique structural features of 13-membered macrocyles and reiterate the importance of understanding macrocyclic conformation in developing useful probe molecules.

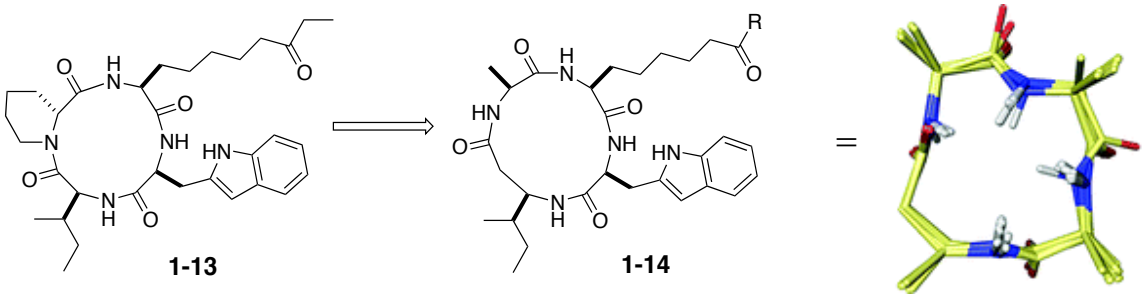

Fig. 1-10. 13-membered analogs **1-14** of the 12-membered natural product Apacidin **1-13** are conformationally homogenous in solution. The figure for the conformation of 13-membered macrocycle was reused with permission.

Compared to 14-membered macrocycles, the conformational preference of 13-membered macrocycles is less understood probably because of the lesser population of bioactive 13-membered macroyclic natural products[24]. A couple of studies on stevastelins – a 13-membered antiviral cyclic peptide that targets Vaccinia VH1 phosphatase – looked at the conformations in solution of a series of its diastereomeric analogs (Fig. 1-11). Using force field conformational searches for one force field constrained by variables from the NMR data, one report found that these diastereomers exist as a single conformational family in solution[39] (Fig. 1-11b). Using another method, NMR analysis of molecular flexibility in solution (NAMFIS), the same set of diastereomers were found to adopt different conformations in solution[40] (Fig. 1-11c). The accuracy of conformational analysis of macrocycles using NMR and computational methods is highly dependent on the type of conformational search methods used (different search methods have different parameters) and the condition and type of NMR analysis. Although the two studies found contradictory results between the homogeneity and

heterogeneity of the conformations of the studied series of diatereomers in solution, both agreed that using D-ser reduces conformational mobility in stevastelins and more importantly, subtle changes in stereochemistry at one or two chiral centers can greatly affect the conformational preference of this 13-membered macrocycles. Similar to 14-membered macrocycles, the specific contribution of configuration at a stereogenic center or combination of stereogenic centers and substitution pattern to the low energy conformation adopted by the macrocycle is not well understood.

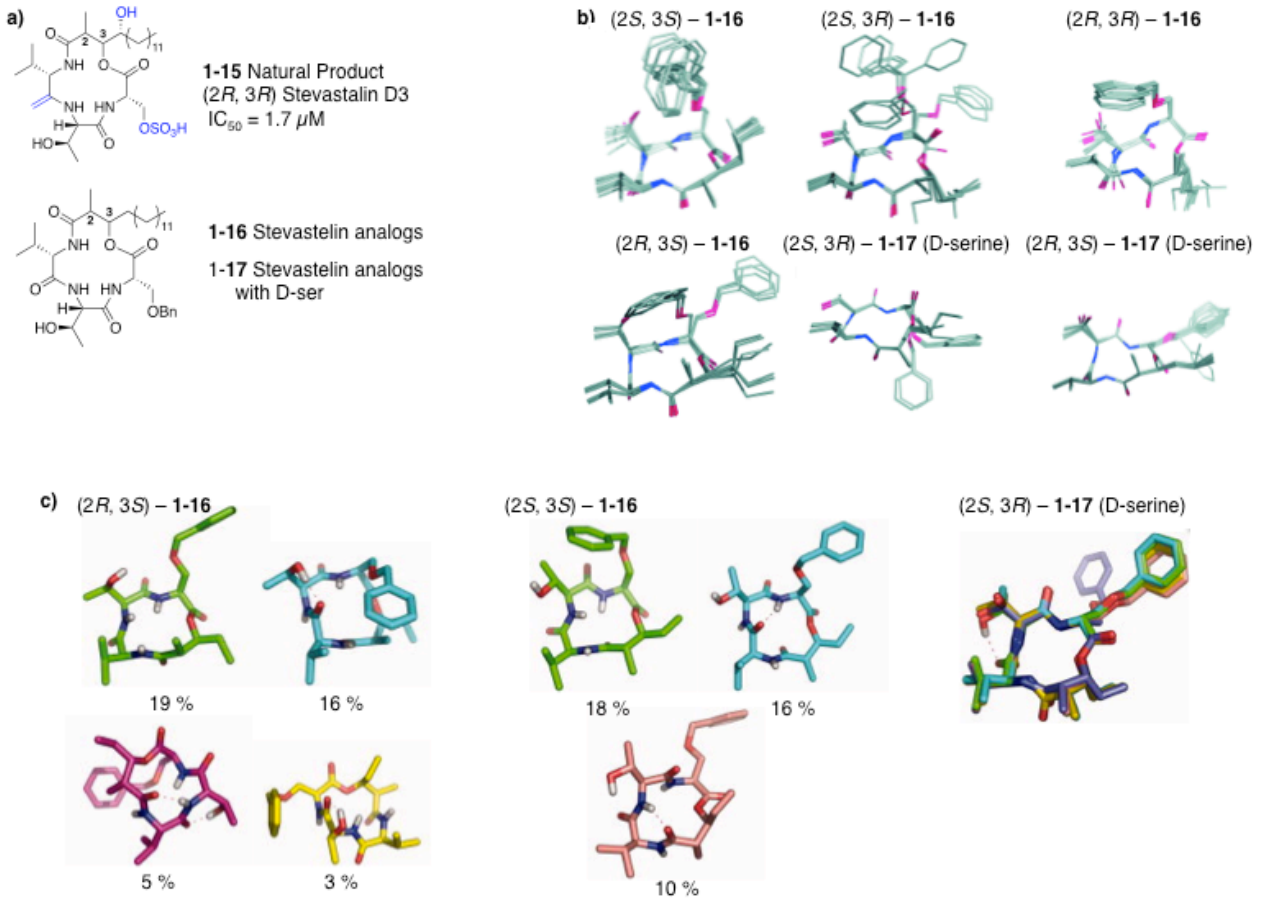

Fig. 1-11. 13-membered ring (Stevastelin analog) conformational analysis. (a) Chemdraw of the natural product stevastelin D3 and the core structure of its analogs. Blue font color emphasizes the structural difference between the two macrocycles. Conformational analysis of stevastalin diastereomers using two different combinations of NMR and computational methods led to two different conclusions regarding the homogeneity (**b**) – diastereomers **1-16** exists as a single conformational family in solution - and heterogeneity (**c**) – the same diastereomers of **1-16** exists in different conformations in solution - of the conformations of the diastereomers in solution. Both analyses agreed that using D-ser **1-17** led to a homogenous conformation in solution. Figures for the different conformations were reused with permission from ref 38 and 39.

1.5 [13]-macrodilactone: motivation, research question, hypothesis, research design and strategy

1.5.1 Motivation and research question

As emphasized in the introduction, macrocycles as a class of molecules have unique structural properties that allow them to occupy a chemical space distinct from other molecules or their acyclic counterparts. This unique chemical space has great potential in biology (developing novel chemical probes, and therapeutics) and chemistry (developing novel chemical transformations and asymmetric reactions). The unique structural properties are intimately linked to ring conformation. Thus, understanding the factors that control the conformation of the ring will be very useful. Dale's pioneering work on 14-membered macrocycles greatly simplified its conformational analysis but is not applicable to more complex, highly substituted 14-membered macrocyclic systems. 13-membered macrocycles, although possess interesting structural and biological properties are less studied. In both 13-membered and 14-membered macrocycles or probably, in macrocycles as a class in general, one of the important areas that need clarification is how the stereogenic elements (stereogenic planes and stereogenic centers around the ring) contribute to the stable low-energy conformation adopted by the macrocyle. Although, many have observed that subtle changes in the stereochemistry in one or two chiral centers have tremendous impact on conformation, as far as we know, no one has figured out how this happens. We think that this is because most of the reports used macrocyclic systems with multiple stereogenic centers already set in the ring. Such is the case for cyclic peptides, which is the macrocyclic system used by majority of

scientists who work in this field. We thought that in order to really understand the contribution of stereogenic centers on macrocyclic conformation, a systematic study is required. Starting from a ring system without stereogenic center followed by systematic incorporation of one streogenic center at a time at specific position around the ring can help pinpoint the exact contribution of specific stereogenic center and combinations thereof. One of the overarching goals in our lab is to understand, at a fundamental level, all the factors that affect the overall structure of macrocycles.

1.5.2 Hypothesis, research design and strategy

Currently, we use the [13]-macrodilactone as our model system to systematically explore the parameters that govern its structure. Consider the unsubstituted macrocycle **1-19** in Figure 1-12. Atoms of the ring are categorized as part of a planar unit such as the two esters (atoms C4-C7 and C12-C2) and the *E*-alkene (C8-C11) or elsewhere (atom C3). Connections between planar units can be through a bond, as in the connection of the C4-C7 ester with the alkene, or through an atom (and its associated bonds), as between the two ester units which are connected by C3. Starting with the C12-C2 ester unit, a motif of planar unit, atom, planar unit, planar unit develops (Fig. 1-12).

We look at the contribution of the interplay between planar units (2 esters and an e-alkene) and stereogenic centers around the ring on its overall structure in solid state using X-ray crystallography. We describe the three-dimensional structure of the [13]-macrodilactone using three terms - planar chirality, shape and topology. The planar chirality refers to the configuration of the embedded stereogenic *E*-alkene plane. We use

shape to describe the conformation or geometry adopted by the ring skeleton regardless of the substituents. We use topology as a more encompassing description of the overall structure of the [13]-macrodilactone because it takes into consideration all the structural features i.e., planar chirality, shape and the orientation of functional groups in the ring and in the substituents.

Our major hypothesis is that the numbered atoms (Fig. 1-12) – we call key atoms - that are positioned at the edge of each planar unit can greatly influence the overall topology of the macrocycle primarily due to steric considerations. If the configuration of a substituent at any of the key atoms results in ring strain, the planar units will rearrange themselves forcing the macrocycle to adopt a different shape. To test this hypothesis, we systematically incorporate one and two substituents at a time around the key atoms on the ring using a synthetic route we have previously reported – a series of acylation of various diol using various pentenoic acid followed by ring closing metathesis of the corresponding diene[41]. This systematic incorporation of stereogenic centers will allow us to determine the actual contribution of the configuration at one or a combination of stereogenic centers as well as the substitution pattern on the overall topology (planar chirality, shape and functional group orientations) of [13]-macrodilactone in solid state using X-ray crystallography. Using this strategy, we have previously reported a series of observations on mono-substituted[41b, 41d] and di-substituted 13-macrodilactones[41c, 41d] .

In this chapter, we construct a general model that explains the topology of our [13]-macrodilactones. The model collects the factors that govern the topology and offers a physical rationale behind them. Our analysis will focus especially on how the stereogenic centers at key atoms affect the topology of [13]-macrodilactones. We use a

combination of crystallographic data along with computational methods to categorize the topologies and to understand their origins. We think that our systematic approach to dissect the principles that govern the structural preference of [13]-macrodilactones will be helpful in synthesizing macrocycles with designed structural properties. Although our observations are primarily based on X-ray crystallographic data and some computational methods and are thus bound by the limitations inherent to these types of analyses, the fundamental information they revealed about the [13]-macrodilactone systems has value and might be applicable to other ring systems with similar chemical composition.

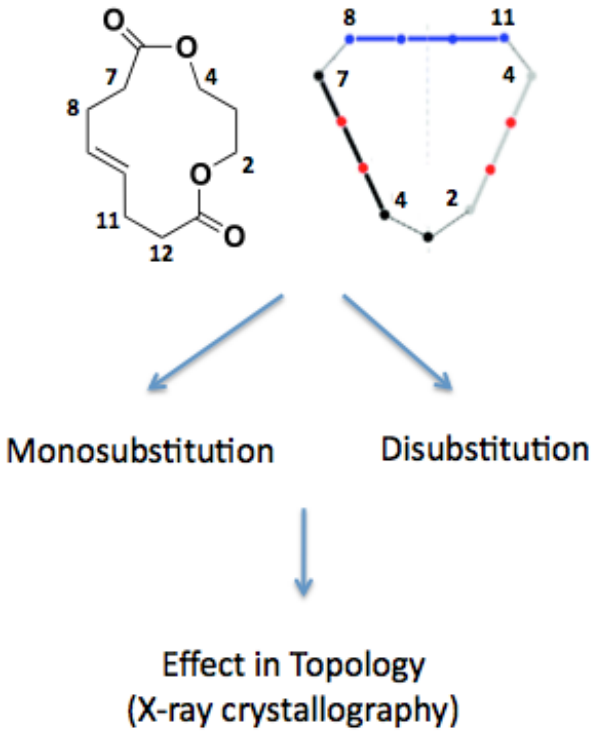

Fig. 1-12. Research design and strategy

1.6 Unsubstituted [13]-macrodilactone: synthesis and structural analyses

Our goal has been to systematically assess the contributions of specific stereogenic centers on the topology of [13]-macrodilactones. All our previous reports were focused on substituted [13]-macrodilactones[41b-d]. To gain an understanding of the inherent conformational preferences of the macrocycle, however, we synthesized and characterized the unsubstituted [13]-macrodilactone **1-19**. Its structure serves as a reference for comparison to all the subsequent substituted structures. In this way, we could assign the effect of the configuration of stereogenic centers at the key atoms on the overall structure of the [13]-macrodilactone.

1.6.1 Unsubstituted [13]-macrodilactone: synthesis and X-ray crystal structure

The unsubstituted [13]-macrodilactone **1-19** was synthesized using the route we previously reported[41b-d] and characterized using X-ray crystallography. The starting 1,3 propanediol was run though a series of acylation using pentenoic acid to get the diacylated diene **1-18**. This acyclic precursor was closed via a ring closing metathesis using Grubb's 2nd generation catalyst (Scheme 1-1).

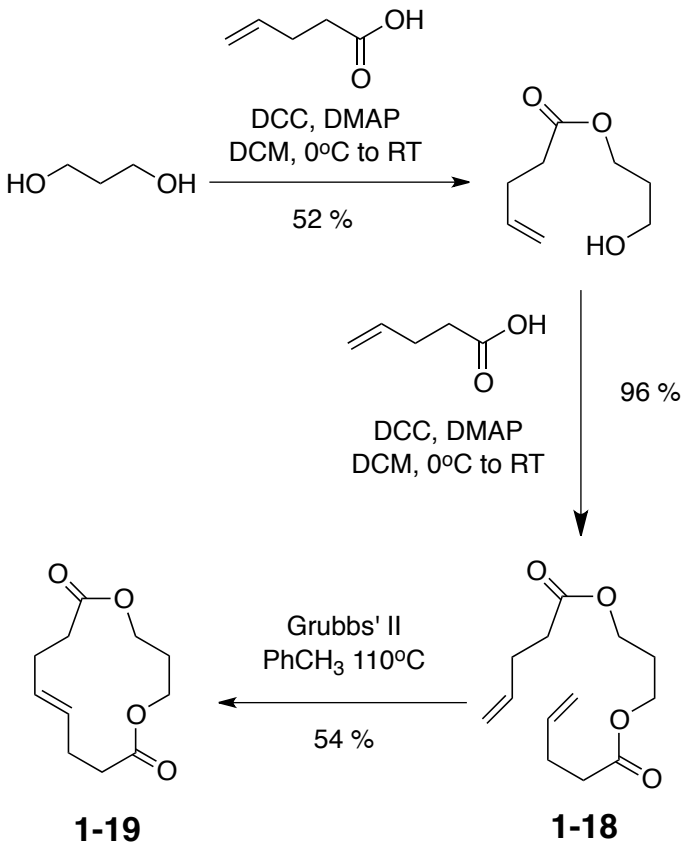

Scheme 1-1. Synthesis of [13]-macrodilactone

Unsubstituted [13]-macrodilactone **1-19** is crystalline and its structure was characterized using X-ray crystallography. Like the other [13]-macrodilactones we previously reported, **1-19** is rigidified by three four-atom planar units: two ester planes of atoms 4,5,6,7 and 2,3,12,13 and the alkene plane of atoms 8,9,10,11. These planar units limit the number of freely rotatable bonds in the macrocyle (Fig. 1-12 and 1-13). The planar units arranged themselves in a non-coplanar manner around C3, an sp^3-hybridized carbon that is not a part of any planar units. This

atom is called a hinge atom because it acts as a hinge in which the two ester planes can rearrange themselves. The macrocycle adopted a shape that, when viewed from the side, looks like a ribbon and, from the top, looks like a triangle (Fig. 1-13). We call this shape 'ribbon' because the planar units wrap around each other in a manner that resembles a ribbon. This result establishes that the globally preferred shape for the [13]-macrodilactone is the ribbon shape. Importantly, **1-19** crystallized as a racemic mixture of enantiomeric macrocycles that exhibit planar chirality (Figs. 1-13, 1-14). *E*-alkene containing cyclic molecules such as *E*-cycylooctene shows planar chirality that is solely due to the streogenic *E*-alkene plane. Planar chirality in macrocycles was also observed for bisbenzimidazole macrocycles with chiral cyclic *E*-alkene linkage that hardly flips into its enantiomeric structure at room temperature[42]. Furthermore, for bisbenzimidazole macrocycles, the *E*-alkene planar chirality was effectively transferred to the *S* axial chirality of the bisimidazole framework and the *P* helical chirality of the cyclic *E*-alkene[43]. Both p*S* and p*R* planar chiral macrocycles - the planar chirality was assigned based on the configuration of the chiral *E*-alkene plane (Fig. 1-14) - are present in the unit cell for **1-19**, proving that the [13]-macrodilactone motif creates an element of stereogenicity on its own.

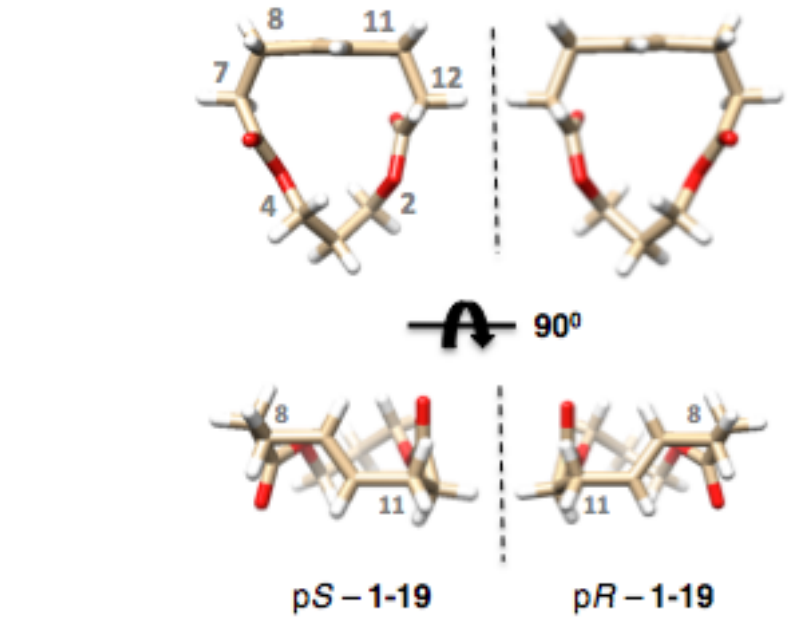

Fig. 1-13. Structural properties of unsubstituted [13]-macrodilactone. Crystal structure show the planar enantiomers - p*S* and p*R*. Numbered atoms show the three 4-atom planar units. Top figures show the triangular shape when viewed from the top of the molecular plane. Bottom figures show the ribbon shape when viewed on the side of the molecular plane.

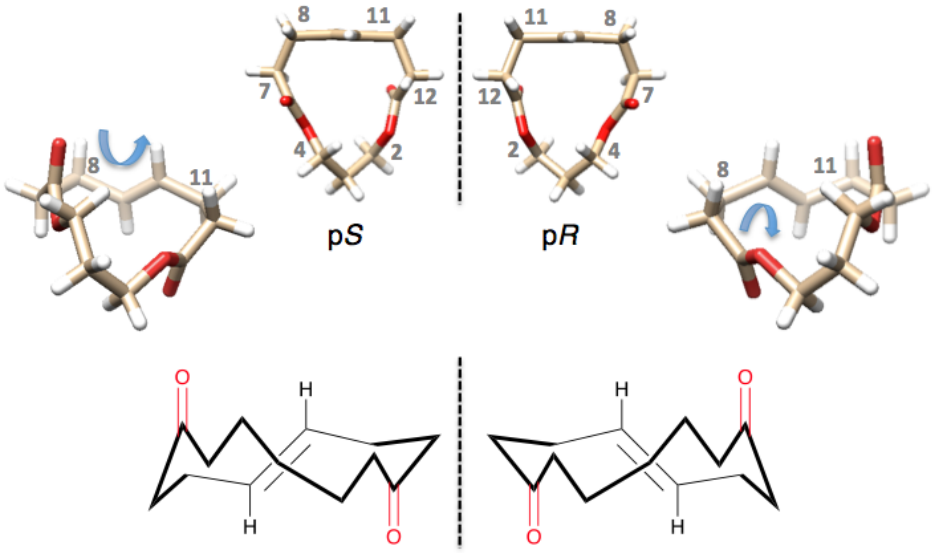

Figure 1-14. Assignment of planar chirality of [13]-macrodilactones based on the configuration of the stereogenic alkene plane.

1.6.2 Introduction to 2D maps of [13]-macrodilactones

In order to easily and systematically account for the similarities and differences in shape and planar chiralities between each [13]-macrodilactones, we have adapted a graphical representation previously developed for porphyrin systems[44]. The map shows the deviation of each atom from a molecular plane defined by three specific atoms: C3, C13 and C6. Deviations of each atom from the plane were measured using the software Mercury, available from CCDC. The y-axis corresponds to the relative distance of each atom with respect to the molecular plain and the positive or negative sign refers to the atoms above or below the specified plane (Fig. 1-15). Using the p*S* enantiomer of [13]-macrodilactone **1-19** as an example (Fig. 1-15), the plane consisting of the C3, C13, and C6 (coded in black) atoms were chosen to define the macrocyclic plane. To respresent a three-dimensional structure in two-dimensions, the macrocyle was treated as an acyclic structure by cutting through the C3 atom. This leads to a two-dimensional map where the C2-C3 bond represented as the first 2 points on the graph followed by the succession of atoms that constitute the ring skeleton with the C4-C3 bond represented as the last points in the graph. The same treatment was used to graphically represent the crystal structures of all the [13]-macrodilactones. These maps help to simplify the visualization of the similarities and differences in the shape and planar chirality between various [13]-macrodilactones that would otherwise require multiple figures to illustrate the different perspectives in looking at a three-dimensional structure.

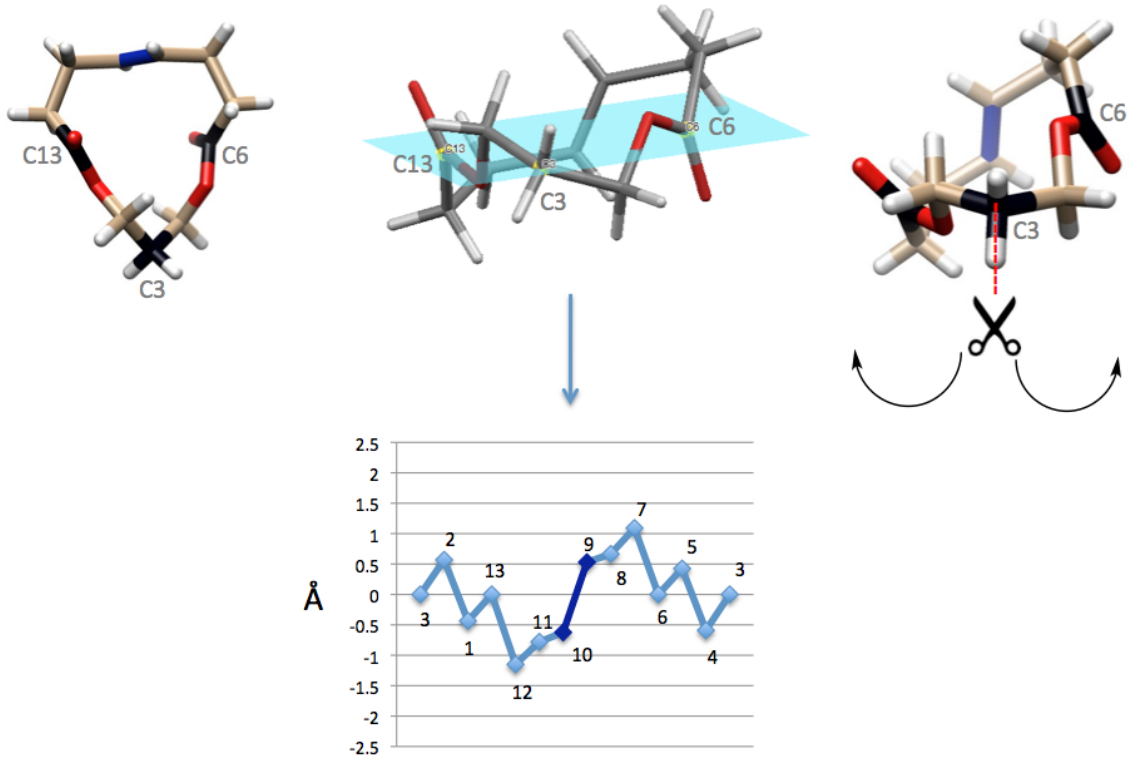

Figure 1-15. Construction of the 2D map of [13]-macrodilactone

1.7 Mono-substituted [13]-macrodilactones: syntheses and structural analyses

To look at the effect of one stereogenic center on the topology (planar chirality and shape) of the [13]-macrodilactone, we synthesized mono-substituted versions (with stereogenic centers at either C2 or C7) and followed on the subsequent structural changes using X-ray crystallography. Our lab previously synthesized the C2-substituted [13]-macrodilactone **1-20** and found that specific configuration at C2 gave a specific planar chirality where an *R* and *S* configuration gave a p*R* and pS planar chirality, respectively[41b] (Fig. 1-16). A new monosubstituted [13]-macrodilactone with a phenyl substitutent at C7 position was synthesized and characterized to look at the effect of incorporating a stereogenic center at the carbon alpha to the carbonyl[41d].

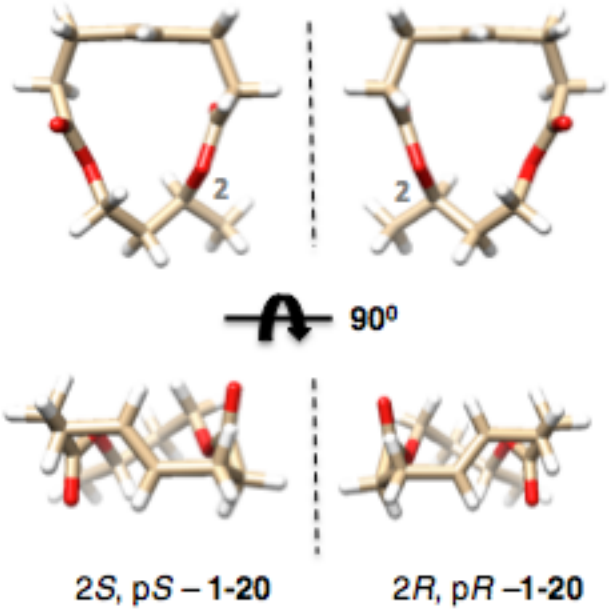

Fig. 1-16. X-ray crystal structure of the enantiomers of C2-methyl [13]-macrodilactone **1-20.**

1.7.1 C7 mono-substituted [13]-macrodilactone: Synthesis and X-ray crystal structure

C7-phenyl mono-substituted [13]-macrodilactone **1-22** was synthesized using the same synthetic route (Scheme 1-2) we established previously. 1,3- propanediol was first acylated with pentenoic acid using DCC and DMAP to yield the 3-hydroxypropyl 4-pentenoate in 56% yield. A second acylation with racemic 2-phenyl-4-pentenoic acid on the remaining free hydroxyl group gave diacylated product (80%). Racemic macrocycle **1-22** (*rac*-**1-22**) arose *via* RCM of the diacylated product using Grubbs' second-generation catalyst (58%).

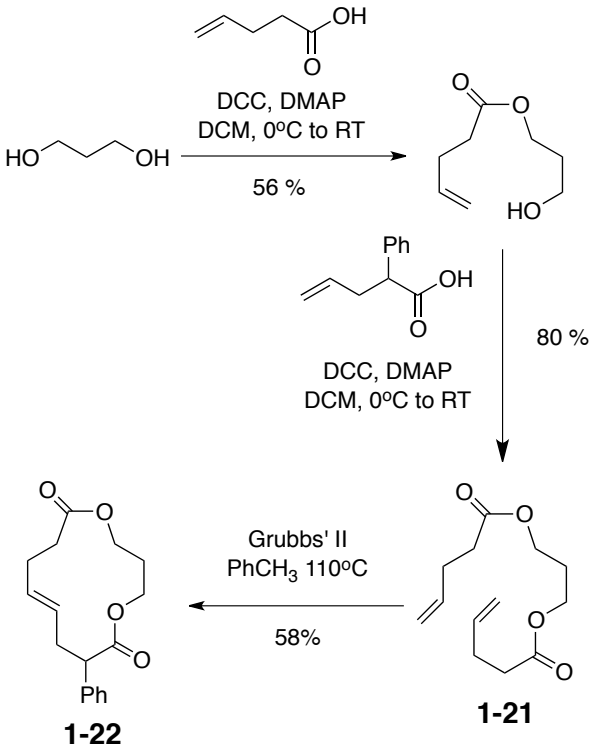

Scheme 1-2. Synthesis of C7-phenyl [13]-macrodilactone

Similar to the C2-methyl compound **1-20**, the configuration at the α-stereogenic center (C7) guides the topology of [13]-macrodilactones. Macrocycle *rac*-**1-22** was isolated as a crystalline solid, which was subjected to X-ray crystallographic analysis. Since racemic 2-phenyl-4-pentenoic acid was used in the synthesis, the corresponding macrocycle was also racemic. Present in its crystal lattice, therefore, were both enantiomers of the [13]-macrodilactone **1-22**. The C7 stereogenic center with *R* configuration resulted in a macrocycle with only p*S* planar chirality while the C7 *S* enantiomer gave rise to only p*R* planar chirality (Fig. 1-17). Transannular nonbonded interactions where sterically demanding substituents attached to the stereogenic center are situated away from the macrocyclic ring itself are minimized in this conformation. The enantiomers have the same shape but different planar chirality and, thus, different

topologies. Here, 'topology' includes the mirror-image orientations of the phenyl substituents and the carbonyl groups in three-dimensional space. It is important to note that the shape adopted by the backbone of **1-22** was similar to that of C2-substituted macrocycle **1-20** (RMSD = 0.0454, using 2*R*,p*R*-**1-20** and 7*S*,p*R*-**1-22**) (Fig. 1-18), supporting that this shape is generally the most stable conformation for the mono-substituted [13]-macrodilactones regardless of the location of the substituent (either C2 or C7) or the type of substituent (methyl or phenyl). Both C2 and C7 are at the junction of two planar units (Figure 1-12 and 1-13) corroborating the hypothesis that these positions are key stereogenic centers that direct the planar chirality, and hence the topology of [13]-macrodilactones.

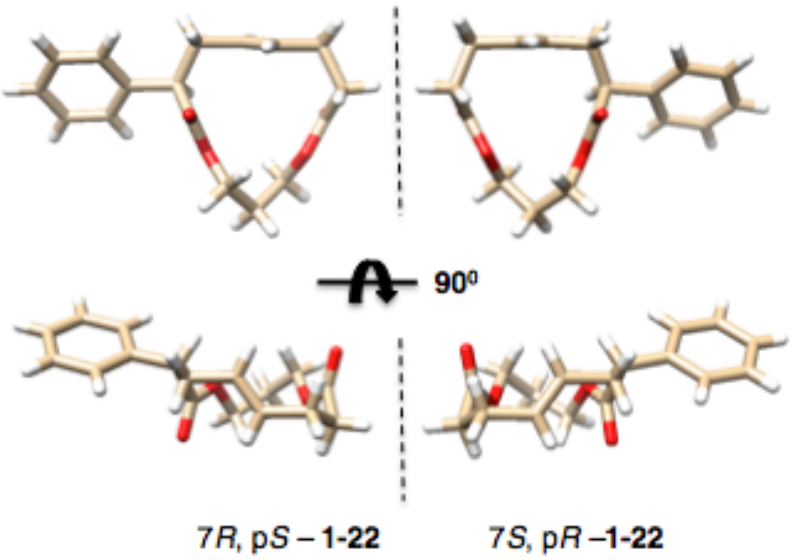

Fig. 1-17. X-ray crystal structures of the enantiomers of C7-phenyl [13]-macrodilactone **1-22.**

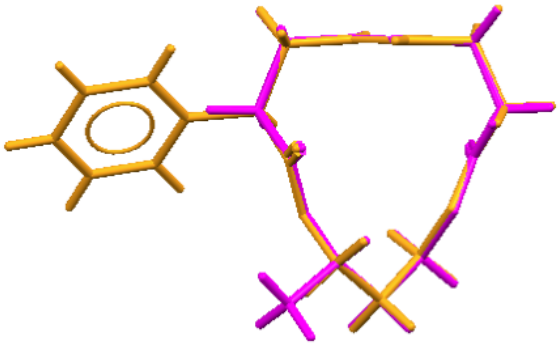

Fig. 1-18. Overlay of 2*R*,p*R* - **1-20** (pink) and 7*S*, p*R* - **1-22** (cyan) with an RMSD of 0.0454 showing common 'triangular' or 'ribbon' [13]-macrodilactone shape.

1.7.2 Illustration of α-carbon stereogenic center's control of planar chirality and demonstration of macrocyclic stereocontrol using chiral HPLC

To illustrate that it is indeed the configuration at the α-stereogenic center that dictates the planar chirality adopted by the [13]-macrodilactone, an enantioenriched version of **1-22** (7*S*,p*R*) was synthesized using 2*S*-phenyl-4-pentenoic acid (90% ee). Chiral HPLC profiles of *rac*-**1-22** and 7*S*,p*R*-**1-22** are shown in Fig. 1-19. The macrocycle derived from racemic pentenoic acid resulted in a 50:50 mixture of [13]-macrodilactones. The one synthesized from 2*S*-phenyl-4-pentenoic acid was enantioenriched, with an ee of 60%. We attributed the deterioration of enrichment between the acid and macrocycle to racemization of the chiral diester under the acylation conditions during diene formation. Nonetheless, the transfer of point chirality from the starting acid to the planar chirality observed in macrocycle 7*S*,p*R*-**1-22** corroborated our original conclusion about the control of planar chirality in [13]-macrodilactones by the α-stereogenic center. DMDO epoxidation of *rac*-**1-22** (Scheme 1-3) gave only one diastereomer of **1-23** as a pair of enantiomers (Figure 1-19). For 7*R*,p*S*-**1-22**, the enantioenrichment of the alkene was maintained after epoxidation to **1-22**. Reactions of these [13]-macrodilactones therefore exhibit a high level of macrocyclic diastereocontrol.

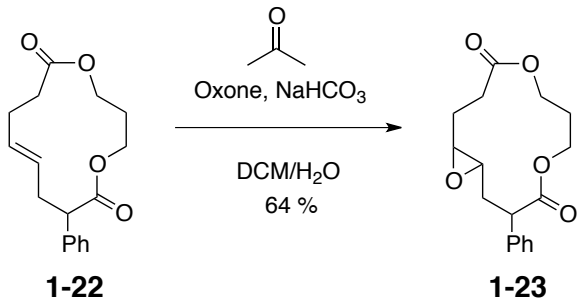

1-22 **1-23**

Scheme 1-3. DMDO epoxidation of rac-**1-22.**

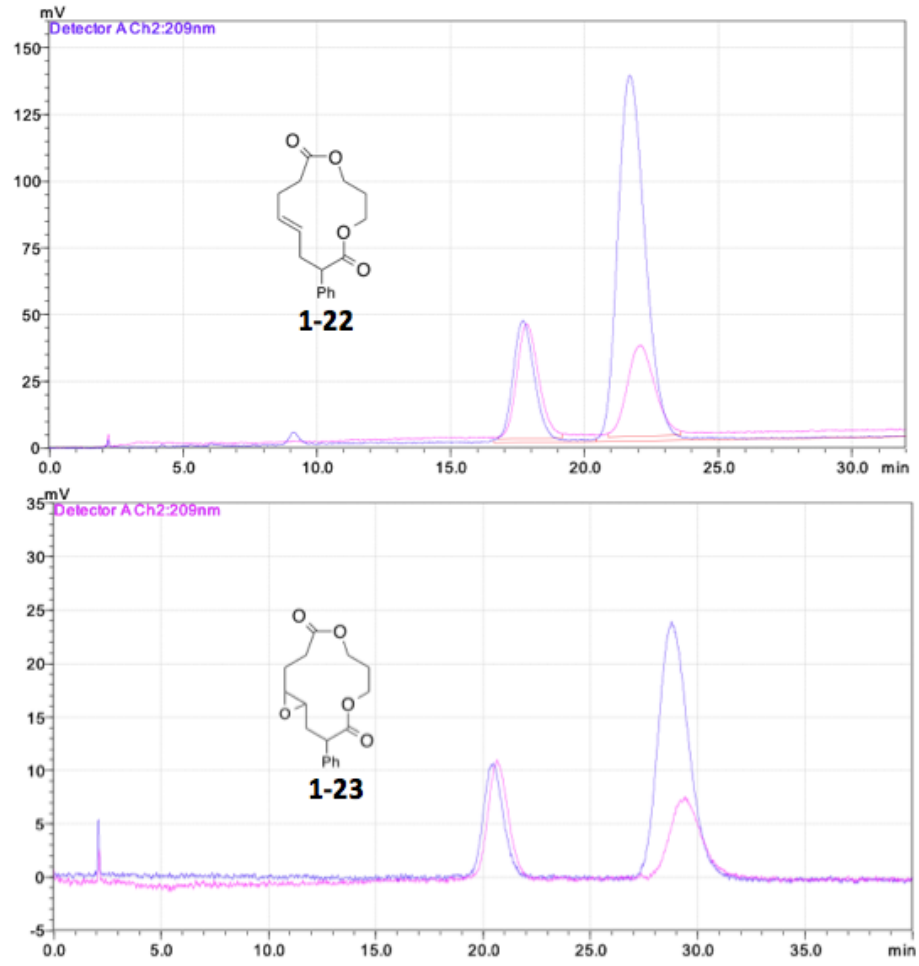

Fig. 1-19. Chiral HPLC profiles of racemic (pink) and chiral (blue) [13]-macrodilactone **1-22** and the corresponding epoxides **1-23**.

1.7.3 Structural insights on the effect of one stereogenic center on [13]-macrodilactone topology

Table 1-2. Point chirality-to-planar chirality correspondence in mono-substituted [13]-macrodilactones

Mono-substituted 13-macrodilactones	Point chirality	Planar chirality
C2-methyl	2S	pS
	2R	pR
C7-phenyl (if phenyl is given the 3rd priority in assigning configuration)	7R (7S)	pS
	7S (7R)	pR

The structures of the two mono-substituted [13]-macrodilactones (with a stereogenic center at either C2 or C7) demonstrated that the configuration at the center guides the planar chirality of [13]-macrodilactone where one configuration, either *R* or *S* only gave one planar chiral enantiomer, p*S* or p*R*. In the case of the C2-methyl [13]-macrodilactone **1-20**, the 2*R* center gave rise to the p*R* planar chirality. For **1-22**, the 7*S* configuration gave rise to the p*R* planar chirality. This observation is further supported by the fidelity of formation of only one planar chirality during cyclization of a homochiral diene**.** At first glance, it may seem that there is no correspondence between the configuration at the stereogenic center and the planar chirality of the macrocycle. However, if the substituent (methyl, phenyl, etc.) on the stereogenic center is given the third priority by convention, then the 7*S* configuruation of **1-22** becomes 7*R* (Table 1-2). It suggests that specific geometry of groups around the center (not necessarily equivalent to CIP *R* and *S* designations) does in fact set the planar chirality of the ring regardless of the substituent type (either methyl or phenyl) or location (either C2 or C7). If any

substituent on the ring will be given the third priority when assigning configuration at point chirality, then the rule for point-to-planar chirality in mono-substituted [13]-macrodilactone systems will be *R*-to-p*R* and *S*-to-p*S* (Table 1-2). Moreover, the unsubstituted [13]-macrodilactone **1-19** and the two monosubstituted **1-20** and **1-22** all adopted the same ribbon or triangular shape as illustrated by the 2D maps (Fig. 1-20). Also note that the substituents in **1-20** and **1-22** are all positioned outside of the ring or are in 'pseudo-equatorial' positions as evident in their crystal structure and in the 2D maps.

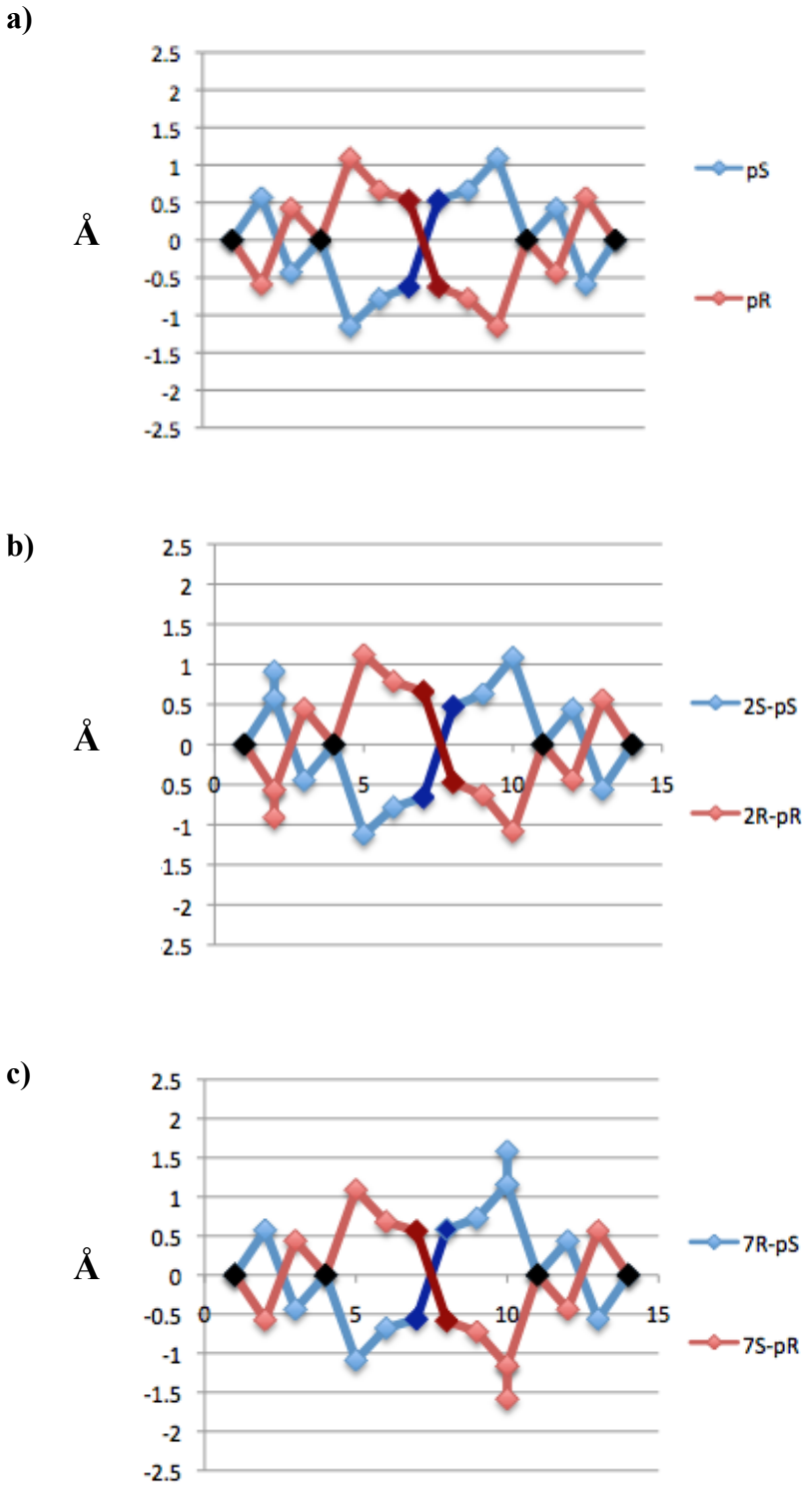

Fig. 1-20. 2D maps for the unsubstituted [13]-macrodilactone (a) **1-19** and mono-substituted [13]-macrodilactones (b) **1-20** and (b) **1-22**.

1.7.4 Origin of the control of [13]-macrodilactone planar chirality by one stereogenic center

Since the unsubstituted [13]-macrodilactone **1-22** contains an inherent planar chirality (an element of stereoisomerism), addition of another stereogenic element such as a stereogenic center could give rise to up to four stereoisomers. Combining specific isomers with either p*S* or p*R* planar chirality for each *R*, *S* configuration at the stereogeic center would give p*S*,*S*, p*S*,*R*, p*R*,*S*, and p*R*,*R* isomers. In cases where the [13]-macrodilactone had only one stereogenci center, we only isolate two stereoisomers - a pair of enantiomers – in which each configuration (either *S* or *R*) at stereogenic center gave rise to only one out of the two possible planar chiralities (p*S* or p*R*). This observation hypothesized that the energy associated with the conformation of the two stereoisomers we didn't isolate are higher energy conformations.

Ground-state energy minimization - using a dispersion corrected density functional (MO6-2x) paired with a robust basis set (6-31+G(d,p)) - was employed to look at the energetics associated with the conformations of **1-20** and **1-22 (**Fig. 1-21 and 1-22 **).** The C7-phenyl group in **1-22** was replaced with a methyl group to have the same number of atoms when comparing the energies for each macrocyels. The planar stereoisomers of **1-20** (2*S*, p*S* and 2*R*, p*R*) have degenerate energies and thus were isolated and crystallized as a racemate of planar enantiomers (Figs. 1-16 and 1-21). The other two stereoisomers (2*S*, p*R* and 2*R*, p*S*) that were not isolated (and probably were not formed) have degenerate energies as well but are 3.5 kcal/mol higher than their respective diastereomers **(**Fig. 1-21**)**. The specific combinations of 2*S*, p*R* and 2*R*, p*S* results in a

macrocyclic conformation in which the substituents are both in pseudo-axial position as opposed to pseudo-equatorial positions of the substitutents of stereoisomers 2*S*, p*S* and 2*R*, p*R*. A pseudo-axial position promoted transannular nonbonding interactions that resulted to a higher energy conformation. Similar observations were seen for the energetics of **1-22** but with a slightly lower energy difference (2.4 kcal/mol) between the isolated isomers (7*R*, p*R* and 7*S*, p*S* – with a methyl substituent instead of phenyl) and the other two potential isomers (7*S*,p*R* and 7*R*, p*S* - with a methyl substituent instead of phenyl) (Figure 1-22). It appears that for mono-substituted [13]-macrodilactones, regardless of substituent position (either C2 or C7) or type of substituent (either methyl or phenyl), the preference for a pseudo-equatorial position governs the selectivity for a specific planar chirality conferred by the configuration at the stereogenic center. Moreover, the shape adopted by the mono-substituted [13]-macrodilactones **1-20** and **1-22** is the same triangular or ribbon shape observed for the unsubstituted [13]-macrodilactone **1-20** showing that addition of one substituent in the ring does not affect the shape of [13]-macrodilactones.

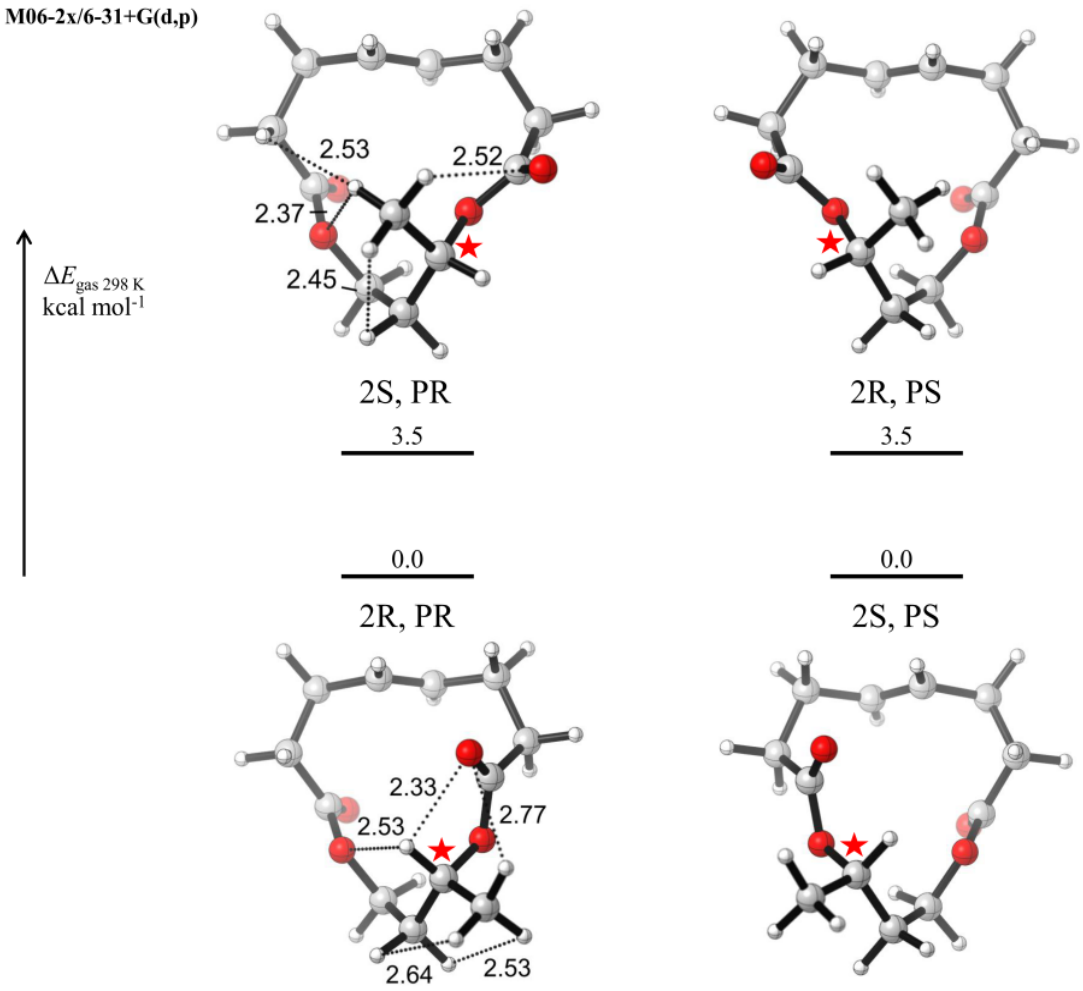

Fig. 1-21. Ground-state energy minimizations of conformations of four stereoisomers of **1-20.**

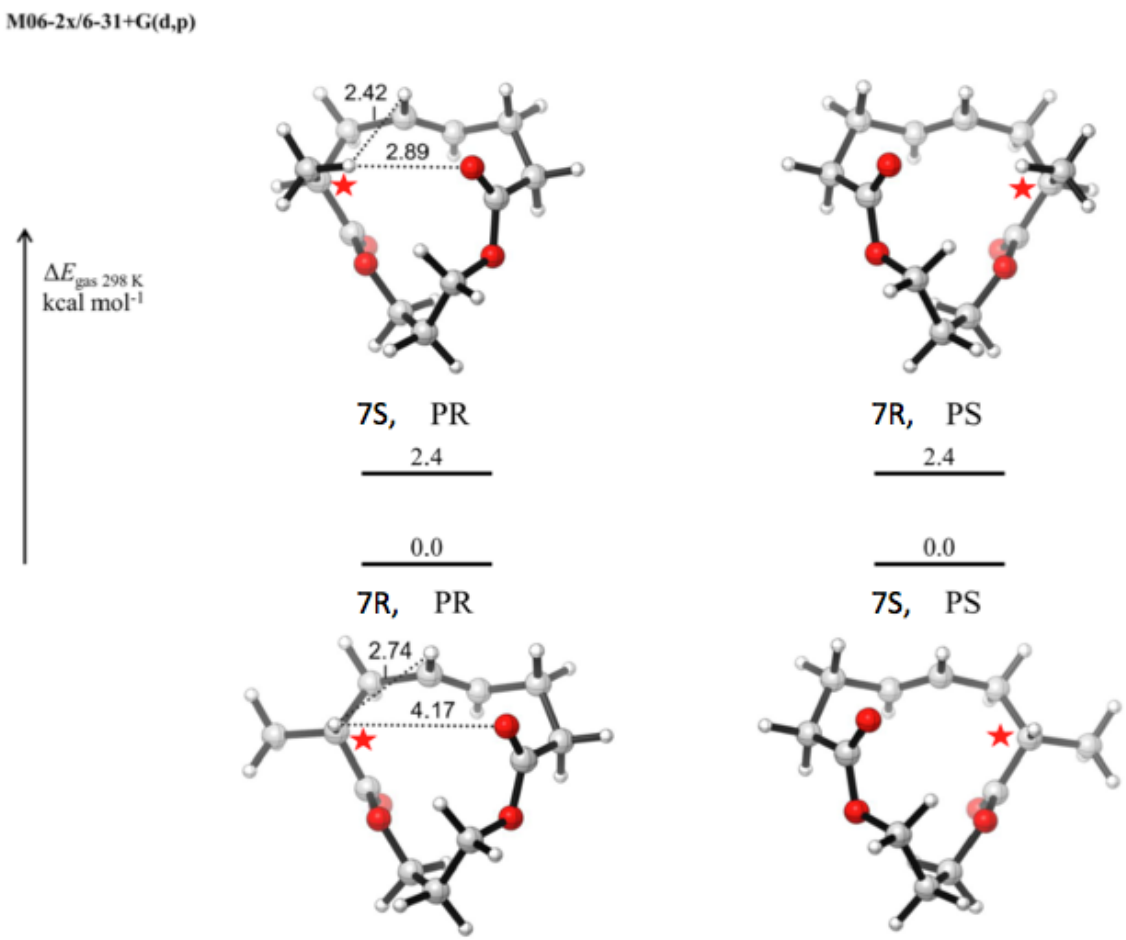

Fig. 1-22. Ground-state energy minimizations of conformations of four stereoisomers of **1-22** with a methyl substiuent instead of phenyl.

1.8 Di-substituted [13]-macrodilactones: syntheses and structural analyses

Subtle changes in stereochemistry of substituents can greatly influence the conformational preference and biological activities of macrocyles as discussed in the introduction. This observation has confounded medicinal chemists for a long time. Our systematic approach in using the [13]-macrodilactone systems lends itself to the possibility of addressing how the stereogenic centers around the macrocyle contributes to its overall structure. To explore some underlying principles on the effect of combinations of two stereogenic centers and substitution pattern on the planar chirality, shape and overall topology of [13]-macrodilactones, we used the same synthetic route we have previously reported to synthesize di-substituted macrocycles with various substitution patterns.

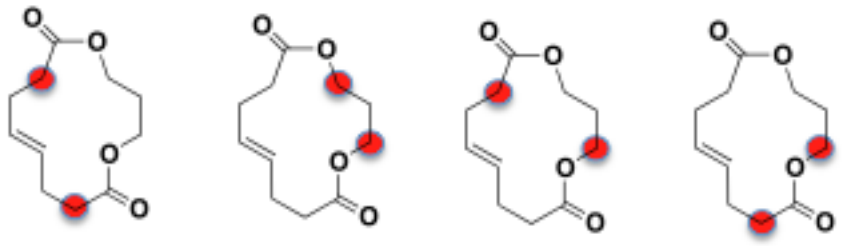

Fig. 1-23. Di-substituted [13]-macrodilactones with various substitution patterns. From left to right: 7,12; 2,4; 2,7; 2,12 di-substituted 13-macrodilactones.

1.8.1 C7, C12 - diphenyl [13]-macrodilactones: synthesis and X-ray crystal structure

C7 and C12 di-substituted [13]-macrodilactoens were synthesized to explore how the α-stereogenic centers work together to guide both the shape and topology of [13]-macrodilactones. They were prepared in the same reaction pot because the diastereomeric RCM precursors, an enantiomeric pair and a *meso* compound, could not be separated by chromatography. The synthesis starts with diacylation of 1,3 propane-diol with two

equivalence of 2-phenyl pentenoic acid and DCC and DMAP followed by ring closing metathesis again by using Grubb's 2nd generation catalyst. The two diastereomeric macrocycles **1-25** and **1-26** were separated by column chromatography (Scheme 1-4).

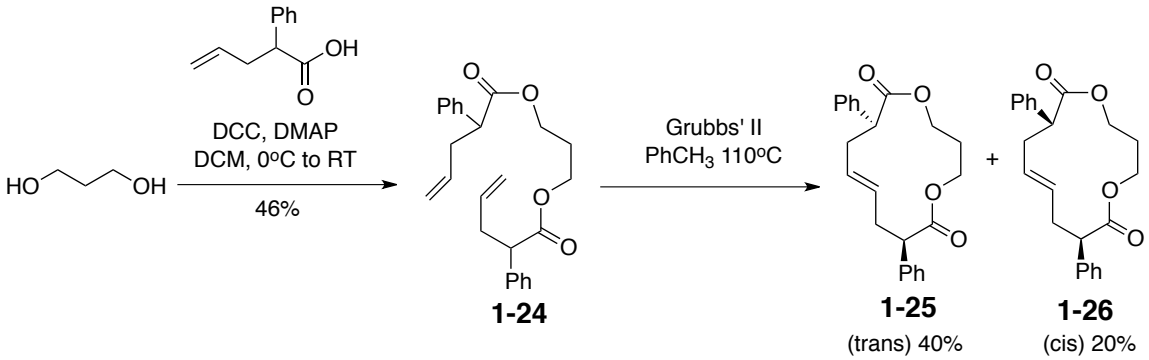

Scheme 1-4. Synthesis of C7, C12 diphenyl [13]-macrodilactones **1-24** and **1-26**.

Both *trans* diastereomer **1-25** and *cis* diastereomer **1-26** were crystalline solids that yielded to structural analysis from X-ray diffraction data. The structures of **1-25** and **1-26** revealed the interplay between the key stereocenters and their shapes. Specifically, the relative (*trans* vs. *cis*) configuration of the phenyl groups at the α-stereogenic centers dictated the shape adopted by each diastereomer and the configuration dictated the planar chirality (Fig. 1-24). All four compounds differ in their topologies by virtue of either the differences in their planar chirality or their shape.

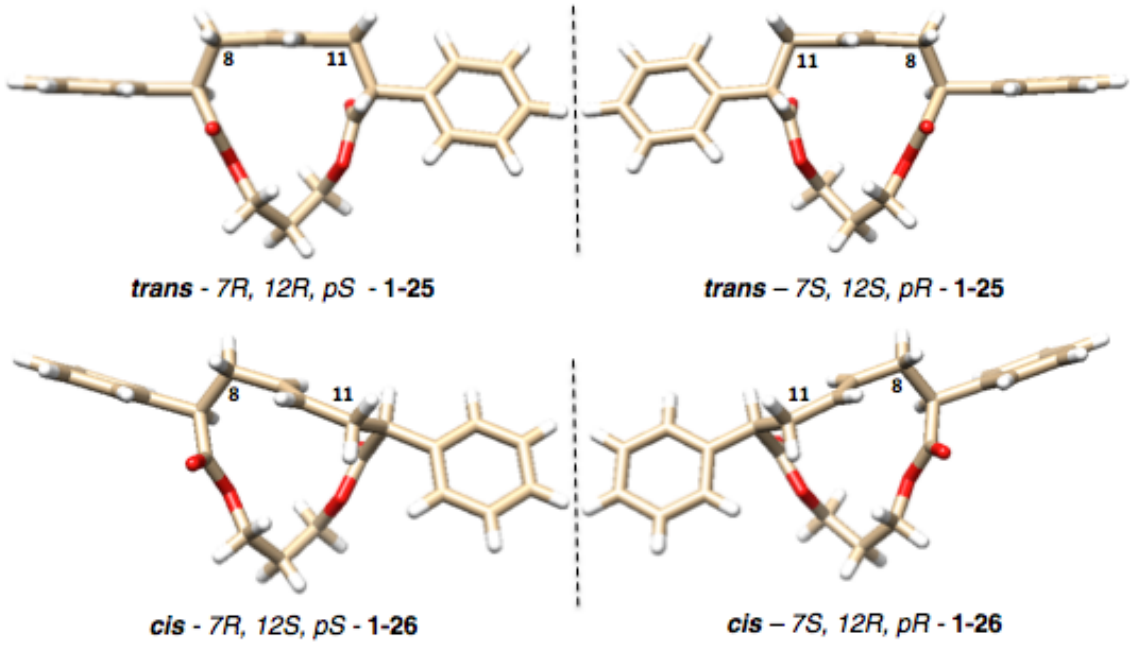

Fig. 1-24. Crystal structure of diastereomeric *trans* and *cis* [13]-macrodilactones, **1-25** and **1-26** (**1-25** /*trans* = 7*R*,12*R*,p*S* and 7*S*,12*S*,p*R*; **1-26** /*cis* = 7*S*,12*R*,p*R* and 7*R*,12*S*,p*S*).

The *trans* isomer was a racemic mixture of 7*R*,12*R*,p*S*-**1-25** and 7*S*,12*S*,p*R*-**1-25** with its shape reminiscent of unsubstituted [13]-macrodilactones **1-19** and mono-substituted [13]-macrodilactones **1-20** and **1-22**. In fact, the RMSD between the **1-20** and 7*S*,12*S*,p*R*-**1-25** was only 0.0487. (Fig. 1-25a). This shape was adopted presumably because the two phenyl substituents were oriented outside of the ring and thus minimized transannular nonbonded interactions. The *cis* configured isomers of **1-26**, on the other hand, adopted a different shape (RMSD 0.49 between **1-20** and 7*S*,12*S*,p*R*-**26**) (Fig. 1-25b). Inspection of the top, or "triangle" views of **1-25** and **1-26** in **Fig. 1-24** and **1-25** illustrates the difference. The non-ribbon shape of **1-26** is more compressed, or kinked, relative to **1-25** and its molecular plane is also more twisted. While the diene precursor of **1-26** was *meso*, **1-26** itself is a mixture of enantiomers defined by the planar chirality

(p*S* or p*R*) introduced to the molecules by cyclization. The relative stereochemistry at C7 and C12 probably prevents formation of the ribbon shape because minimization of transannular interactions in this case requires reconfiguration of the backbone and hence a different shape.

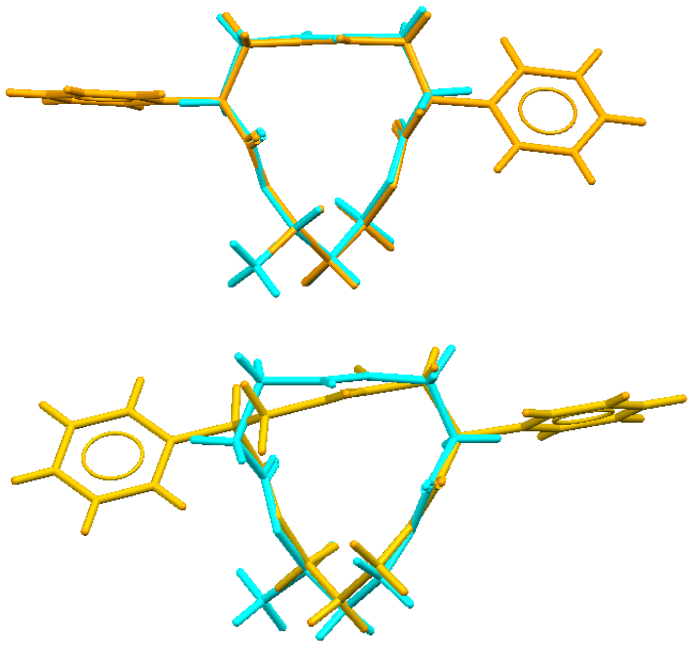

Fig. 1-25. Overlays of **1-20** in cyan and (a) *trans* di-substituted **1-25** (b) *cis* di-substituted **1-26** in yellow.

We previously observed that other key stereogenic centers (C2 and C4) can work constructively to reinforce the ribbon or against each other resulting in alternative shapes. For the C2, C4 compounds, the *trans* series adopted the ribbon conformation akin to **1-19**, **1-20**, **1-22** and **1-25** whereas the *cis* series gave rise to a different macrocyclic shape that was coincidentally distinct from the shape of **1-26**. The ribbon conformation seems to be of the lowest energy for these [13]-macrodilactones but, based on relative stereochemistry, alternative shapes and consequently topologies are available. Together the structural observations from this study suggest that shape and the topology of this

family of [13]-macrodilactones can be fine-tuned based on specific combinations of configuration on α-carbon stereogenic centers.

1.8.2 Synthesis of di-substituted [13]-macrodilactones with C2, C7 and C2, C12 substitution patterns

To explore some underlying general principles on the effect of combinations of two stereogenic centers and substitution pattern on the planar chirality, shape and overall topology of [13]-macrodilactones, we used the same synthetic route we have previously reported to synthesize new di-substituted macrocycles with new substitution patterns (Scheme 1-5). Compounds **1-27** and **1-28** have substituents at C2 and C12 while compounds **1-29** and **1-30** have substituents at C2 and C7. **1-27** and **1-28** were synthesized starting from 3-hydroxybutanol followed by acylation with 2-phenyl pentenoic acid and DCC and DMAP. The resulting mono-acylated hydroxybutanol was again acylated with, this time, pentenoic acid and DCC and DMAP. The last step is to close the ring, again, using Grubbs' second-generation caltalyst. The two diastereomers 1**-27** and **1-28** (each a pair of enantiomers) were isolated using column chromatography. The same route was used to synthesize the diastereomers **1-29** and **1-30** but instead of using 2-phenyl pentenoic acid first followed by pentenoic acid, the sequential acylation with DCC and DMAP was reversed where pentenoic acid was used first to acylate the 3-hydoxybutanol followed by another acylation with 2-phenyl pentenoic acid (Scheme 1-5).

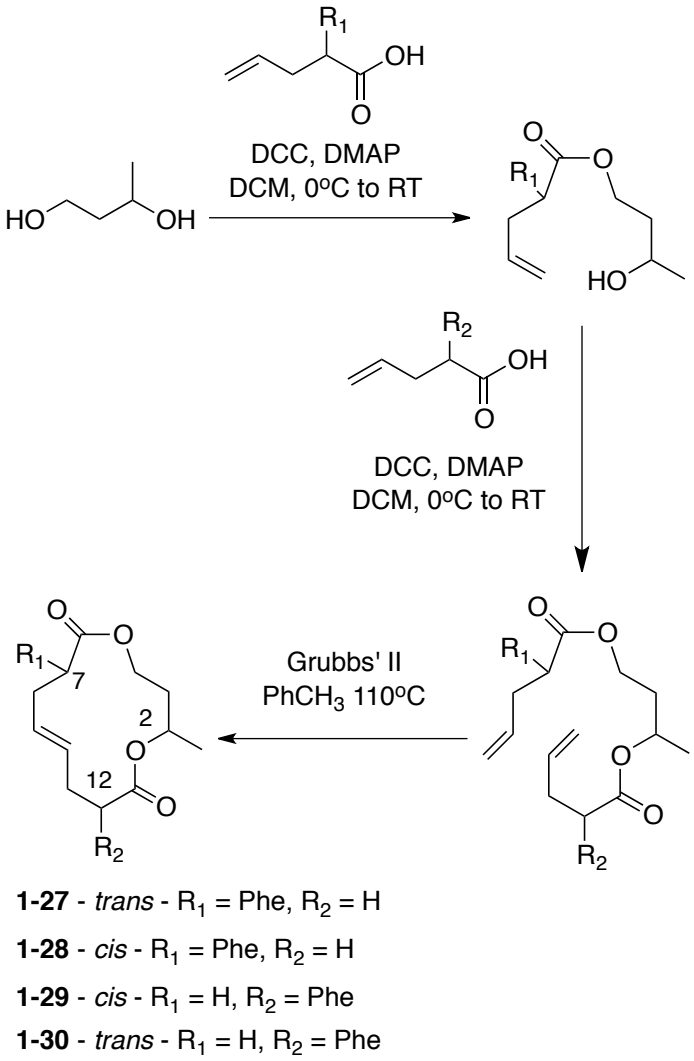

1-27 - *trans* - R_1 = Phe, R_2 = H

1-28 - *cis* - R_1 = Phe, R_2 = H

1-29 - *cis* - R_1 = H, R_2 = Phe

1-30 - *trans* - R_1 = H, R_2 = Phe

Scheme 1-5. Synthesis of C2, C7 and C7, C12 di-substituted [13]-macrodilactones.

Similar to the C7, C12 (compounds **1-25** and **1-26**) and C2, C4 (compounds **1-31** and **1-32**) di-substituted [13]-macrodilactones, we isolated four stereosiomers with two different shapes for C2, C7 and C2, C12 di-substituted macrocycles (Fig. 1-26 and 1-27). The difference in planar chiralities, shape and overall topologies of all the di-substituted [13]-macrodilcatones are evident in both the 2D maps and the crystal structures (Fig. 1-26 and 1-27).

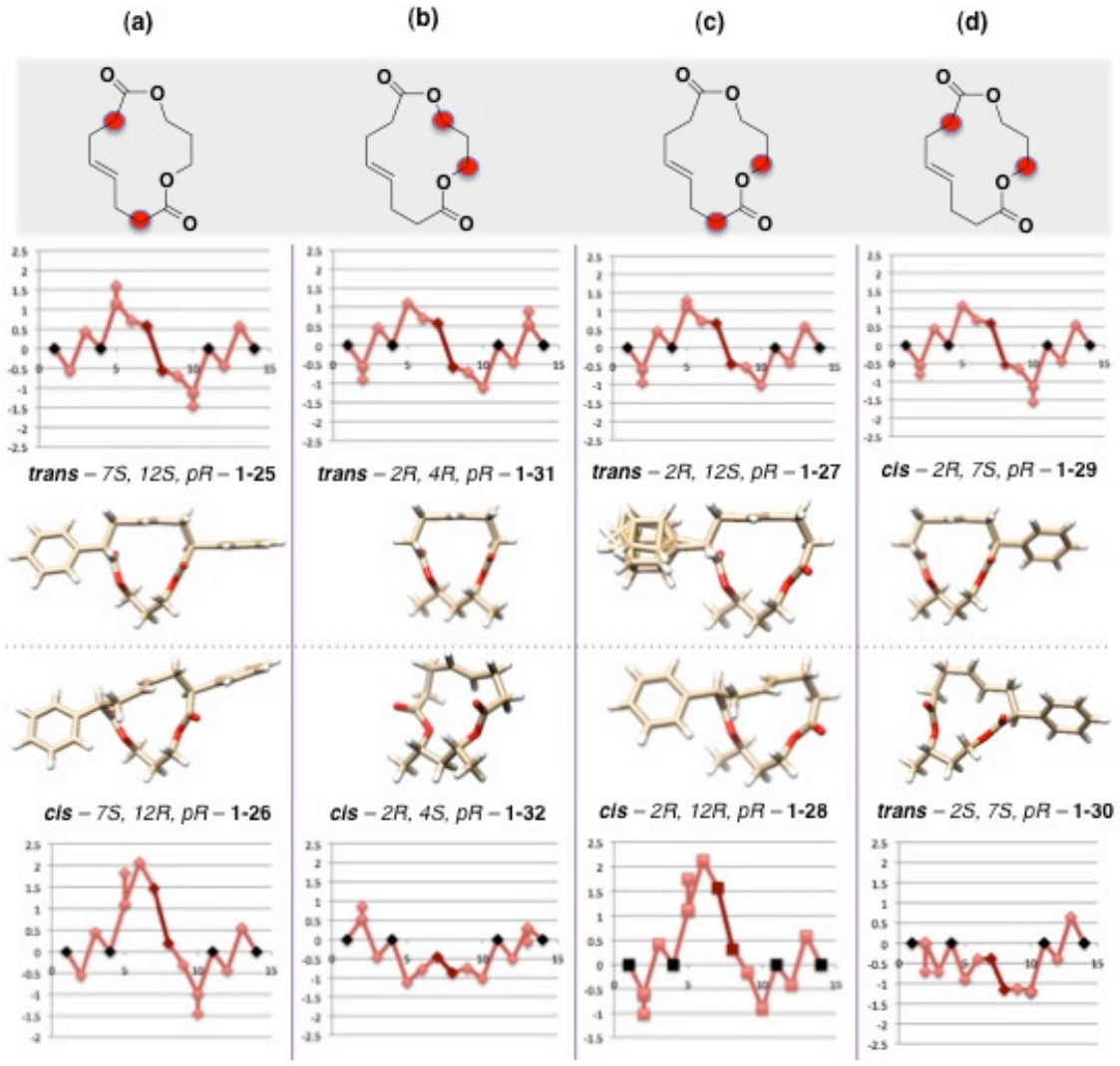

Fig. 1-26. Structural properties of di-substituted [13]-macrodilactones with various substitution patterns and with p*R* planar chiralities as shown by the X-ray crystal structures and 2D maps.

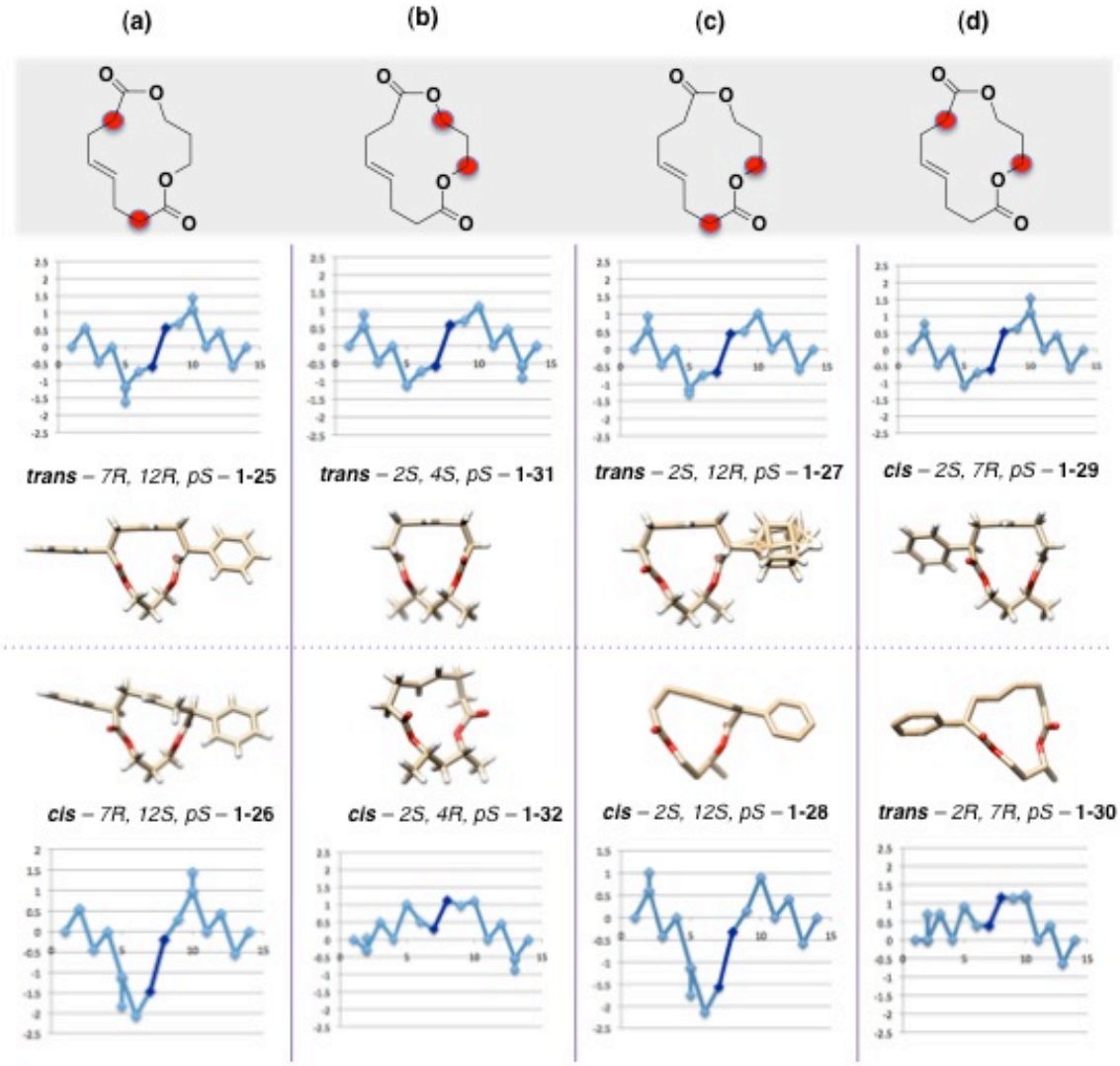

Fig. 1-27. Structural properties of di-substituted [13]-macrodilactones with various substitution patterns and with p*S* planar chiralities as shown by the X-ray crystal structures and 2D maps.

1.8.3 Effect of relative cis/trans configuration of substitutents on the topology of di-substituted 13-macrodilactones

With respect to the contribution of combinations of stereogenic centers to the shape of the [13]-macrodilactone, we initially hypothesized that the relative (***cis*** and ***trans***) configuration dictates the shape of the macrocyle based on our observations on both C7, C12 (Figs. 1-26a, 1-27a) and C2, C4 (Figs. 1-26c, 1-27c) macrocycles. We define the ***cis/trans*** configuration in a similar manner to the designation of ***cis/trans*** configuration in cyclohexane. The *trans* isomers adopted the ribbon shape and the ***cis*** adapted the alternate shape. This trend held true for the C2, C12 macrocyle (Figs. 1-26c, 1-27c) but did not apply to C2, C7 macrocyle where the *cis* configured macrocycle adopted the ribbon shape and the *trans* adopted an alternate shape (Figs. 1-26d, 1-27d). Based on the crystal structures of the new di-substituted macrocycles we obtained, it is clear that it is not the relative ***cis/trans*** configuration that determines whether the di-substituted [13]-macrodilactone will adopt th ribbon or the alternate shapes.

1.8.4 Effect of substitution pattern on the topology of di-substituted [13]-macrodilactones

The alternative shape adopted by the di-substituted [13]-macrodilactone seemed to depend on the substitution pattern. Macrocyles **1-26** and **1-28** with substitutions at C7, C12 and C2, C12 respectively adopted a similar shape as shown by their crystal structures and 2D maps (Figs. 1-26a, 1-27a and Figs. 1-26c, 1-27c). Macrocyles **1-26** and **1-28** have a five-atom alkene planar units instead of a four-atom planar units in the ribbon/triangular shape. Formation of a five-atom planar unit forced the alkene plane to

twist or deviate from the almost perpendicular orientation of the alkene plane (with respect to the molecular plane) in the ribbon/triangular shape. This deviation is clearly visualized through the positive migration of the alkene atoms in the 2D maps. Both **1-26** and **1-28** have a substituent at C12 suggesting that the configuration or the geometry at C12 stereogenic center can greatly influence the shape of [13]-macrodilactones. More specifically, the type of shape where a five-atom alkene planar unit was formed instead of the typical four-atom alkene planar unit is probably controlled by the configuration at C12.

Macrocycles **1-32** and **1-30** adopted yet another shape that is distinct from the ribbon/triangular shape and that of **1-26** and **1-28** as evident from their crystal structures and 2D maps (Figs. 1-26b, 1-27b and Figs. 1-26d, 1-27d). Pronounced difference can be seen in the orientation of the two carbonyl groups. The C=O groups in **1-32** and **1-30** are pointing in the same direction whereas in all the ribbon/triangular shape, the C=O groups are pointing in opposite direction. This orientation of carbonyl groups in **1-32** and **1-30** probably forced the alkene plane to again deviate from the molecular plane. The deviation from the molecular plane is also clearly visualized through the negative migration of the alkene atoms (as opposed to the positive deviation seen for **1-26** and **1-28**) in the 2D maps. Both **1-32** and **1-30** have a substituent at C2 suggesting that, similar to C12, the configuration or the geometry at C2 stereogenic center can greatly influence the shape of [13]-macrodilactone. More specifically, the type of shape where the two carbonyls are pointing in the same direction is probably controlled by the configuration at C2.

1.8.5 Effect of the interplay between configurations at the stereogenic centers and stereogenic plane on topology of di-substituted [13]-macrodilactones

Inspection of the crystal structures to explore some underlying general principle that apply to all the di-substituted [13]-macrodilactones – with regard to the relationship of configurations at stereogenic centers, planar chirality and shape - revealed that the trend observed in mono-substituted macrocycles applies to the di-substituted [13]-macrodilactones as well. For mono-substituted macrocycles, specific configuration at the stereogenic center (either *R* or *S*) resulted in only one planar chirality (either p*S* or p*R*). For C2 (and C4) streogenic center with methyl substituent, an *R* configuration should have a p*R* planar chirality while an *S* configuration should have a pS planar chirality. For the C7 (and C12) stereogenic center with phenyl substituent, it was the other way around. The *R* configuration should have a p*S* planar chirality while the *S* configuration should have a p*R* planar chirality (Table 2). As pointed out in the previous discussion, the appearance of the lack of correspondence between the general correlation of point and planar chirality for the C2-methyl and C7-phenyl mono-substituted macrocycles is due to the assignment of functional group prioritization based on CIP *R* and *S* designations. Specific geometry at the stereogenic center (point chirality) – driven by the preference for a pseudo-equatorial position – do indeed control the planar chirality. Similarly for the di-substituted [13]-macrodilactones, if both configurations at the stereogenic centers agree with the point to planar chirality correspondence (Table 1-2) observed for the mono-substituted [13]-macrodilactones – all of the substituents are in the pseudo-equatorial positions i.e. Figs. 1-26a – 7*S*, 12*S* p*R*; 1-26b – 2*R*, 4*R*, p*R*; 1-26c – 2*R*, 12*S*, p*R*; and 1-26d – 2*R*, 7*S*, p*R* - the macrocycle adopts the most stable 'ribbon' shape. If on the other

hand, one of the stereogenic centers does not agree with the point to planar chirality correspondence – underlined stereogenic centers - (i.e. Fig. 1-26a - 7*S*, <u>12*R*</u>, p*R*; 1-26b – 2*R*, <u>4*S*</u>, p*R*; 1-26c – 2*R*, <u>12*R*</u>, p*R*; and 1-26d – <u>2*S*,</u> 7*S*, p*R*), the macrocycle is forced to adopt a different or 'alternate' shape. For di-substituted [13]-macrodilactones, the proper configurations at the two stereogenic centers (point chiralities) and the olefenic stereogenic plane (planar chirality) is required to form the most stable conformation – the 'ribbon shape' - while if one of the substituents at the stereogenic centers has an incorrect point to planar chirality correspondence, a different shape is adopted.

1.8.6 Origin of the control of [13]-macrodilactone shape by two stereogenic centers

We used a computational method once again to further explore the driving force behind the preference for 'alternate' shape conferred by the incorrect point-to-planar chirality correspondence in the stereogenic elements on the [13]-macrodilactones. Using the C7, C12 di-substituted [13]-macrodilactone as an example, we used ground-state energy minimization to look at the energy associated with the 'ribbon' shape (*trans*-7*R*, 12*R*, p*S*) vs. the 'alternate' shape (*cis*-7*R*, 12*S*, p*S*) (Fig. 1-28). The 'alternate' shape is 1.7 kcal/mol higher in energy than the 'ribbon' shape. Using the same combination of configurations at stereogenic centers and at the stereogenic plane that gave rise to a non-ribbon shape (7*R*, 12*S*, p*S*) and forcing it to adopt a ribbon shape instead led to a conformation where one of the substituents is in pseudo-axial position (*trans* - 7*R*, 12*R*, p*S*). The specific combination 7*R*, 12*S*, p*S* adopted an alternate shape because adopting a ribbon shape is 2.4 kcal/mol higher in energy probably because of the transannular strain induced by a substituent in a pseudo-axial position. Similar to the mono-substituted

macrocycle, it looks like it's still the preference for pseudo-equatorial position that directs the type of shape adopted by the di-substituted [13]-macrodilactones.

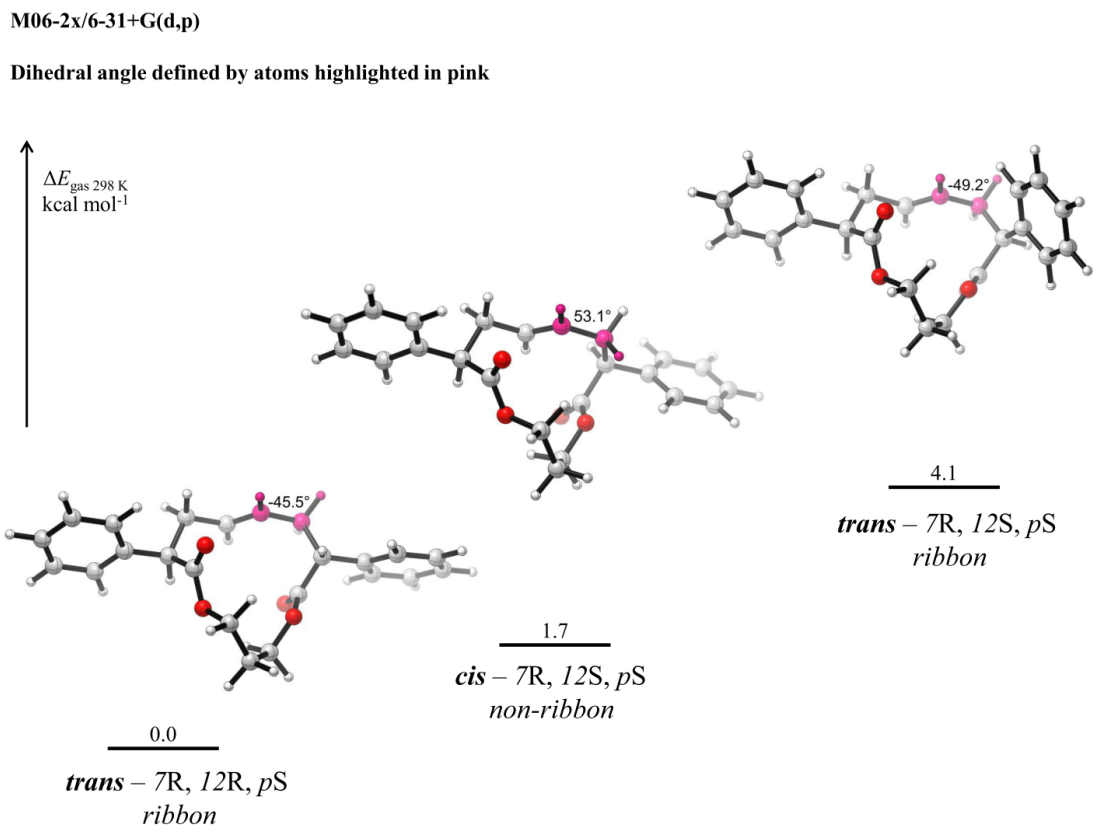

Fig. 1-28. Ground state energy minimization of C7, C12 disubstituted [13]-macrodilactones **1-25**.

1.8.7 Conclusion: Rules of [13]-macrodilactone topology and its potential application to other macrocyclic systems

Our systematic approach in investigating the interplay between the planar units and the stereogenic elements (point chirality and planar chirality) to the overall structure of [13]-macrodilactones has provided some valuable insights that we thought would be helpful in synthesizing macrocyles with designed structural properties. Although our

observations are primarily based on X-ray crystallography data and some computational methods and are thus bound by the limitations inherent to these types of analyses, we believe that the fundamental information we learned from the [13]-macrodilactone systems has some value. Below, we outlined the lessons we learned from this effort and discuss how it might be applicable to other ring systems with similar chemical composition.

1) *Unsubstituted [13]-macrodilactone adopts a single shape - a 'ribbon' shape when viewed from the side or a 'triangular' shape when viewed from the top of the molecular plane. This shape is rigidified by planar units alone. It exists as a pair of enantiomers brought about by stereogenic alkene plane.*

   For macrocycels that contain rigidifying planar units (macrolides, macrolactams, cyclic peptides or macrocycles with embedded alkene), there might be a preferred stable shape that is controlled by planar units alone. *E*-alkene containing macrocycles (without substituents) will most likely exist as a pair of planar enantiomers.

2) *There is a specific point-to-planar chirality correspondence when one stereogenic center is incorporated in [13]-macrodilactone regardless of the location and type of substituent. This means that a specific geometrical arrangement at a stereogenic center confers selectivity towards a specific planar chirality. If the substituent is considered to have the lowest priority based on CI specifications for assigning the configurations at stereogenic centers, the point-to-planar chirality correspondence is R to pR and S to pS. This selectivity is driven by the preference of the substituents to*

be oriented away from the ring or in pseudo-equatorial position. Regardless of type and location of stereogenic center, [13]-macrodilactone with one substituent adopted the same ribbon shape.

This observation implies that for *E*-alkene containing macrocyles, synthesizing macrocyles with a specific planar chirality (either p*S* or p*R*) is possible by incorporating a stereogenic center around the ring with a specific configuration (either *R* or *S*). For macrocycles that contain rigidifying planar units (macrolides, macrolactams, cyclic peptides or macrocycles with embedded alkene), changing the shape of macrocycles might not be possible by just incorporating one stereogenic center around the ring.

3) *All the di-substituted [13]-macrodilactone gave four different streoisomers with two different shapes (ribbon and various alternate shapes). A proper configuration - controlled by the preference for pseudo-equatorial position - at both stereogenic centers and stereogenic plane is required to get the most stable ribbon shape. However, if one configuration at either setreogenic centers or the stereogenic plane do not match, an alternate shape is adopted which varies depending on the substitution pattern.*

In designing macrocycles with different shapes, at least two stereogenic centers might be needed to be incorporated in the ring. The most stable shape defined by the planar units alone is accessible only if all the substituents around the ring are in pseudo-equatorial position. If one of the substituents is in pseudo-axial position, an 'alternate' shape will be adopted. Moreover, various 'alternate' shapes can be

accessed depending on the substitution pattern. This observation we believe, will be very helpful for generating macrocyclic compound libraries with varied skeletons and for medicical chemists who are trying to optimze the biological and pharmacological profiles of bioactive macrocyles.

1.9 Experimental Section

Experimental procedures and characterization of compounds in Chapter 1

General

Reactions were monitored using TLC. UV light, *p*-anisaldehyde, potassium permanganate ($KMnO_4$) or ceric ammonium molybdate (CAM) solutions were used for visualization. Chromatography was performed on silica gel and solvent systems used were based on the R_f values. ^{1}H NMR spectra (400 MHz) were referenced to $CDCl_3$ (δ_H 7.27 ppm) and ^{13}CNMR spectra (100 MHz) were referenced to $CDCl_3$ (δ_C 77.23 ppm).

Sequential Acylations

Method A:

Dicyclohexylcarbodiimide (DCC) (1.09 mmol) and N,N-dimethylaminopyridine (DMAP) (0.3 mmol) in DCM (7 mL) were stirred at 0 °C. 4-pentenoic acid (1 mmol) was added and the mixture was stirred at the same temperature for 30 minutes until a white suspension was observed in the flask. 1,3-propanediol (1 mmol) in DCM (3 mL) was then added to the reaction mixture and stirred overnight at room temperature. The mixture was filtered through a celite and solvent was removed from the filtrate under reduced pressure. The crude residue was purified by silica gel column chromatography (3:1 Hex:EtOAc) to give the monoacylated product.

Method B:

DCC (1.09 mmol) and DMAP (0.3 mmol) were added in DCM (40 mL) and cooled to 0°C. The acid of choice (1 mmol) was added to the solution and stirred at the same temperature for 30 minutes. The monoacylated product (1 mmol) from the first acylation was then added to the mixture and stirred overnight at room temperature. The reaction mixture was filtered through celite and the solvent of the filtrate was removed under reduced pressure. Crude residue was purified by silica gel column chromatography to get the diene.

One-pot acylation

In a round bottom flask, DCC (0.23 g, 1.09 mmol) and DMAP (.037 g, 0.300 mmol) were dissolved in DCM (40mL), and the solution was cooled to 0°C. The acid of choice (1.00 mmol) was added and stirred at the same temperature for 30 minutes. Either 1,3-butanediol or 1,3-propanediol (0.500 mmol) in DCM (10 mL) was then added to the mixture and stirred overnight at room temperature. The mixture was then filtered through celite. The solvent of the filtrate was removed under reduced pressure and the residue was purified by silica gel column chromatography to get the diene.

Ring Closing Metathesis

Grubbs' second-generation catalyst (0.050 mmol) was added to a solution of the diene (1 mmol) in toluene (100 mL). The mixture was heated to reflux at 110 °C overnight. The toluene was removed under reduced pressure and the crude product was purified by column chromatography.

DMDO Epoxidation (Lee, D.; Sello, J. K.; Schreiber S. L. *J. Am. Chem. Soc.* **1999**, *121*, 10648-10649)

Excess amount of $NaHCO_3$ (0.450 g, 0.94 mmol) and Oxone (0.450 g, 0.19 mmol) was added to a solution of [13]-macrodilactone (racemic or chiral) (75 mg) in acetone:H_2O:DCM (1:1:1, 15 mL) at 0 °C. The resulting heterogeneous mixture was stirred for 3 h at 0 °C and extracted with DCM. The epoxide was purified using column chromatography.

Characterization

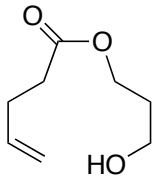

3-hydroxypropyl 4-pentenoate. The synthesis of this compound followed the general monoacylation procedure (Method A) to give 3-hydroxypropyl 4-pentenoate in 52% yield as a colorless oil (1.0 mmol scale). R_f 0.2 (30% EtOAc:Hex); ^{1}HNMR ($CDCl_3$) 400 MHz. δ 5.82 (ddd, 1H, *J*= 10.4, 6.3, 6.3, 6.3 Hz), 5.08 (dd, 1H, *J* = 16.6, 16.6, 0 Hz), 5.02 (dd, 1H, *J*= 10.2, 10.2, 0 Hz), 4.25 (t, 2H, *J* = 6.1 Hz), 3.69 (m 2H), 2.80 (s, 1H), 2.41 (m, 4H), 1.88 (qn, 2H, *J* = 6.1 Hz); ^{13}C NMR ($CDCl_3$) 100 MHz δ 173.6, 136.6, 115.6, 61.5, 59.0, 33.6, 31.7, 28.9; TOF HRMS (DART) m/z calcd for $C_9H_{16}O_3$ $(M+H)^+$ 173.1099, found 173.1191

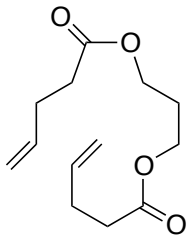

1-18. The synthesis of this compound can follow either the general procedure for synthesizing dienes (Method A and then Method B) or a one-pot acylation. The general route for dienes gave a better yield of (96%) in 26.0 mmol scale as colorless oil. R_f 0.58 (20% EtOAc:Hex); ^{1}HNMR (400 MHz, CDCl3) δ 5.83 (dddd/dq, 2H, *J*= 23.4, 6.4, 6.4, 6.4), 5.04 (ddd, 4H, *J*= 24.7, 17.1, 1.3), 4.17 (ddd, 4H, *J*= 6.42, 6.42, 0), 2.42 (m, 8H),

1.98 (dddd/tt, 2H, *J*= 6.3, 6.3, 6.3, 6.3); ^{13}C NMR (100 MHz, CDCl3) δ 173.2, 136.8, 115.8, 61.2, 33.7, 29.1, 28.2; TOF HRMS (DART) m/z calcd for $C_{13}H_{20}O_4$ $(M+H)^+$ 241.1439, found 241.1425

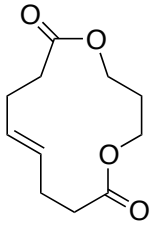

1-20. Followed the general RCM method to give the product in 54% yield and as a white crystalline solid (2.08 mmol scale). m.p. 61.2 – 61.7 °C; R_f 0.34 (20% EtOAc:Hex); ^{1}HNMR (400 MHz, CDCl3) δ 5.44 (m, 2H), 4.18 (ddd/dt, 4H, *J*= 5.7, 5.7, 0), 2.33 (m, 8H), 2.02 (dddd/tt, 2H, *J*= 6.1, 6.1, 6.1, 6.1); ^{13}C NMR (100 MHz, CDCl3) δ 173.9, 130.0, 60.7, 34.4, 28.7, 26.1; TOF HRMS (DART) m/z calcd for $C_{11}H_{16}O_4$ $(M+H)^+$ 213.1127, found 213.1158

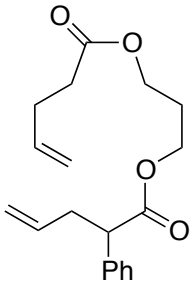

***rac*-1-21.** The synthesis of this compound followed the general method of dienes through monoacylation (Method B) in 50% yield and as a clear yellowish oil (0.63 mmol). Rf 0.6 (20% EtOAc:Hex); 1HNMR (CDCl3) 400 MHz. δ 7.33 (m, 4H), 7.28 (m, 1H), 5.83 (m, 1H), 5.74 (dddd/ddt, 1H, *J*= 17.0, 10.3, 6.7, 6.7), 5.08 (m, 2H), 5.01 (dd, 2H, *J*= 10.4,

5.0), 4.16 (ddd, 2H, *J*= 17.5, 11.34, 6.3), 4.08 (m, 2H), 3.66 (dd, 1H, *J*= 8.5, 7.1), 2.85 (ddd, 1H, *J*= 14.8, 8.2, 8.2), 2.54 (ddd, 1H, *J*= 13.8, 6.8, 6.8), 2.39 (ddd, 4H, *J*= 15.5, 11.35, 4.17), 1.93 (dddd/dq, 2H, *J*= 6.48, 6.48, 6.48, 6.48); 13C NMR (CDCl3) 100 MHz δ 173.5, 173.1, 138.7, 136.8, 135.4, 128.9, 128.1, 127.6, 117.3, 115.8, 61.5, 61.0, 51.7, 37.7, 33.7, 29.1, 28.1; TOF HRMS (DART)*m/z* calcd for C19H24O4 (M+H)+ 317.1753, found 317.1732.

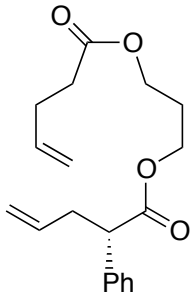

***S*-1-21.** Followed the general method of dienes through monoacylation (method A and then method B) in 75% yield as a yellowish oil (0.79 mmol). R_f 0.6 (20% EtOAc:Hex); $[a]_D$ +257.4° (c 1.0, CH_2Cl_2);^{1}HNMR ($CDCl_3$) 400 MHz. δ 7.30 (m, 5H), 5.80 (m, 2H), 5.08 (m, 2H), 5.02 (dd, 2H, *J*=10.3, 4.9), 4.16 (ddd, 2H, *J*= 17.57, 11.09, 6.31), 4.07 (m, 2H), 3.66(dd, 1H, *J*= 8.5, 7.0), 2.84 (ddd, 1H, *J*= 15.01, 8.07, 8.07), 2.54 (ddd, 1H, *J*= 13.64, 6.74, 6.74), 2.38 (ddd, 4H, *J*= 14.71, 11.34, 4.35), 1.92 (dddd/dq, 2H, *J*= 6.37, 6.37, 6.37, 6.37); ^{13}C NMR ($CDCl_3$) 100 MHz δ 173.5, 173.1, 138.7, 136.8, 135.4, 128.8, 128.1, 127.6, 117.2, 115.7, 61.5, 61.0, 51.7, 37.6, 33.7, 29.0, 28.1; TOF HRMS (ESI) *m/z* calcd for C19H24O4 (M+Na)+ 339.1572, found 339.1556.

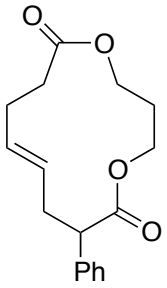

***rac*-1-22.** Followed the general RCM method to give the product in 54% yield and as a white crystalline solid. m.p. 78-79 °C; R_f 0.4 (20% EtOAc:Hex); ^{1}HNMR ($CDCl_3$) 400 MHz. δ 7.37 (d, 2H, *J*= 7.1), 7.31 (dd, 2H, *J*= 7.1, 7.1), 7.26 (dd, 1H, *J*= 3.1, 3.1), 5.55 (m, 2H), 4.54 (m, 1H), 4.44 (m, 1H), 4.01 (ddd/dt, 1H, *J*= 8.2, 4.1, 4.1), 3.83 (ddd/dt, 1H, *J*= 8.2, 4.1, 4.1), 3.60 (dd, 1H, *J*= 12.6, 2.7), 2.77 (ddd/dt, 1H, *J*= 12.9, 12.0, 8.1), 2.35 (m, 5H), 2.03 (m, 2H); ^{13}C NMR ($CDCl_3$) 100 MHz δ 174.2, 173.9, 139.1, 131.1, 129.1, 128.9, 127.9, 127.6, 60.6, 60.4, 52.1, 37.9, 34.3, 28.8, 26.0; anal. for $C_{17}H_{20}O_4$, C 70.78, H 6.96, O 22.26, found C 70.86, H 6.96.

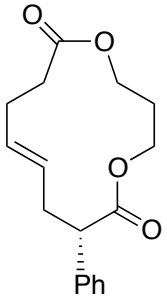

7*S*,p*R*-1-22. Followed the general method of RCM in 25% yield (scale) as a white solid. m.p. 72-74 °C; $[a]_D$ +2.6° (c 1.0, CH_2Cl_2); R_f 0.4 (20% EtOAc:Hex); ^{1}HNMR ($CDCl_3$) 400 MHz. δ 7.39 (d, 2H, *J*= 7.2), 7.23 (dd, 2H, *J*= 7.2, 7.2), 7.26 (m, 1H), 5.56 (m, 2H), 4.54 (m, 1H), 4.46 (m, 1H), 4.04 (ddd/dt, 1H, *J*= 8.4, 4.0, 4.0), 3.86 (ddd/dt, 1H, *J*= 8.4, 4.0, 4.0), 3.62 (dd, 1H, *J*= 12.6, 2.9), 2.79 (ddd/dt, 1H, *J*= 12.9, 12.9, 8.2), 2.37 (m, 5H),

2.05 (m, 2H);); ^{13}C NMR ($CDCl_3$) 100 MHz δ 174.1, 173.9, 139.0, 131.0, 129.0, 128.8, 127.9, 127.6, 60.6, 60.4, 52.0, 37.9, 34.3, 28.7, 26.0; TOF HRMS (ESI) *m/z* calcd for $C_{17}H_{20}O_4$ $(M+Na)_+$ 311.1259, found 311.1253.

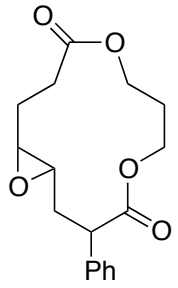

***rac*-1-23**. Compound *rac*-**1-22** was epoxidized using a procedure for in situ generation of DMDO as described to give *rac*-**1-23** in 64% yield (0.26 mmol) and as a white solid. m.p. 100-102 °C; R_f 0.2 (20% EtOAc:Hex); ^{1}HNMR ($CDCl_3$) 400 MHz. δ 7.30 (m, 5H), 4.82 (m, 2H), 3.91 (ddd/dt, 1H, *J*= 8.1, 3.7, 3.7), 3.72 (m, 2H), 2.87 (ddd, 2H, *J*= 8.8, 8.8, 2.6), 2.47 (dd, 2H, *J*= 8.24, 5.04), 2.24 (m, 2H), 2.03 (m, 3H), 1.60 (m, 1H); ^{13}C NMR ($CDCl_3$) 100 MHz δ 173.4, 172.9, 139.1, 129.0, 127.7, 127.6, 60.2, 59.5, 58.5, 57.6, 47.8, 36.7, 29.6, 26.9, 26.3; TOF HRMS (ESI) *m/z* calcd for $C_{17}H_{20}O_5$ $(M+Na)_+$ 327.1208, found 327.1206.

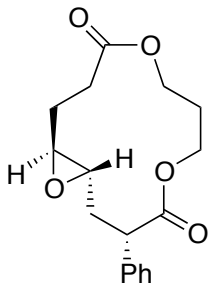

7*S*,p*R*-1-23. Compound *7S,pR*-**1-22** was epoxidized using a procedure for in situ generation of DMDO as described to give **7*S*,p*R*-1-23** in 67% yield and as a white solid (0.25 mmol). mp 114-118 °C; $[a]_D$ +120.3° (c 1.0, CH_2Cl_2); R_f 0.2 (20% EtOAc:Hex); ^{1}HNMR ($CDCl_3$) 400 MHz. δ 7.29 (m, 5H), 4.83 (m, 2H), 3.92 (ddd/dt, 1 H, *J*= 8.2, 4.3, 4.3), 3.73 (m, 2H), 2.87 (ddd, 2H, *J*= 8.8, 8.8, 2.6), 2.47 (dd, 2H, *J*= 8.2, 5.3), 2.25 (m, 2H), 2.06 (m, 2H), 2.00 (ddd/dt, 1H, *J*= 12.9, 9.6, 9.6), 1.61 (m, 1H); ^{13}C NMR ($CDCl_3$) 100 MHz δ 173.4, 172.9, 139.1, 129.1, 127.7, 127.6, 60.2, 59.5, 58.5, 57.6, 47.8, 36.7, 29.6, 26.9, 26.3; TOF HRMS (ESI) *m/z* calcd for $C_{17}H_{20}O_5$ $(M+Na)^{+\cdot}$ 327.1208, found 327.1216.

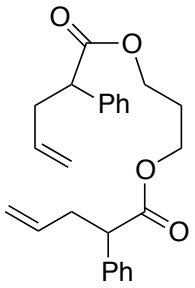

1-24. Followed the general procedure of diene through diacylation in 46% yield and clear yellowish oil (2.55 mmol). R_f 0.8 (20% EtOAc:Hex); ^{1}HNMR ($CDCl_3$) 400 MHz. δ 7.22 (m, 10H), 5.63 (dddd/dt, 2H, *J*= 17.3, 10.3, 7.0, 7.0), 5.00 (dd, 2H, *J*= 17.1, 1.3), 4.92 (dd, 2H, *J*= 10.2, 0), 3.96 (m, 4H), 3.54 (dd, 2H, *J*= 7.9, 7.9), 2.73 (ddd, 2H, *J*= 14.58, 8.05, 8.05), 2.43 (ddd, 2H, *J*= 13.93, 6.75, 6.75), 1.77 (dddd/tt, 2H, *J*= 6.13, 6.13, 6.13, 6.13); ^{13}C NMR ($CDCl_3$) 100 MHz δ 173.5, 138.7, 135.4, 128.9, 128.1, 127.6, 117.3, 61.3, 51.7, 37.7, 28.1; TOF HRMS (ESI) *m/z* calcd for $C_{25}H_{28}O_4$ $(M+Na)^{+\cdot}$ 365.1753, found 365.1749.

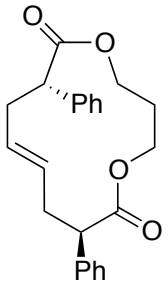

1-25. Followed the general method of RCM in 47% yield (0.45 mmol) and as a white solid. m.p. 172-174 °C; R_f 0.56 (20% EtOAc:Hex); ^{1}HNMR ($CDCl_3$) 400 MHz. δ 7.33 (m, 10H), 5.64 (ddd/dt, 2H, *J*= 3.67, 3.67, 0), 4.67 (m, 2H), 3.80 (ddd/dt, 2H, *J*= 7.09, 3.17, 3.17), 3.62 (dd, 2H, *J*= 12.50, 2.14), 2.82 (m, 2H), 2.28 (dd, 2H, *J*= 12.62, 0), 2.03 (m, 2H); ^{13}C NMR ($CDCl_3$) 100 MHz δ 174.1, 139.0, 130.3, 128.9, 127.8, 127.6, 59.7, 51.8, 38.1, 25.5; TOF HRMS (DART) m/z calcd for $C_{23}H_{24}O_4$ $(M+H)^+$ 365.1753, found 365.1749

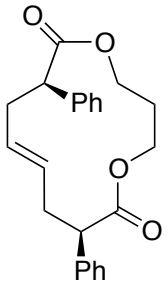

1-26. Followed the general method of RCM in 20% yield and as a white solid. m.p. 147-156 °C; R_f 0.44 (20% EtOAc:Hex); ^{1}HNMR ($CDCl_3$) 400 MHz. δ 7.33 (m, 10 H), 5.74 (ddd, 2H, *J*= 2.84, 2.84, 0), 4.41 (ddd, 2H, *J*= 11.37, 5.71, 5.71), 4.09 (ddd, 2H, *J*= 10.93, 5.15, 5.15), 3.75 (ddd, 2H, *J*= 12.17, 3.31, 0), 2.78 (m, 2H), 2.40 (dd, 2H, *J*= 13.57, 0), 2.08 (dddd/dq, 2H, *J*= 5.20, 5.20, 5.20, 5.20); ^{13}C NMR ($CDCl_3$) 100 MHz δ 174.1, 139.1,

129.7, 128.9, 128.1, 127.7, 63.1, 52.4, 36.9, 27.3; TOF HRMS (DART) m/z calcd for $C_{23}H_{24}O_4$ $(M+H)^+$ 365.1753, found 365.1748.

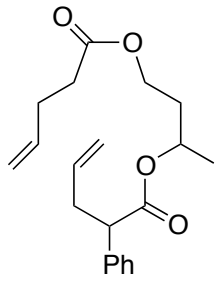

diacylated diene precursor of 1-27 and 1-28. Followed the general method of dienes through monoacylation of 1,3 butanediol first with pentenoic acid to get the monoacylated 1,3 butanediol (method A) and then method B using 2-phenyl pentenoic acid in 62% yield as a yellowish oil (0.8 mmol). R_f 0.8 (20% EtOAc:Hex); ^{1}HNMR (400 MHz, CDCl3) δ (m, 5H), 5.77 (m, 2H), 5.03 (m, 5H), 4.09 (m, 1H), 3.99 (ddd, 1H, *J*= 11.4, 6.1, 6.1), 3.83 (ddd, 1H, *J*= 13.9, 7.8, 6.1), 3.63 (m, 1H), 2.83 (m, 1H), 2.54 (m, 1 H), 2.39 (m, 1H), 2.34, (m, 2H), 1.83 (m, 2H), 1.25 (m, 2H), 1.15 (m, 3H); ^{13}C NMR (100 MHz, CDCl3) δ 173.1, 138.9, 136.9, 135.5, 128.9, 128.0, 127.6, 117.1, 115.7, 68.5, 60.7, 51.8, 37.6, 34.9, 33.6, 29.0, 20.3, 20.0; TOF HRMS (DART) m/z calcd for $C_{23}H_{26}O_4$ $(M+H)^+$ 331.1909, found 331.1921.

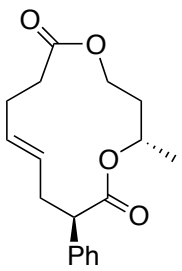

1-27. Obtained using the general RCM procedure in 21.2% yield (0.5 mmol) and as a white solid. m.p. 85.0 – 85.7 °C; R_f 0.48 (20% EtOAc:Hex); ^{1}HNMR (400 MHz, CDCl3) δ 7.28 (m, 5H), 5.52 (m, 2H), 5.09 (ddd, 1H, *J*= 10.6, 6.1, 3.8), 4.34 (ddd, 1H, *J*= 12.1, 12.1, 3.6), 3.94 (ddd, 1H, *J*= 11.2, 5.2, 2.2), 3.54 (ddd, 1H, *J*= 12.6, 2.5, 0), 2.79 (ddd, 1H, *J*= 13.0, 13.0, 9.3), 2.30 (m, 5H), 2.01 (m, 1H), 1.78 (m, 1H), 1.16 (dd, 3H, *J*= 6.24, 0); ^{13}C NMR (100 MHz, CDCl3) δ 174.1, 173.3, 139.1, 131.7, 129.12, 128.9, 127.6, 127.5, 67.3, 60.5, 52.2, 37.6, 34.5, 33.5, 29.2, 20.5; TOF HRMS (DART) m/z calcd for $C_{18}H_{22}O_4$ $(M+H)^+$ 303.1596, found 303.1005

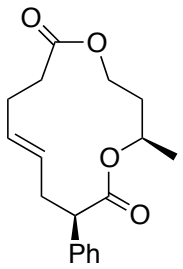

1-28. Obtained using the general RCM procedure in 4.6% yield (0.5 mmol) and as a white solid. m.p. 96.3 – 96.9 °C; R_f 0.42 (20% EtOAc:Hex); ^{1}HNMR (400 MHz, CDCl3) δ 7.30 (m, 5H), 5.60 (m, 2H), 5.12 (ddd, 1H, *J*= 9.9, 6.3, 3.7), 4.16 (m, 1H), 4.07 (m, 1H), 3.83 (ddd, 1H, *J*= 11.7, 3.6, 0), 2.70 (ddd, 1H, *J*= 15.7, 11.7, 4.3), 2.39 (m, 5H), 1.96 (dddd, 2H, *J*= 8.9, 8.9, 4.2, 4.2), 1.20 (dd, 3H, *J*= 6.4, 0); ^{13}C NMR (100 MHz, CDCl3) δ 174.2, 172.7, 139.4, 129.5, 128.9, 128.6, 128.0, 127.5, 69.4, 61.1, 52.2, 35.4, 34.0, 29.7, 20.8; TOF HRMS (DART) m/z calcd for $C_{18}H_{22}O_4$ $(M+H)^+$ 303.1596, found 303.1606

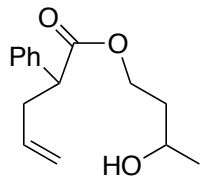

3-hydroxybutyl 2-phenyl-4-pentenoate. The synthesis of this compound followed the general monoacylation procedure (Method A) to give 3-hydroxybutyl 2-phenyl-4-pentenoate in 44% yield as a colorless oil (2.0 mmol scale). R_f 0.2 (30% EtOAc:Hex); ^{1}HNMR ($CDCl_3$) 400 MHz δ 7.30 (m, 5H), 5.74 (ddt/dddd, 1H, *J* = 17.2, 10.5, 6.9, 6.9), 5.09 (dd, 1H, *J* = 17.2, 0.0), 5.03 (dd, 1H, *J* = 10.3, 0), 4.34 (ddt/ dddd, 1H, *J* = 11.4, 8.4, 5.0, 5.0), 4.13 (ddt/ dddd, 1H, *J* = 11.2, 7.7, 5.6, 5.6), 3.74 (m, 1H), 3.66 (dd, 1H, *J* = 8.7, 6.9), 2.85 (ddd, 1H, *J* = 15.7, 8.5, 7.6), 2.54 (m, 1H), 2.19 (m, 1H), 1.71 (m, 2H), 1.16 (dd, 3H, *J*= 6.0, 4.0); ^{13}C NMR ($CDCl_3$) 100 MHz δ 174.0, 135.4, 128.9, 128.1, 127.6, 117.3, 65.1, 62.4, 62.3, 51.8, 38.2, 37.6, 23.6; TOF HRMS (DART) m/z calcd for $C_{15}H_{20}O_3$ $(M+H)^+$ 249.1491, found 249.1502

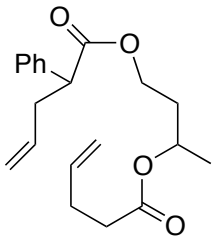

diacylated diene precursor of 1-29 and 1-30. Followed the general method of dienes through monoacylation of 1,3 butanediol first with pentenoic acid to get the monoacylated 1,3 butanediol (method A) and then method B using 2-phenyl pentenoic acid in 62% yield as a yellowish oil (0.8 mmol). R_f 0.6 (20% EtOAc:Hex); ^{1}HNMR

($CDCl_3$) 400 MHz δ 7.26 (m, 5H), 5.72 (m, 2H), 5.00 (m, 5H), 4.09 (m, 2H), 3.62 (dd, 1H, *J*= 8.3, 7.1), 2.82 (ddd, 1H, *J* = 14.8, 7.6, 7.6), 2.51 (ddd, 1H, *J* =13.9, 6.7, 6.7), 2.35 (dd, 2H, *J* = 2.5, 0), 2.33 (dd, 2H, *J* = 2.6, 0.0), 2.20 (m, 2H), 1.17 (dd, 3H, *J* = 8.5, 6.5); ^{13}C NMR ($CDCl_3$) 100 MHz δ 173.4, 172.4, 138.6, 136.7, 135.3, 128.7, 128.0, 127.4, 117.1, 115.6, 67.9, 61.3, 51.6, 37.5, 34.8, 33.8, 29.0, 20.1; TOF HRMS (DART) m/z calcd for $C_{20}H_{26}O_4$ $(M+H)^+$ 331.1409, found 331.1920.

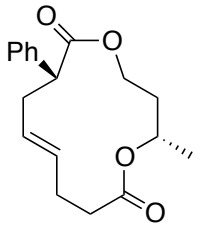

1-29. Obtained using the general RCM procedure in 13% yield (0.5 scale) and as a white solid. m.p. 112-113 °C; R_f 0.52 (20% EtOAc:Hex); ^{1}HNMR ($CDCl_3$) 400 MHz δ 7.30 (m, 5H), 5.52 (ddd/dt, 2H), *J* = 8.8, 4.8, 4.8), 5.12 (m, 1H), 4.39 (ddd, 1H, *J*= 14.9, 11.1, 3.6), 3.76 (ddd, 1H, *J* = 11.1, 5.7, 1.4), 3.54 (ddd, 1H, *J*= 12.5, 2.6, 0.0), 2.74 (ddd, 1H, *J* = 13.0, 13.0, 9.1), 2.41 (m, 2H), 2.27 (m, 3H), 2.02 (m, 1H), 1.75 (m, 1H), 1.29 (dd, 3H, *J* = 6.2, 0); ^{13}C NMR ($CDCl_3$) 100 MHz δ 174.4, 172.9, 139.0, 130.9, 129.7, 128.8, 127.9, 127.6, 66.8, 60.5, 52.1, 38.3, 34.3, 33.5, 28.2, 20.7; TOF HRMS (DART) m/z calcd for $C_{18}H_{22}O_4$ $(M+H)^+$ 303.1596, found 303.1594

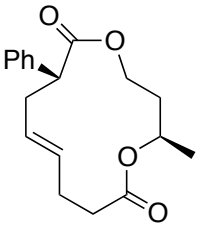

1-30. Obtained using the general RCM procedure in 17% yield (0.5 mmol) and as a white solid. m.p. 75 °C; R_f 0.47 (20% EtOAc:Hex); ^{1}HNMR ($CDCl_3$) 400 MHz δ 7.31(m, 5H), 5.65 (ddd/dt, 2H, *J* = 5.9, 5.9, 5.9), 5.13 (m, 1H), 4.33 (ddd, 1H, *J* = 11.6, 6.8, 3.4), 3.70 (ddd, 1H, *J* = 0, 3.7, 11.6), 2.68(m, 1H), 2.41 (m, 4H), 2.26 (m, 1H), 1.96 (m, 2H), 1.28 (dd, 3H, *J* = 6.2, 0.0); ^{13}C NMR ($CDCl_3$) 100 MHz δ 174.1, 173.4, 139.1, 130.9, 129.2, 128.9, 128.3, 127.5, 70.1, 62.7, 52.7, 36.7, 35.0, 34.3, 27.5, 20.9; TOF HRMS (DART) m/z calcd for $C_{18}H_{22}O_4$ $(M+H)^+$ 303.1596, found 303.1637

X-ray Crystallography Data

Procedure for determination of RMSDs

The root mean square deviations (RMSDs) were produced with the structure overlay feature of the Mercury software package. Pairs of atoms were selected to calculate the square root of the mean square differences between atomic coordinates. Our approach focused on the 13 atoms of the macrocycle in compound **1**. These coordinates were mapped onto the corresponding atom positions of compounds **4**, **6**, and **7**. All of the compounds reported here crystallized as racemic mixtures. The coordinates were carefully inspected to insure the average RMSD between two sets of coordinates reflected corresponding conformations in the alkene and ester functional groups.

X-ray Crystallography Data

Procedure for determination of RMSDs

The root mean square deviations (RMSDs) were produced with the structure overlay feature of the Mercury software package. Pairs of atoms were selected to calculate the square root of the mean square differences between atomic coordinates. Our approach focused on the 13 atoms of the macrocycle in compound **1-20**. These coordinates were mapped onto the corresponding atom positions of compounds **1-22**, **1-25**, and **1-26**. All of the compounds reported here crystallized as racemic mixtures. The coordinates were carefully inspected to insure the average RMSD between two sets of coordinates reflected corresponding conformations in the alkene and ester functional groups.

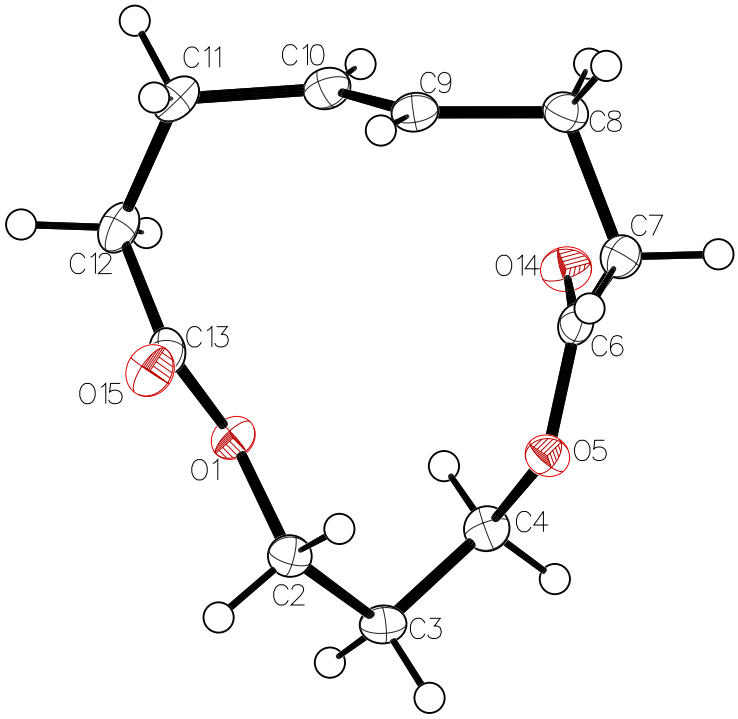

Fig. 1-29 A thermal ellipsoid plot of **1-19** (spider-15025) at a 50% probability level. The full numbering scheme is shown. Hydrogen atoms are depicted as spheres.

Table 1-3. Crystal data and structure refinement for **1-19** (spider-15025).

Identification code	spider-15025	
Empirical formula	$C_{11}H_{16}O_4$	
Formula weight	212.24	
Temperature	93(2) K	
Wavelength	0.71075 Å	
Crystal system	Monoclinic	
Space group	$P\,2_1/c$	
Unit cell dimensions	a = 12.9215(9) Å	α = 90°.
	b = 9.3726(2) Å	β = 91.858(6)°.
	c = 8.9925(2) Å	γ = 90°.
Volume	1088.49(8) $Å^3$	
Z	4	
Density (calculated)	1.295 Mg/m^3	
Absorption coefficient	0.098 mm^{-1}	
F(000)	456	
Crystal size	0.410 x 0.380 x 0.260 mm^3	
Crystal color and habit	Colorless Block	
Diffractometer	Rigaku R-AXIS RAPID imaging plate	
Θ range for data collection	3.140 to 27.474°.	
Index ranges	$-16 \le h \le 16$, $-12 \le k \le 12$, $-11 \le l \le 11$	
Reflections collected	42983	
Independent reflections	2492 [R(int) = 0.0300]	
Observed reflections (I > 2σ(I))	2255	
Completeness to θ = 25.242°	99.9 %	
Absorption correction	Semi-empirical from equivalents	
Max. and min. transmission	1.000 and 0.945	
Solution method	SHELXS-2013 (Sheldrick, 2013)	
Refinement method	SHELXL-2014/7 (Sheldrick, 2014)	
Data / restraints / parameters	2492 / 0 / 136	
Goodness-of-fit on F^2	1.071	
Final R indices [I>2σ(I)]	R1 = 0.0320, wR2 = 0.0807	
R indices (all data)	R1 = 0.0349, wR2 = 0.0823	
Largest diff. peak and hole	0.311 and -0.174 $e.Å^{-3}$	

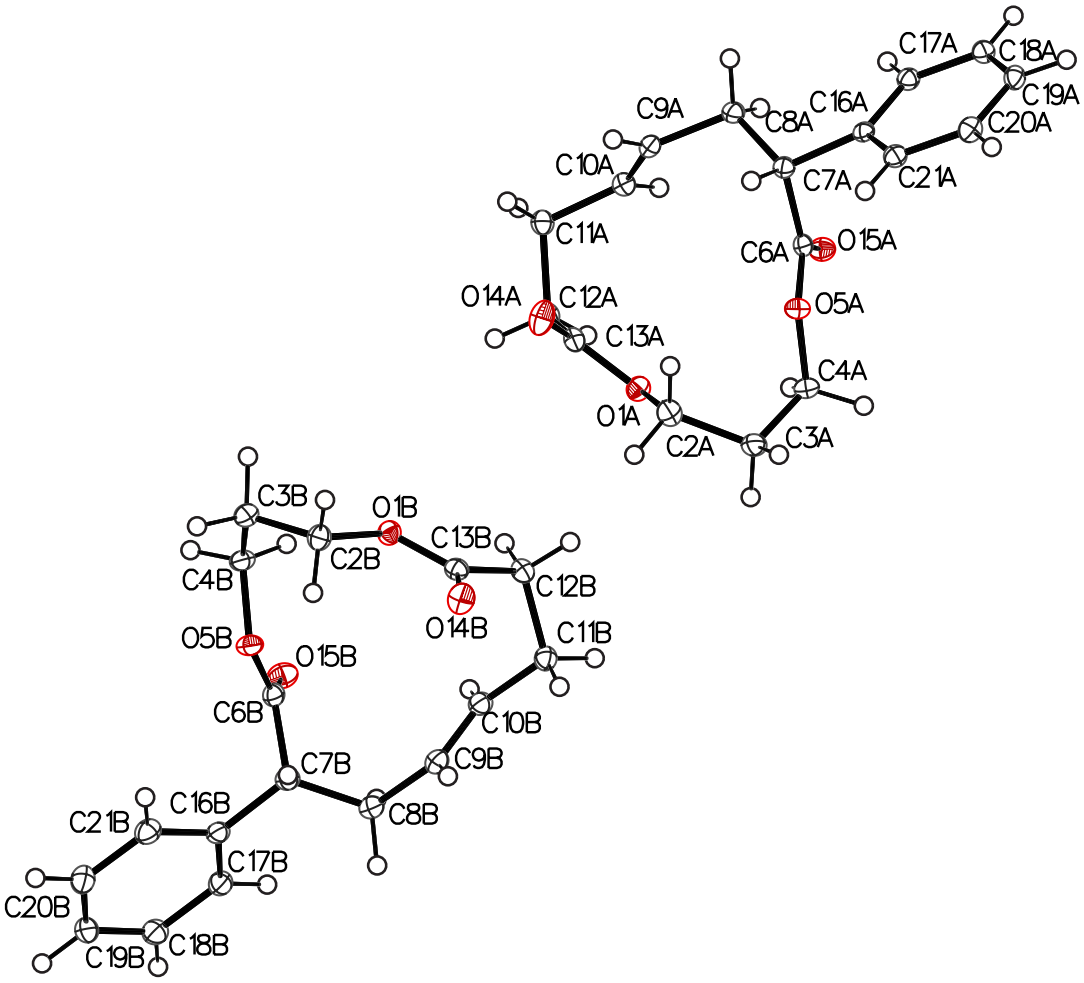

Fig. 1-30 A thermal ellipsoid plot of **rac-1-22** (spider-15025) at a 50% probability level. The full numbering scheme is shown. Hydrogen atoms are depicted as spheres.

Table 1-4. Crystal data and structure refinement for compound **1-22**.

Identification code	compound 4	
Empirical formula	$C_{17}H_{20}O_4$	
Formula weight	288.33	
Temperature	93(2) K	
Wavelength	1.54187 Å	
Crystal system	Triclinic	
Space group	$P\bar{1}$	
Unit cell dimensions	a = 5.51640(10) Å	α = 94.989(7)°
	b = 11.8803(3) Å	β = 90.739(6)°
	c = 23.3669(16) Å	g = 98.520(7)°
Volume	1508.23(12) $Å^3$	
Z	4	
Density (calculated)	1.270 Mg/m^3	
Absorption coefficient	0.731 mm^{-1}	
F(000)	616	
Crystal color	Colorless	
Crystal size	0.200 x 0.200 x 0.050 mm^3	
Θ range for data collection	1.899 to 68.240°	
Index ranges	$-6 \leq h \leq 6, -14 \leq k \leq 14, -28 \leq l \leq 28$	
Reflections collected	54047	
Independent reflections	5407 [R(int) = 0.0459]	
Completeness to θ = 67.687°	98.3 %	
Absorption correction	Semi-empirical from equivalents	
Max. and min. transmission	0.964 and 0.802	
Refinement method	Full-matrix least-squares on F^2	
Data / restraints / parameters	5407 / 0 / 379	
Goodness-of-fit on F^2	1.054	
Final R indices [I>2σ(I) = 4987 data]	R1 = 0.0391, wR2 = 0.0948	
R indices (all data)	R1 = 0.0421, wR2 = 0.0973	
Largest diff. peak and hole	0.446 and -0.216 $e.Å^{-3}$	

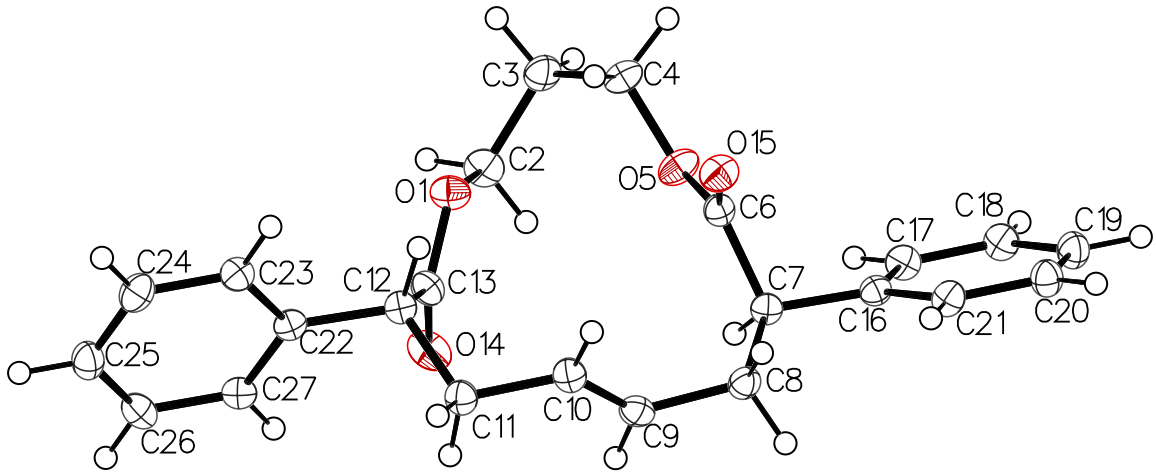

Figure 1-31. A thermal ellipsoid plot of **1-25** at a 50% probability level. The full numbering scheme is shown. Hydrogen atoms are depicted as spheres.

Table 1-5. Crystal data and structure refinement for compound **1-25**.

Identification code	compound 6	
Empirical formula	$C_{23}H_{24}O_4$	
Formula weight	364.42	
Temperature	150(2) K	
Wavelength	0.71075 Å	
Crystal system	Triclinic	
Space group	$P\bar{1}$	
Unit cell dimensions	a = 5.5848(4) Å	α = 69.615(5)°.
	b = 11.7915(8) Å	β = 84.229(6)°.
	c = 15.6064(11) Å	g = 81.837(6)°.
Volume	952.16(12) $Å^3$	
Z	2	
Density (calculated)	1.271 Mg/m^3	
Absorption coefficient	0.086 mm^{-1}	
F(000)	388	
Crystal color	Colorless	
Crystal size	0.220 x 0.210 x 0.190 mm^3	
Theta range for data collection	3.494 to 27.468°	
Index ranges	$-7 \leq h \leq 7, -15 \leq k \leq 15, -20 \leq l \leq 20$	
Reflections collected	16756	
Independent reflections	4345 [R(int) = 0.0758]	
Completeness to theta = 25.242°	99.8 %	
Absorption correction	Semi-empirical from equivalents	
Max. and min. transmission	0.984 and 0.795	
Refinement method	Full-matrix least-squares on F^2	
Data / restraints / parameters	4345 / 0 / 245	
Goodness-of-fit on F^2	1.092	
Final R indices [I>2sigma(I) = 2226 data]	R1 = 0.0510, wR2 = 0.1119	
R indices (all data, ? Å)	R1 = 0.1232, wR2 = 0.1695	
Extinction coefficient	0.033(5)	
Largest diff. peak and hole	0.294 and -0.298 $e.Å^{-3}$	

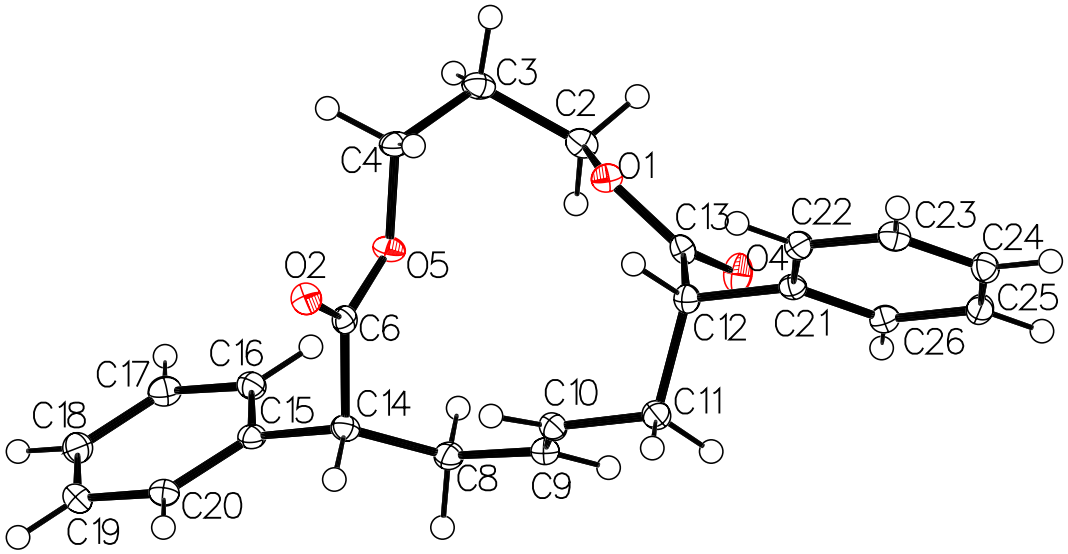

Figure 1-32. A thermal ellipsoid plot of **1-26** at a 50% probability level. The full numbering scheme is shown. Hydrogen atoms are depicted as spheres.

Table 1-6. Crystal data and structure refinement for compound **1-26**.

Identification code	compound 7	
Empirical formula	$C_{23}H_{24}O_4$	
Formula weight	364.42	
Temperature	93(2) K	
Wavelength	1.54187 Å	
Crystal system	Triclinic	
Space group	$P\bar{1}$	
Unit cell dimensions	a = 5.59160(10) Å	α = 70.326(5)°.
	b = 11.9281(2) Å	β = 80.097(6)°.
	c = 15.3677(11) Å	g = 79.031(6)°.
Volume	941.04(8) $Å^3$	
Z	2	
Density (calculated)	1.286 Mg/m^3	
Absorption coefficient	0.701 mm^{-1}	
F(000)	388	
Crystal color	Colorless	
Crystal size	0.270 x 0.140 x 0.050 mm^3	
Θ range for data collection	3.075 to 66.499°	
Index ranges	$-6 \le h \le 6, -14 \le k \le 14, -18 \le l \le 18$	
Reflections collected	28626	
Independent reflections	3254 [R(int) = 0.0430]	
Completeness to θ = 66.499 °	97.8 %	
Absorption correction	Semi-empirical from equivalents	
Max. and min. transmission	0.966 and 0.850	
Refinement method	Full-matrix least-squares on F^2	
Data / restraints / parameters	3254 / 0 / 244	
Goodness-of-fit on F^2	1.073	
Final R indices [I>2σ(I) = 3006 data]	R1 = 0.0294, wR2 = 0.0735	
R indices (all data)	R1 = 0.0317, wR2 = 0.0749	
Largest diff. peak and hole	0.208 and -0.153 $e.Å^{-3}$	

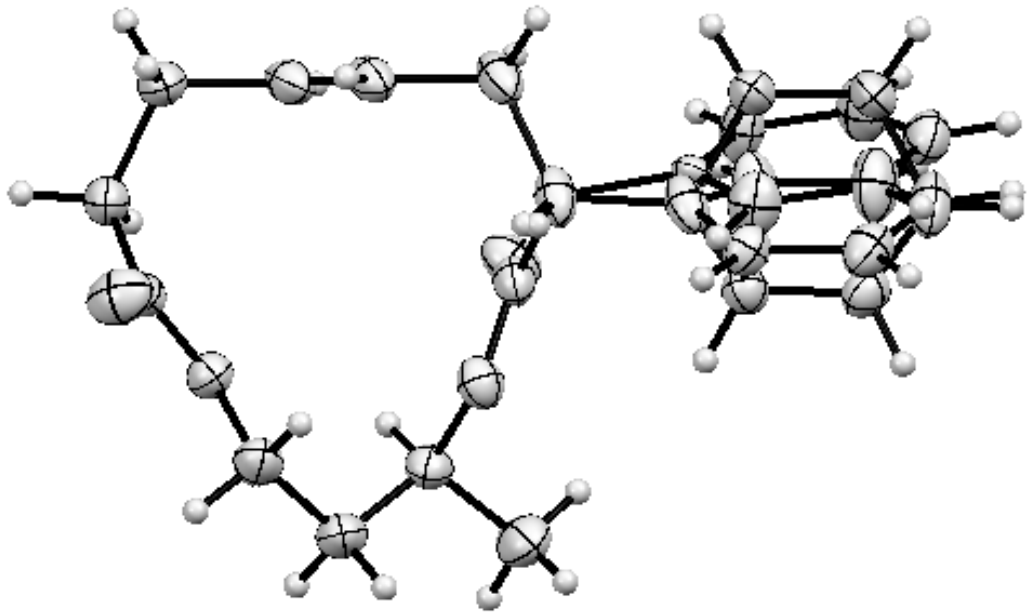

Figure 1-33. A thermal ellipsoid plot of **1-27** (spider_13084) at a 50% probability level. The hydrogen atoms are shown as spheres.

Table 1-7. Crystal data and structure refinement for compound **1-27** (spider_13084).

Identification code	spider_13084	
Empirical formula	$C_{18}H_{22}O_4$	
Formula weight	302.35	
Temperature	150(2) K	
Wavelength	0.71075 Å	
Crystal system	Orthorhombic	
Space group	*P b c a*	
Unit cell dimensions	a = 8.9681(3) Å	a = 90°
	b = 9.8245(3) Å	b = 90°
	c = 36.663(3) Å	g = 90°
Volume	3230.3(3) $Å^3$	
Z	8	
Density (calculated)	1.243 Mg/m^3	
Absorption coefficient	0.087 mm^{-1}	
F(000)	1296	
Crystal color	Colorless	
Crystal size	0.220 x 0.200 x 0.190 mm^3	
Θ range for data collection	3.125 to 27.483°	
Index ranges	$-11 \leq h \leq 11$, $-12 \leq k \leq 12$, $-47 \leq l \leq 47$	
Reflections collected	98785	
Independent reflections	3708 [R(int) = 0.0762]	
Completeness to θ = 25.242°	99.9 %	
Absorption correction	Semi-empirical from equivalents	
Max. and min. transmission	0.984 and 0.849	
Refinement method	Full-matrix least-squares on F^2	
Data / restraints / parameters	3708 / 0 / 290	
Goodness-of-fit on F^2	1.057	
Final R indices [$I>2\sigma(I)$ = 2883 data]	R1 = 0.0483, wR2 = 0.1037	
R indices (all data)	R1 = 0.0674, wR2 = 0.1120	
Largest diff. peak and hole	0.149 and -0.190 e.$Å^{-3}$	

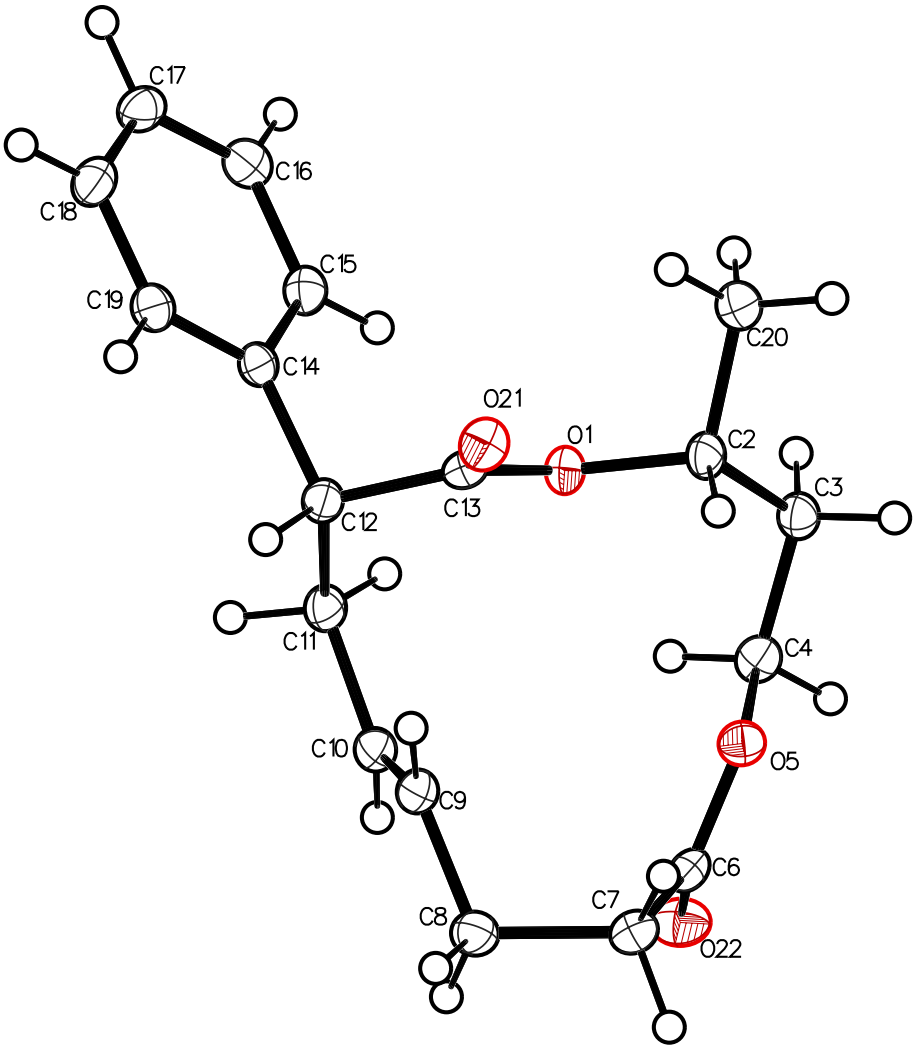

Figure 1-34. A thermal ellipsoid plot of **1-28** (007-15017) at a 50% probability level. The hydrogen atoms are shown as spheres. The chirality of atom C2 is R; C12 is R.

Table 1-8. Crystal data and structure refinement for **1-28** (007-15017).

Identification code	007-15017	
Empirical formula	$C_{18}H_{22}O_4$	
Formula weight	302.35	
Temperature	93(2) K	
Wavelength	1.54178 Å	
Crystal system	Monoclinic	
Space group	*C* 2/*c*	
Unit cell dimensions	a = 17.6902(12) Å	α = 90°.
	b = 5.6442(4) Å	β = 103.867(2)°.
	c = 32.347(2) Å	γ = 90°.
Volume	3135.6(4) $Å^3$	
Z	8	
Density (calculated)	1.281 Mg/m^3	
Absorption coefficient	0.727 mm^{-1}	
F(000)	1296	
Crystal size	0.200 x 0.200 x 0.090 mm^3	
Crystal color and habit	Colorless Prism	
Diffractometer	Rigaku Saturn 944+ CCD	
Θ range for data collection	2.814 to 67.878°.	
Index ranges	$-20 \leq h \leq 21$, $-6 \leq k \leq 6$, $-38 \leq l \leq 38$	
Reflections collected	47305	
Independent reflections	2825 [R(int) = 0.0476]	
Observed reflections (I > 2σ(I))	2574	
Completeness to θ = 67.679°	99.7 %	
Absorption correction	Semi-empirical from equivalents	
Max. and min. transmission	0.937 and 0.768	
Solution method	SHELXT-2014/5 (Sheldrick, 2014)	
Refinement method	SHELXL-2014/7 (Sheldrick, 2014)	
Data / restraints / parameters	2825 / 0 / 200	
Goodness-of-fit on F^2	1.052	
Final R indices [I>2σ(I)]	R1 = 0.0282, wR2 = 0.0690	
R indices (all data)	R1 = 0.0318, wR2 = 0.0707	
Largest diff. peak and hole	0.192 and -0.197 $e.Å^{-3}$	

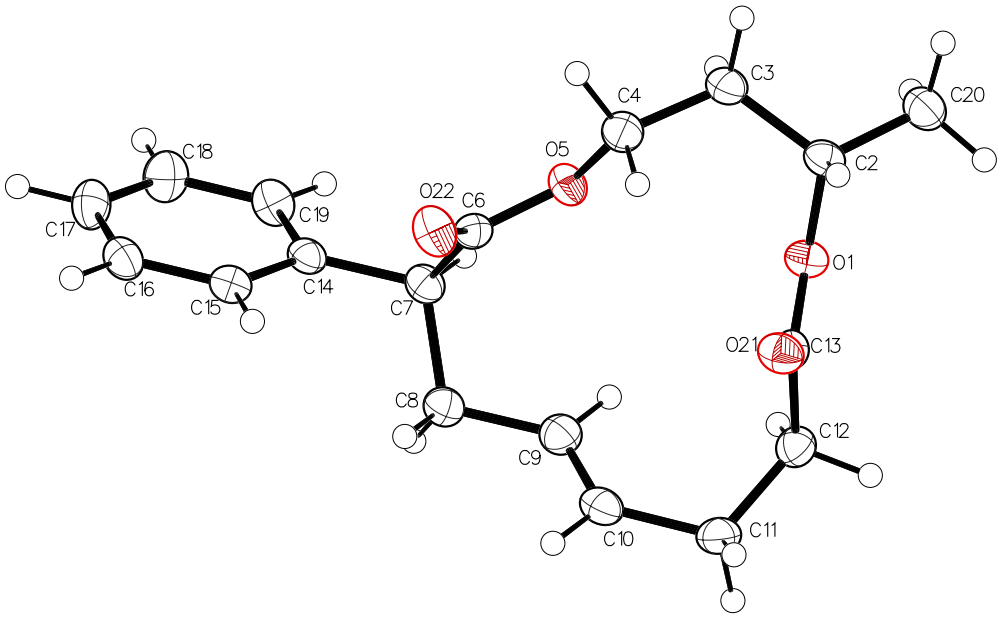

Figure 1-35. Thermal ellipsoid plot and the full numbering scheme of **1-29** (007-15060). All atoms shown are depicted with 50% thermal contours. The hydrogen atoms are shown as spheres. The chirality of atom C2 is S; C12 is S.

Table 1-9. Crystal data and structure refinement for **1-29** (007-15060).

Identification code	007-15060	
Empirical formula	$C_{18}H_{22}O_4$	
Formula weight	302.35	
Temperature	93(2) K	
Wavelength	1.54178 Å	
Crystal system	Monoclinic	
Space group	P 2_1/c	
Unit cell dimensions	a = 12.8744(9) Å	α = 90°.
	b = 13.5401(9) Å	β = 104.358(4)°.
	c = 9.4132(7) Å	γ = 90°.
Volume	1589.7(2) $Å^3$	
Z	4	
Density (calculated)	1.263 Mg/m^3	
Absorption coefficient	0.717 mm^{-1}	
F(000)	648	
Crystal size	0.200 x 0.200 x 0.090 mm^3	
Crystal color and habit	Colorless Prism	
Diffractometer	Rigaku Saturn 944+ CCD	
Θ range for data collection	3.544 to 66.580°.	
Index ranges	$-15 \leq h \leq 15$, $-15 \leq k \leq 15$, $-11 \leq l \leq 11$	
Reflections collected	49323	
Independent reflections	2784 [R(int) = 0.0879]	
Observed reflections (I > 2σ(I))	2355	
Completeness to θ = 66.580°	98.9 %	
Absorption correction	Semi-empirical from equivalents	
Max. and min. transmission	0.938 and 0.684	
Solution method	SHELXT-2014/5 (Sheldrick, 2014)	
Refinement method	SHELXL-2014/7 (Sheldrick, 2014)	
Data / restraints / parameters	2784 / 0 / 200	
Goodness-of-fit on F^2	1.049	
Final R indices [I>2σ(I)]	R1 = 0.0356, wR2 = 0.0934	
R indices (all data)	R1 = 0.0440, wR2 = 0.1008	
Largest diff. peak and hole	0.230 and -0.266 $e.Å^{-3}$	

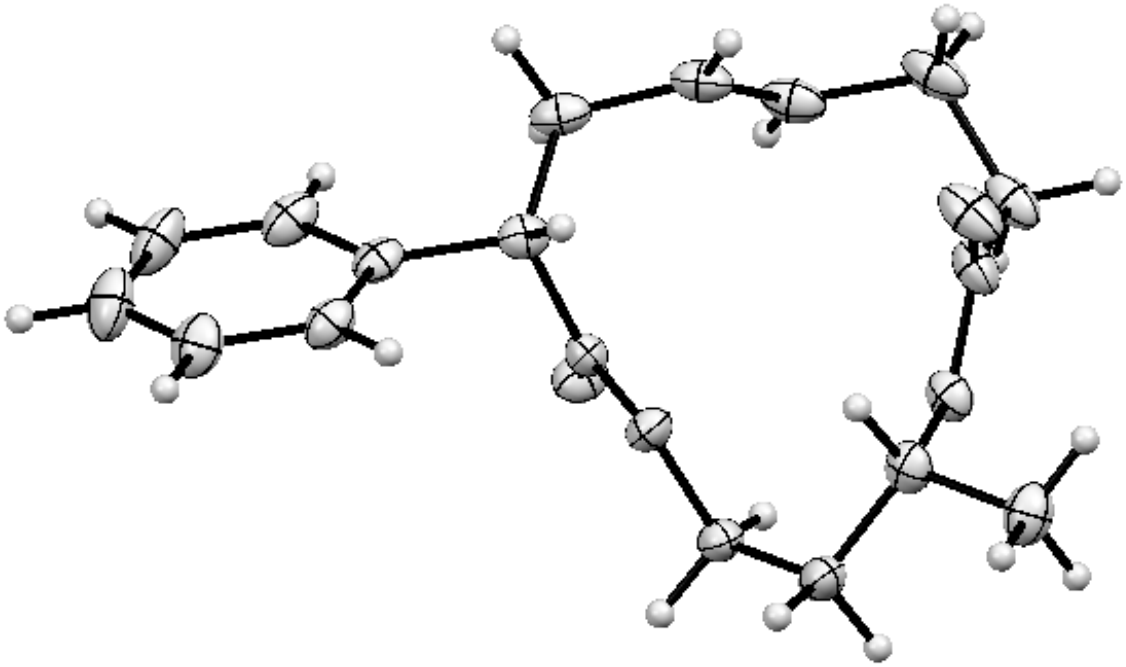

Figure 1-36. Thermal ellipsoid plot of **1-30** (007_13099). All atoms shown are depicted with 50% thermal contours. The hydrogen atoms are shown as spheres.

Table 1-10. Crystal data and structure refinement for **1-30** (007_13099).

Identification code	007_13099	
Empirical formula	$C_{18}H_{22}O_4$	
Formula weight	302.35	
Temperature	93(2) K	
Wavelength	1.54178 Å	
Crystal system	Monoclinic	
Space group	$P\,2_1/c$	
Unit cell dimensions	a = 12.2539(10) Å	a = 90°
	b = 5.61320(10) Å	b = 103.473(8)°
	c = 23.7795(4) Å	g = 90°
Volume	1590.63(15) $Å^3$	
Z	4	
Density (calculated)	1.263 Mg/m^3	
Absorption coefficient	0.716 mm^{-1}	
F(000)	648	
Crystal color	Colorless	
Crystal size	0.220 x 0.110 x 0.090 mm^3	
Θ range for data collection	3.709 to 65.048°	
Index ranges	$-14 \le h \le 14$, $-6 \le k \le 6$, $-24 \le l \le 27$	
Reflections collected	24316	
Independent reflections	2673 [R(int) = 0.0447]	
Completeness to θ = 65.048°	98.2 %	
Absorption correction	Semi-empirical from equivalents	
Max. and min. transmission	0.938 and 0.818	
Refinement method	Full-matrix least-squares on F^2	
Data / restraints / parameters	2673 / 0 / 200	
Goodness-of-fit on F^2	1.027	
Final R indices [$I>2\sigma(I)$ = 2490 data]	R1 = 0.0316, wR2 = 0.0848	
R indices (all data)	R1 = 0.0344, wR2 = 0.0890	
Largest diff. peak and hole	0.200 and -0.173 $e.Å^{-3}$	

Computational details for energy minization experiments

Quantum chemical calculations were performed using Gaussian 09. Geometry optimization and vibrational frequency calculations in the gas phase were carried out at the M06-2x/6-31+g(d) level of theory. The M06-2x functional was selected over other popular density functionals due to its adequate description of noncovalent interactions in macrocycles. Stationary points were characterized by frequency calculations at 298 K, with structures at energy minima showing no negative frequencies and transition-states showing one negative frequency. All energy values are zero point corrected and shown are in kcal mol^{-1}, bond lengths are reported in Ångstroms (Å), and bond angles in degrees (˚). Molecular figures were generated using CYLView.

Computational experiments designed to determine the effect of the configuration at the stereogenic center to the preference for a specific planar chirality of monosubstituted [13]-mcrodilacone.

1.10 References

1. (a) Driggers, E. M.; Hale, S. P.; Lee, J.; Terrett, N. K., The exploration of macrocycles for drug discovery--an underexploited structural class. *Nat Rev Drug Discov* **2008,** *7* (7), 608-24; (b) Marsault, E.; Peterson, M. L., Macrocycles are great cycles: applications, opportunities, and challenges of synthetic macrocycles in drug discovery. *J Med Chem* **2011,** *54* (7), 1961-2004; (c) Yudin, A. K., Macrocycles: lessons from the distant past, recent developments, and future directions. *Chemical Science* **2015,** *6* (1), 30-49; (d) Mallinson, J.; Collins, I., Macrocycles in new drug discovery. *Future Med Chem* **2012,** *4* (11), 1409-38; (e) Giordanetto, F.; Kihlberg, J., Macrocyclic drugs and clinical candidates: what can medicinal chemists learn from their properties? *J Med Chem* **2014,** *57* (2), 278-95.

2. Haubner, R.; Schmitt, W.; Hölzemann, G.; Goodman, S. L.; Jonczyk, A.; Kessler, H., Cyclic RGD Peptides Containing β-Turn Mimetics. *Journal of the American Chemical Society* **1996,** *118* (34), 7881-7891.

3. DeLorbe, J. E.; Clements, J. H.; Whiddon, B. B.; Martin, S. F., Thermodynamic and Structural Effects of Macrocyclic Constraints in Protein−Ligand Interactions. *ACS Medicinal Chemistry Letters* **2010,** *1* (8), 448-452.

4. Dinsmore, C. J.; Bogusky, M. J.; Culberson, J. C.; Bergman, J. M.; Homnick, C. F.; Zartman, C. B.; Mosser, S. D.; Schaber, M. D.; Robinson, R. G.; Koblan, K. S.; Huber, H. E.; Graham, S. L.; Hartman, G. D.; Huff, J. R.; Williams, T. M., Conformational Restriction of Flexible Ligands Guided by the Transferred NOE Experiment: Potent

Macrocyclic Inhibitors of Farnesyltransferase. *Journal of the American Chemical Society* **2001,** *123* (9), 2107-2108.

5. Jirousek, M. R.; Gillig, J. R.; Gonzalez, C. M.; Heath, W. F.; McDonald, J. H.; Neel, D. A.; Rito, C. J.; Singh, U.; Stramm, L. E.; Melikian-Badalian, A.; Baevsky, M.; Ballas, L. M.; Hall, S. E.; Winneroski, L. L.; Faul, M. M., (S)-13-[(Dimethylamino)methyl]-10,11,14,15-tetrahydro-4,9:16,21-dimetheno- 1H,13H-dibenzo[e,k]pyrrolo[3,4-h][1,4,13]oxadiazacyclohexadecene-1,3(2H)-dione (LY333531) and Related Analogues: Isozyme Selective Inhibitors of Protein Kinase Cβ. *Journal of Medicinal Chemistry* **1996,** *39* (14), 2664-2671.

6. Bartlett, S.; Beddard, G. S.; Jackson, R. M.; Kayser, V.; Kilner, C.; Leach, A.; Nelson, A.; Oledzki, P. R.; Parker, P.; Reid, G. D.; Warriner, S. L., Comparison of the ATP Binding Sites of Protein Kinases Using Conformationally Diverse Bisindolylmaleimides. *Journal of the American Chemical Society* **2005,** *127* (33), 11699-11708.

7. Rezai, T.; Yu, B.; Millhauser, G. L.; Jacobson, M. P.; Lokey, R. S., Testing the Conformational Hypothesis of Passive Membrane Permeability Using Synthetic Cyclic Peptide Diastereomers. *Journal of the American Chemical Society* **2006,** *128* (8), 2510-2511.

8. Hu, X.; Nguyen, K. T.; Jiang, V. C.; Lofland, D.; Moser, H. E.; Pei, D., Macrocyclic Inhibitors for Peptide Deformylase: A Structure−Activity Relationship Study of the Ring Size. *Journal of Medicinal Chemistry* **2004,** *47* (20), 4941-4949.

9. (a) Lipinski, C. A.; Lombardo, F.; Dominy, B. W.; Feeney, P. J., Experimental and computational approaches to estimate solubility and permeability in drug

discovery and development settings1. *Advanced Drug Delivery Reviews* **2001,** *46* (1–3), 3-26; (b) Veber, D. F.; Johnson, S. R.; Cheng, H.-Y.; Smith, B. R.; Ward, K. W.; Kopple, K. D., Molecular Properties That Influence the Oral Bioavailability of Drug Candidates. *Journal of Medicinal Chemistry* **2002,** *45* (12), 2615-2623.

10. Ganesan, A., The impact of natural products upon modern drug discovery. *Current Opinion in Chemical Biology* **2008,** *12* (3), 306-317.

11. Villar, E. A.; Beglov, D.; Chennamadhavuni, S.; Porco Jr, J. A.; Kozakov, D.; Vajda, S.; Whitty, A., How proteins bind macrocycles. *Nat Chem Biol* **2014,** *10* (9), 723-731.

12. Wells, J. A.; McClendon, C. L., Reaching for high-hanging fruit in drug discovery at protein-protein interfaces. *Nature* **2007,** *450* (7172), 1001-1009.

13. Mani, S.; Ghalib, M.; Goel, S.; Serradell, N.; Bolós, J.; Rosa, E., Ixabepilone. *Drugs of the Future* **2007,** *32* (12), 1033.

14. Dabydeen, D. A.; Burnett, J. C.; Bai, R.; Verdier-Pinard, P.; Hickford, S. J. H.; Pettit, G. R.; Blunt, J. W.; Munro, M. H. G.; Gussio, R.; Hamel, E., Comparison of the Activities of the Truncated Halichondrin B Analog NSC 707389 (E7389) with Those of the Parent Compound and a Proposed Binding Site on Tubulin. *Molecular Pharmacology* **2006,** *70* (6), 1866-1875.

15. Schlunzen, F.; Zarivach, R.; Harms, J.; Bashan, A.; Tocilj, A.; Albrecht, R.; Yonath, A.; Franceschi, F., Structural basis for the interaction of antibiotics with the peptidyl transferase centre in eubacteria. *Nature* **2001,** *413* (6858), 814-821.

16. Zapf, C. W.; Bloom, J. D.; Li, Z.; Dushin, R. G.; Nittoli, T.; Otteng, M.; Nikitenko, A.; Golas, J. M.; Liu, H.; Lucas, J.; Boschelli, F.; Vogan, E.; Olland, A.; Johnson, M.; Levin,

J. I., Discovery of a stable macrocyclic o-aminobenzamide Hsp90 inhibitor which significantly decreases tumor volume in a mouse xenograft model. *Bioorganic & Medicinal Chemistry Letters* **2011,** *21* (15), 4602-4607.

17. Still, W. C.; Galynker, I., Chemical consequences of conformation in macrocyclic compounds : An effective approach to remote asymmetric induction1. *Tetrahedron* **1981,** *37* (23), 3981-3996.

18. Kim, H.; Lee, H.; Kim, J.; Kim, S.; Kim, D., A General Strategy for Synthesis of Both (6Z)- and (6E)-Cladiellin Diterpenes: Total Syntheses of (−)-Cladiella-6,11-dien-3-ol, (+)-Polyanthellin A, (−)-Cladiell-11-ene-3,6,7-triol, and (−)-Deacetoxyalcyonin Acetate. *Journal of the American Chemical Society* **2006,** *128* (49), 15851-15855.

19. Tu, W.; Floreancig, P. E., Oxidative Carbocation Formation in Macrocycles: Synthesis of the Neopeltolide Macrocycle. *Angewandte Chemie International Edition* **2009,** *48* (25), 4567-4571.

20. Seiple, I. B.; Su, S.; Young, I. S.; Lewis, C. A.; Yamaguchi, J.; Baran, P. S., Total Synthesis of Palau'amine. *Angewandte Chemie International Edition* **2010,** *49* (6), 1095-1098.

21. Han, C.; Rangarajan, S.; Voukides, A. C.; Beeler, A. B.; Johnson, R.; Porco, J. A., Reaction Discovery Employing Macrocycles: Transannular Cyclizations of Macrocyclic Bis-lactams. *Organic Letters* **2009,** *11* (2), 413-416.

22. Warrington, J. M.; Yap, G. P. A.; Barriault, L., Tandem Oxy-Cope/Transannular Ene Reaction of 1,2-Divinylcyclohexanols. *Organic Letters* **2000,** *2* (5), 663-665.

23. Wessjohann, L.; Ruijter, E.; Garcia-Rivera, D.; Brandt, W., What can a chemist learn from nature's macrocycles? – A brief, conceptual view. *Mol Divers* **2005,** *9* (1-3), 171-186.

24. Dale, J., Conformational Aspects of Many-Membered Rings. *Angewandte Chemie International Edition in English* **1966,** *5* (12), 1000-1021.

25. Groth, P., <50 Crystal Structure of Cyclotetradecane at -157 degrees C..pdf>. *Acta Chem. Scand. A 30* (2), 155-156.

26. Drotloff, H.; Rotter, H.; Emeis, D.; Moeller, M., Mesomorphic state of cyclotetradecane. *Journal of the American Chemical Society* **1987,** *109* (25), 7797-7803.

27. Anet, F. A. L.; Cheng, A. K., Conformation of cyclohexadecane. *Journal of the American Chemical Society* **1975,** *97* (9), 2420-2424.

28. Shannon, V. L.; Strauss, H. L.; Snyder, R. G.; Elliger, C. A.; Mattice, W. L., Conformation of the cycloalkanes C14H28, C16H32, and C22H44 in the liquid and high-temperature crystalline phases by vibrational spectroscopy. *Journal of the American Chemical Society* **1989,** *111* (6), 1947-1958.

29. Clyne, D. S.; Weiler, L., The Conformational Analysis of 14-Membered Macrocyclic Ethers. *Tetrahedron* **2000,** *56* (10), 1281-1297.

30. Bassi, I. W.; Scordamaglia, R.; Fiore, L., X-Ray crystal structure of 1,3,8,10-tetraoxacyclotetradecane. *Journal of the Chemical Society, Perkin Transactions 2* **1972,** (12), 1726-1729.

31. Dunitz, J. D.; Meyer, E. F., Die Strukturen der mittleren Ringverbindungen. IX. 1, 8-Diazacyclotetradecan-dihydrobromid. *Helvetica Chimica Acta* **1965,** *48* (7), 1441-1449.

32. Anet, F. A. L.; Cheng, A. K.; Krane, J., Conformations and energy barriers in medium-and large-ring ketones. Evidence from carbon-13 and proton nuclear magnetic resonance. *Journal of the American Chemical Society* **1973,** *95* (23), 7877-7878.

33. Borgen, G. D., Johannes, <38 Conformational Studies of Macrocyclic Tetrakis(gem-dimethyl)cycloalkanediones..pdf>. *Acta Chemica Scandinavica* **1972,** *26* (5), 1799 -1804.

34. Keller, T. H.; Neeland, E. G.; Rettig, S.; Trotter, J.; Weiler, L., Conformational analysis of 14-membered macrolides using x-ray crystallography and molecular mechanics calculations. *Journal of the American Chemical Society* **1988,** *110* (23), 7858-7868.

35. (a) Dugat, D.; Valade, A.-G.; Combourieu, B.; Guyot, J., Conformational analysis of new 14-membered ring diketal dilactam macrocycles: molecular mechanics, liquid and solid state NMR studies. *Tetrahedron* **2005,** *61* (23), 5641-5653; (b) Borgen, G. D., Johannes; Gundersen, Lise-Lotte; Krivokapic, Alexander; Rise, Frode; Øverås, Anniken T., <43 Conformations of 11- and 14-Membered Ring Monolactams..pdf>. *Acta Chemica Scandinavica* **1998,** *52*, 1110-1115.

36. Glenn, M. P.; Kelso, M. J.; Tyndall, J. D. A.; Fairlie, D. P., Conformationally Homogeneous Cyclic Tetrapeptides: Useful New Three-Dimensional Scaffolds. *Journal of the American Chemical Society* **2003,** *125* (3), 640-641.

37. Montero, A.; Beierle, J. M.; Olsen, C. A.; Ghadiri, M. R., Design, Synthesis, Biological Evaluation, and Structural Characterization of Potent Histone Deacetylase Inhibitors Based on Cyclic α/β-Tetrapeptide Architectures. *Journal of the American Chemical Society* **2009,** *131* (8), 3033-3041.

38. Bisek, N.; Wetzel, S.; Arndt, H.-D.; Waldmann, H., Synthesis and Conformational Analysis of Stevastelin C3 Analogues and Their Activity Against the Dual-Specific Vaccina H1-Related Phosphatase. *Chemistry – A European Journal* **2008,** *14* (29), 8847-8860.

39. Jogalekar, A. S., Conformations of stevastelin C3 analogs: Computational deconvolution of NMR data reveals conformational heterogeneity and novel motifs. *Biopolymers* **2010,** *93* (11), 968-976.

40. (a) Fyvie, W. S.; Peczuh, M. W., Diastereoselectivity in Epoxidation of Carbohydrate Fused [13]-Macro-dilactones. *The Journal of Organic Chemistry* **2008,** *73* (9), 3626-3629; (b) Fyvie, W. S.; Peczuh, M. W., Remote induction of asymmetry in [13]-macro-dilactone topology by a single stereogenic center. *Chemical Communications* **2008,** (34), 4028-4030; (c) Ma, J.; Peczuh, M. W., Positioning and Configuration of Key Atoms Influence the Topology of [13]-Macrodiolides. *The Journal of Organic Chemistry* **2013,** *78* (15), 7414-7422; (d) Magpusao, A. N.; Rutledge, K.; Mercado, B. Q.; Peczuh, M. W., Stereogenic [small alpha]-carbons determine the shape and topology of [13]-macrodilactones. *Organic & Biomolecular Chemistry* **2015,** *13* (18), 5086-5089.

41. Nishio, S.; Somete, T.; Sugie, A.; Kobayashi, T.; Yaita, T.; Mori, A., Axially Chiral Macrocyclic E-Alkene Bearing Bisazole Component Formed by Sequential C–H

Homocoupling and Ring-Closing Metathesis. *Organic Letters* **2012,** *14* (10), 2476-2479.

42. Yoshioka, S.; Inokuma, Y.; Hoshino, M.; Sato, T.; Fujita, M., Absolute Structure Determination of Compounds with Axial and Planar Chirality Using the Crystalline Sponge Method. *Chemical Science* **2015**.

43. Akhigbe, J.; Luciano, M.; Zeller, M.; Brückner, C., Mono- and Bisquinoline-Annulated Porphyrins from Porphyrin β,β′-Dione Oximes. *The Journal of Organic Chemistry* **2015,** *80* (1), 499-511.

Chapter 2

A cardiac glycoside activities link Na^+/K^+ ATPase ion-transport to breast cancer migration via correlative SAR

2.1 Introduction to cell migration

In its simplest definition, cell migration refers to the translation of the whole cell body from one location to another[1]. It is a highly complex and dynamic process that is tightly regulated and coordinated spatially and temporally. In general, migration begins when a cell responds to an external signal to migrate through polarization or formation of distinct front and rear part. The front part forms a protrusion in the direction of migration, which is then attached to the substratum by adhesion molecules. At the leading edge of this protrusion, actin polymerization generates contraction forces, which move the cell forward. At the rear, actin depolymerization retracts the cell and adhesion molecules detach the rear portion from the substratum. The specific details (mechanics, mechanisms and regulation) of each of these processes comprise a huge current research field.

Cell migration is a fundamental cellular process that is critical for a number of physiological and pathological phenomena such as wound healing[2], tissue remodeling, angiogenesis, and cancer metastasis[3]. Because of the highly complex nature of the choreography, mechanics and regulation of cell migration, no complete model that incorporates all of its components currently exists. One of the major problems in determining the precise roles of each of the proteins involved in cell migration is the lack of potent and selective inhibitors for the functions of these proteins. Besides their therapeutic potential, small-molecule inhibitors of cell migration serve as valuable tools to probe the molecular basis of cell motility[4].

2.2. Small molecule inhibitors of cell migration

Most of the reported small molecule inhibitors of cell migration (Fig. 2-1) target the two major parts of cell migration machinery, the microtubule and actin. Some of the small molecules that inhibit cell migration by affecting the microtubule include colchicine, which inhibits tubulin polymerization and destabilizes the microtubule[5] and taxol, which, in contrast to colchicine, is a microtubule-stabilizing agent[6]. Those that modulate actin functions can be superficially classified as (1) actin-filament destabilizers (2) actin filament-stabilizers and (3) inhibitors of actin-binding and actin-regulatory proteins[4]. Examples of actin-filament destabilizers include cytochalasin B, cytochalasin D and latrunculin A. Cytochalsin is the most highly characterized microtubule destabilizer which acts by binding and blocking the end of actin filaments and thus inhibiting dynamics at this end of the filament[7]. Among actin filament-stabilizer, the most popular is phalloidin, a phallotoxin from a poisonous mushroom. Phalloidin, although not cell penetrable, is a very useful probe molecule commonly conjugated to a fluorophore and used for visualizing F-actin[7]. Jasplakinolide, on the other hand, is a cell-permeable actin-stabilizer[8].

In contrast to the vast number of small molecules that affect cell migration by modulating the activities of actin and microtubules, there are only very few that targets actin-binding proteins and actin-regulatory proteins and thus new small molecules that target these proteins will be valuable for understanding the regulatory mechanism of actin dynamics. Some examples include blebistatin (an inhibitor of class II-skeletal muscle myosin)[9], synthetic naphthalenesulfonamide, ML-9 (inhibitor of myosin light chain

kinase)[10] and synthetic pyridine derivative Y-27632, an inhibitor of Rho-associated kinase[11].

There are also a few cell migration inhibitors whose target is unknown. One example is the 15-membered macrocyclic natural product Motuporamine C extracted from a marine sponge *Xestospongia exigua*[12]. It was found to inhibit tumor cell invasion and angiogenesis[13]. Finding the biomolecular target of cell migration inhibitors could contribute to the complete understanding of cell migration. The small molecules previously discussed exemplify mechanisms of actions that have already been identified. With the advances in screening technologies as well as small molecule library generation, more useful probes are expected to be discovered and will continue to push the boundary of knowledge in the field of cell migration. Please refer to an excellent review article[4] for a more thorough discussion of cell migration inhibitors.

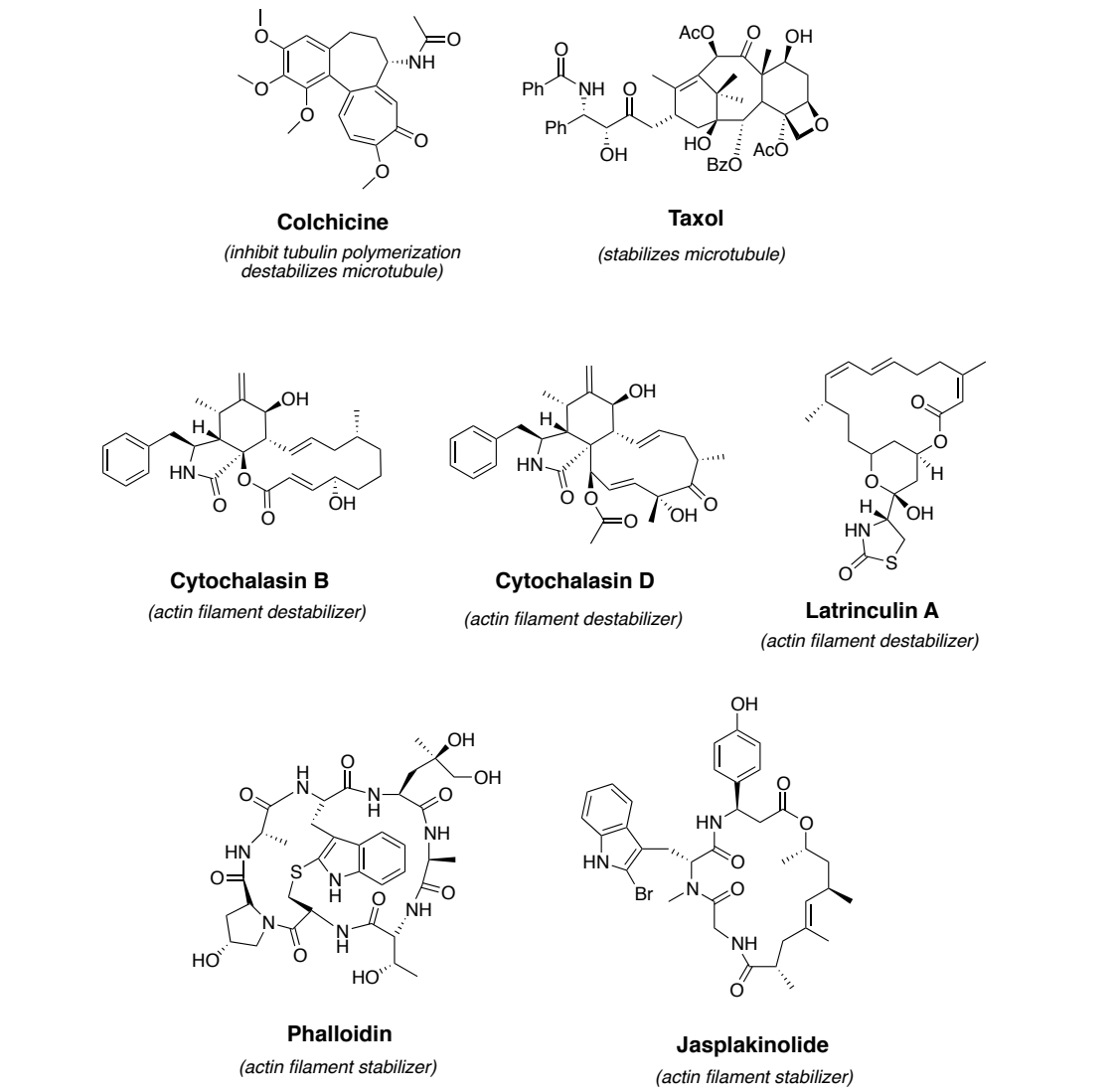

Fig. 2-1. Representative small molecule inhibitors of cell migration.

2.3 Chemical genetics screening for cell sheet migration using a HTS scratch-wound assay

Collective cell migration, although less studied than individual cell migration, is the mode of migration that is operative in physiological processes such as wound healing, gastrulation, tissue repair and cancer metastasis[14]. Single cells must abandon their individual migratory behavior and coordinate their cytoskeletal activities with adjacent cells across cell-cell junctions in order to migrate collectively as a cell sheet. Assays that can recapitulate this mode of migration constitute valuable methods for understanding the fundamental mechanisms and mechanics of collective cell migration.

Cultured epithelial cells provide a great model system for understanding collective cell migration as well as interactions of cells in a sheet. Scratching the monolayer of epithelial cells creates a gap or 'wound' that can initiate the migration of cells towards the wound; this is the process of wound closure (Fig. 2-2). Movement of the cell sheet during wound closure in cultured epithelial cells is very similar to cell sheet movement in vivo during the re-epithelialization step of wound healing and during embryonic morphogenesis of various organisms[15]. Madin-Darby canine kidney (MDCK) cells are one of the widely used cell line for investigating collective cell migration using the wound-closure or scratch-wound assay. MDCK cells move as a cohesive and coherent sheet of cells without loss of cell-cell contact with multiple rows of cells actively contributing to cell sheet movement through protrusive cell crawling[16].

The Fenteany lab adapted the MDCK cell scratch-wound assay to a high-throughput format and used this for chemical genetic screening of epithelial cell sheet migration inhibitors[17]. The 'quantitative' version of scratch-wound assay begins with

addition of either a test compound or a DMSO control in a confluent monolayer of MDCK cells. Mechanical wounding of the monolayer (using a pipette tip) introduces a circular wound, which triggers the collective cell migration of the epithelial sheet (Fig. 2-2). The rate of collective cell sheet migration is measured by quantifying the progress of wound-closure, which in turn is monitored by taking pictures of each well at different time points. The remaining open area at each time-point is calculated by tracing the wound margin in each image using the ImageJ software. For high-throughput screening, an 'end-point' version of the scratch-wound assay is done. In this version, the test compounds are only assayed at one concentration and the compound is considered active if the wound area is still open at a time point when the DMSO-treated well is already closed. To verify and carefully characterize the antimigratory activity of the active compounds, the previously described quantitative wound-closure assay is used where multiple concentrations of active compounds are assayed to generate a dose-response curve, % inhibition and IC_{50} values.

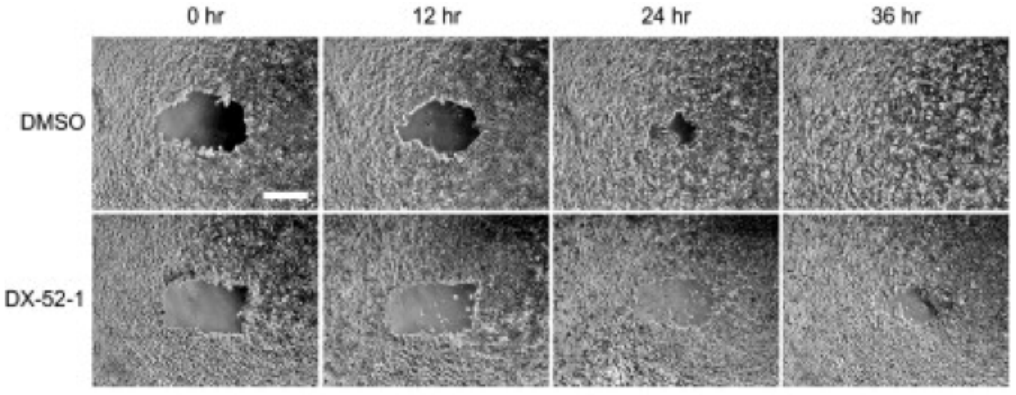

Fig. 2-2. Scratch-wound assay of DX-52-1. The figure was re-used with permission.

Using this strategy, the Fenteany lab discovered new small molecule inhibitors of epithelial cell sheet migration with new protein targets and mechanisms of actions. Some of the small molecules discovered using this strategy include the small molecule DX-52 and locostatin (Fig. 2-3). DX-52 is an analog of the natural product quinocarmycin that targets radixin and inhibited the epithelial cell sheet migration by disrupting the interaction of radixin and actin[16]. This small molecule helped clarify the role of radixin in epithelial cell sheet migration where G protein-coupled receptor kinase 2 (GRK2) was found to activate radixin leading to the regulation of membrane protrusion in migrating epithelial cells[18]. Locostatin on the other hand, targets RKIP and inhibited the cell migration by disrupting the RKIP-Raf 1 interaction[19]. Locostatin has been a valuable probe molecule in understanding the role of RKIP in epithelial and cancer cell migration, invasion and metastasis[20].

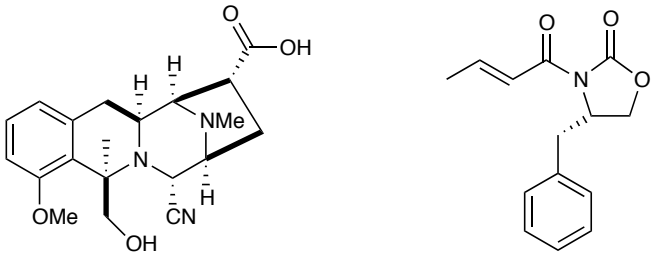

DX-52-1
IC_{50} = 140 nM

locostatin
IC_{50} = 17 μM

Fig. 2-3. Representative epithelial cell sheet migration small molecule probe discovered through high throughput scratch-wound assay in MDCK cells.

2.4 Chemical genetics screening for breast cancer cell migration

The same high-throughput scratch-wound assay was adapted to a 96-well plate format to screen compound libraries for inhibitors of triple-negative breast cancer cell migration. Triple negative cells are a type of breast cancer that is refractory to current chemotherapeutic options. Instead of MDCK cells, immortalized triple negative breast cancer cell lines (BT20 and MDA-MB-231) were used to screen three compound libraries. The first library screened was a small collection of [13]-macrodilactones and carbohydrate-fused [13]-macrodilcatones synthesized in the Peczuh Lab. The next compound libraries screened were commercial chemical libraries of natural product (880 compounds) and synthetic small molecules (12,720 compounds) from the companies Analyticon and Chembridge respectively. The screening strategy starts at 50 μM concentration. Active compounds at this concentration are then cherry-picked and rescreened at lower concentrations (Table 2-1). New small molecule probes for cell migration were discovered from this screening effort, which could potentially be followed up for further SAR, target ID and mechanism of action studies. The next paragraphs will briefly describe the results of these screening efforts. The full list and structure of small molecule 'hits' from the Analyticon natural product library can be found in the Appendix.

Table 2-1. Screening of three compound libraries for MDA-MB-231 breast cancer cell migration inhibitors

Concen-tration	PZ library (9 compounds)	Natural product (880 compounds)		Synthetic small molecules (12,720 compounds)	
50 μM	(3)	(55)	6 %	1,232	10 %
10 μM		(13)	1.5 %	43	0.4 %
2 μM		(10)	1.1 %	28	0.2 %
400 nM		(6)	0.7 %	19	0.1 %
80 nM		(6)	0.7 %	0	0 %

2.4.1 Results and discussion for screening of [13]-macrodilactone library

The triple negative breast cancer cell line BT20 was used to screen the small macrocyle library from the Peczuh Lab. In this effort, an octylglucoside-fused [13]-macrodilactones **2-1, 2-2** and **2-3** (Fig. 2-4) were found to inhibit the migration of this cell line at 30-50 μM concentrations. An SAR study was done to further characterize their antimigratory activity. The full details of this project can be found in the published report[21]. This section of this thesis chapter will only summarize the important results and include one new interpretation for the SAR data in light of the new insights learned from the first chapter.

The active compounds **2-1, 2-2** and **2-3** (Table 2-2) discovered from the initial qualitative scratch-wound assay were eventually found to have a low therapeutic index. Therapeutic index is the ratio of MLC (maximum lethal concentration) to MIC (minimum inhibitory concentration) when assayed using the quantitative scratch-wound assay and thus prevented the determination of IC_{50} values. We hypothesized that the low therapeutic index is due to the cytostatic or cytotoxic activities of these compounds. To test this hypothesis, the compounds were evaluated in a cell viability assay using the cell-counting kit 8 (CCK8) – a highly water soluble tetrazolium salt. The intermediate

molecules (synthetic precursors) **2-5, 2-6** and **2-7** during the synthesis of the octylglucoside-fused [13]-macrodilactones were also evaluated for their antiproliferative and cytotoxic activities (Table 2-2).

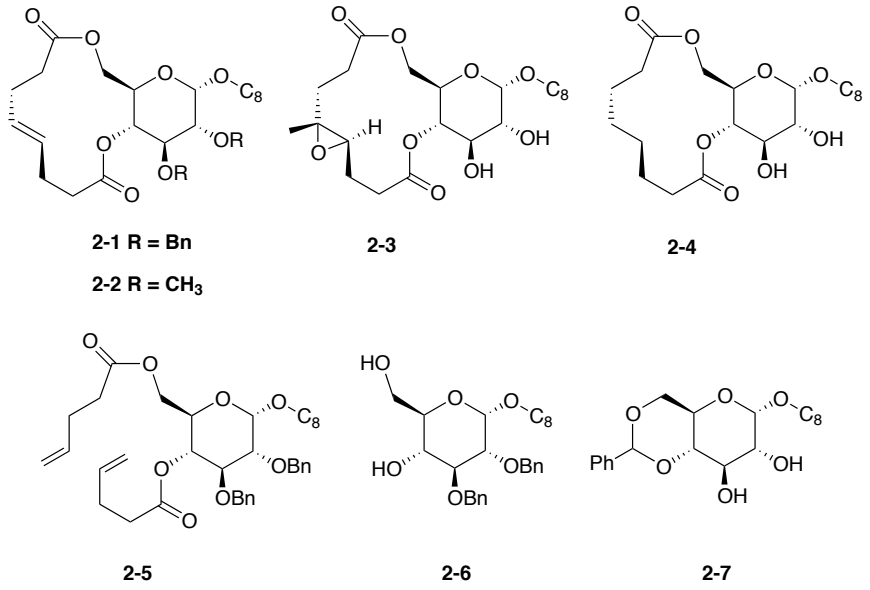

Fig. 2-4. Representative carbohydrate-fused [13]-macrodilactones and synthetic precursors tested for cell viability assay. The top compounds are octylglucoside-fused [13]-macrodilactones while the bottoms ones are some of the intermediate molecules during the synthesis. Compounds **2-1**, **2-2** and **2-3** were the octylglucoside-fused [13]-macrodilactones active at the qualitative scratch-wound assays.

Table 2-2. SAR in cell viability assay

Compound	MIC (μM)	IC_{50} (μM)	95% CI (μM)	MLC (μM)	Therapeutic Index (MLC/MIC)
2-1	10	85.1	82.8 – 87.4	300	30
2-2	50	91.4	89.2 – 93.6	300	6
2-3	50	107	102.6 – 111.5	> 300	6
2-4	10	38.1	37.3 – 38.8	50	5
2-5	25	52.9	51.2 – 53.8	75	3
2-6	25	61.1	60.1 – 60.2	100	4
2-7	10	47.1	43.8 – 50.1	75	7.5

In the cell viability assay, all the active compounds contain an octylglucoside moiety, which suggest that the pharmacophore for the antiproliferative activities of this family of compounds is octylglucoside itself (Table 2-2). The IC_{50} of all the active compounds fall within the same range. However, the toxicity and the therapeutic index considerably vary with the identity of the fused cyclic molecule with compound **2-1** (with a fused [13]-macrodilactone and with a benzyl protection at C2, C3 hydroxyl of the sugar moiety) having at most 10-fold higher therapeutic index. In chapter one, we observed that the [13]-macrodilactone adopts different shapes depending on the configuration of the stereogenic plane and the stereogenic centers on the ring. It is possible that the improvement in therapeutic profile of **2-1** resulted from an optimized ring scaffold that allowed for better orientation of the pharmacophoric unit – the octyl glucoside – around the binding site of its target biomolecule. This suggests that varying or fine-tuning the macrocycle attached or fused to a pharmacophore of bioactive small molecules can potentially optimize the biological properties of these molecules.

2.4.2 Results and discussion for screening of Chembridge synthetic compound library

From the 12, 720 Chembridge synthetic small molecule library, only 1,232 were active at 50μM, which is 10% of the total number of molecules screened (Table 2-1). The hit rate at lower concentrations is 0.4%, 0.2%, 0.1% at 10μM, 2μM and 400nM respectively with no compounds active at concentrations lower than 400nM. This hit rate is lower than the hit rate for the natural product compound library, which is expected for synthetic compound libraries. However, the structures of the molecule hits from synthetic compound library are significantly less complicated than the natural product and thus

would be more amenable for SAR studies. Moreover, the synthetic molecule hits are more likely to be novel structures (less explored than natural product molecules) with potentially novel target and mechanisms of action and thus have huge potential as small molecule probes. The most promising hits, among the 19 synthetic small molecules active at 400nM, are shown in Fig. 2-5. These six molecules are not toxic at this concentration and the wound-area of MDA-MB-231 monolayer treated with these compounds is still widely open after 24 hours compared to the DMSO-treated cells. These molecules can be good lead compounds for SAR, target ID and mechanisms of action studies.

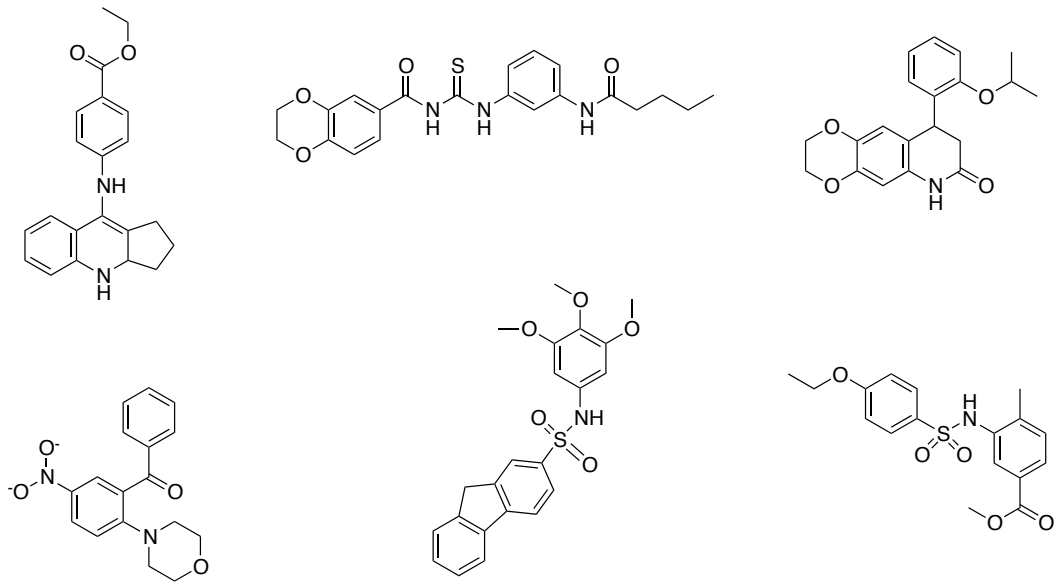

Figure 2-5. Most promising hits from screening of Chembridge synthetic compound library for MDA-MB-231 breast cancer cell migration inhibitors.

2.4.3 Results and discussion for screening of Analyticon natural product compound library

The hit rate for natural product library screening is higher (6%, 1.4%, 1.0%, 0.7%, 0.7% at 50μM, 10μM, 2μM, 400nM, 80nM respectively) than the hit rate for synthetic small molecule screening (Table 2-1). This is to be expected since the natural product is most likely to be biologically active. The structures of the natural product hits at 50 μM are shown in Appendix with the corresponding toxicity profiles as assessed using a qualitative trypan blue assay[22]. Some of the natural product families found were: cinchona alkaloids (5 compounds) – antimalarial; tricothecenes (5) – protein synthesis inhibitors; thapsigargins (4) – Sarco/Endoplasmic Reticulum Ca^{2+} ATPase (SERCA) inhibitors; Sesquiterpenes (5); Indoloquinolizidines (4); Cardiac glycosides (9); colchicine (1) – microtubule polymerization inhibitor; curvularin (1) and other alkaloids. The most promising compounds were further characterized using the quantitative scratch-wound assay. The antimigartory activity profile of some of these compounds is summarized in Table 2-4 and the full data for all the compounds characterized can be found in Appendix. Among these natural product hits, ouabain was chosen as a lead compound for further characterization.

Table 2-3. Antimigratory profiles of the most promising hits from the analyticon natural product compound screening.

Compound	MIC (µM)	IC50 (µM)	MLC (µM)	TI (µM)
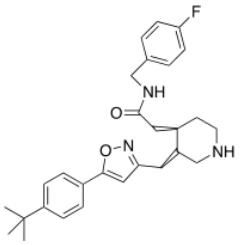	6.25	NA	12.5	2
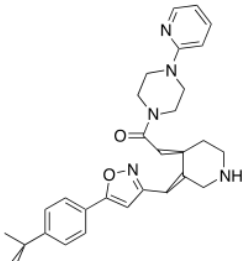	6.25	5.8	25	4
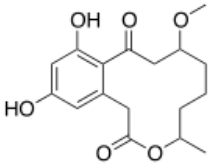 curvularin	3.125	36	> 50	> 16
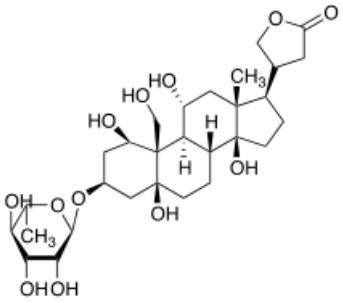 cardiac glycoside (ouabain)	0.061	0.173	>100	>1600

2.5 Cardiac glycosides as potent and selective inhibitor of Na^+/K^+ ATPase

In the course of screening libraries of small molecule and natural product compounds for cell migration inhibitors using our scratch-wound assay, cardiac glycosides were found to inhibit the migration of the human triple-negative breast cancer cell line MDA-MB-231 at submicromolar concentrations. The MDA-MB-231 line is a cellular model for triple-negative breast cancer, which is refractory to current chemotherapeutic options[23]. This chapter investigates how cardiac glycoside inhibited the migration of MDA-MB-231 breast cancer cells.

2.5.1 Cardiac glycosides – structural features and biological activities

Cardiac glycosides also referred to as cardiotonic steroids, are a group of natural products that share a common 'unique' steroidal core that is doubly substituted with a sugar at position 3 and an unsaturated lactone ring at position 17 (Fig. 2-6). Classification of cardiac glycosides depends on the type of lactone ring attached to the steroidal core where those with the lactone 2-furanone are called cardenolides (e.g., ouabain – the most highly studied cardiac glycoside, digitoxin and UNBS1450) and those with lactone 2-pyrone are called bufadienolides (e.g., bufalin and marinobufagenin). The C3 position can be ornate with different types and numbers of sugars such as glucose, rhamnose etc. The steroidal core is also ornate with various substituents at different positions but the unique cic/cis configuration at the A/B and C/D ring junctions is preserved through out the entire cardiac glycoside family. This unique configuration at the two ring junctions resulted to a cup-shaped structure - with two distinct α and β

surfaces (Fig. 2-6 – top right structure) - rather than the flat planar structure inherent to common steroids with trans configurations.

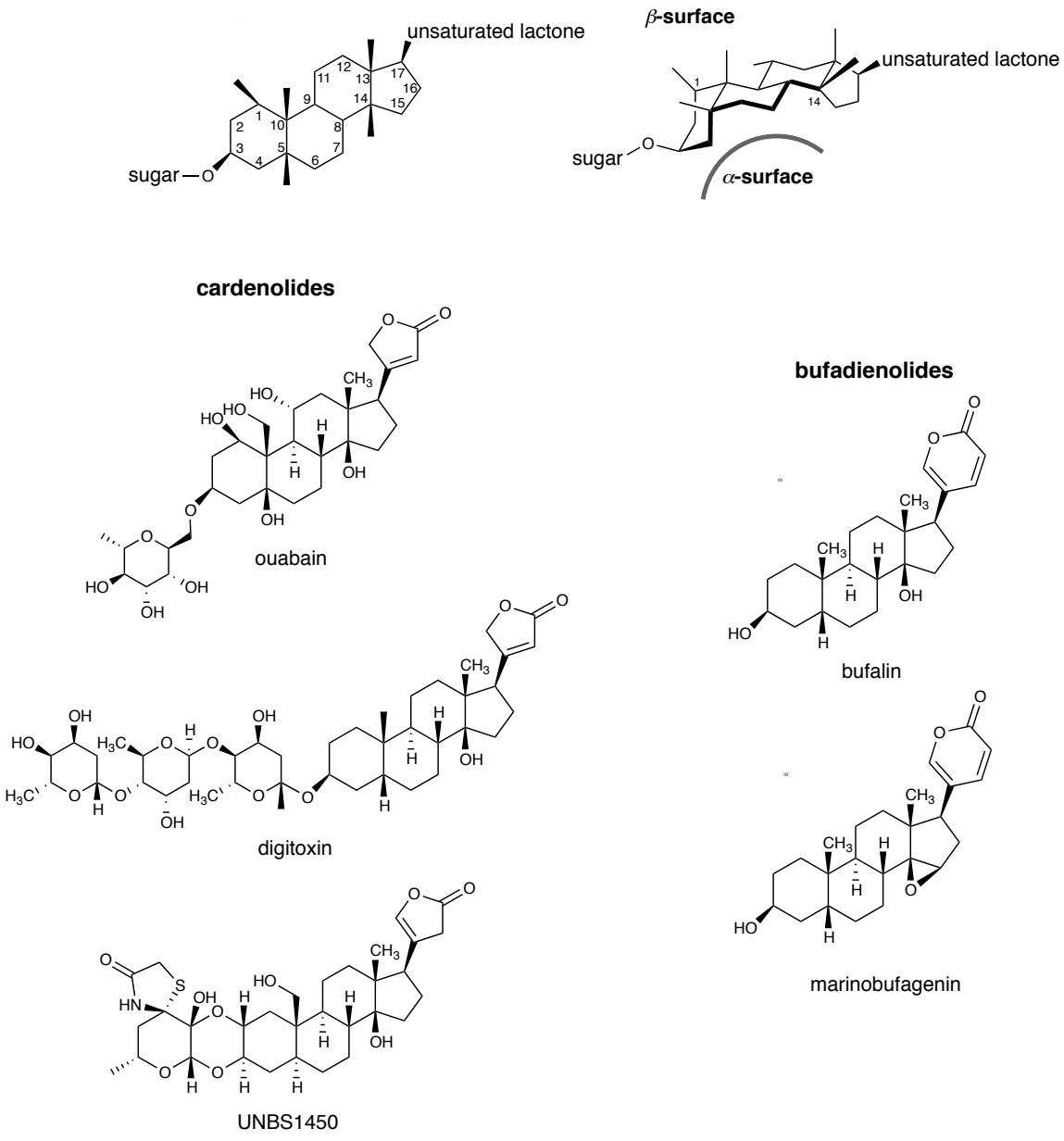

Fig. 2-6. Structural properties of cardiac glycosides and representative members of cardiac glycoside family.

A number of cardiac glycosides such as digitoxin have long been used as positive inotropic drugs for treatment of congestive heart failure by inhibiting the Na^+ and K^+

antiport activity of Na^+/K^+ ATPase[24]. Over the last 20 years, interest in cardiac glycosides has grown tremendously due to their promising anti-cancer properties[25] . The steroid core with distinct *cis* confiugrations at the A/B and C/D ring junctures is the active pharmacophore[26] . It is the minimum structure required for Na^+ pump inhibition through induction of protein conformational change at the receptor level. The lactone ring is not rigorously part of the pharmacophore but it amplifies the affinity of the steroid core with the protein. The sugar moiety affects the potency as well as the pharmacokinetic and pharmacodynamic properties of the cardiac glycosides[27]. This SAR information is only a fraction of the numerous studies on the SAR of various cardiac glycosides with respect to inhibition of Na^+/K^+ ATPase and its anti-cancer activities. However, no SAR study that is focused on the antimigratory activity of cardiac glycosides in breast cancer cells has been reported.

2.5.2 Na^+/K^+ ATPase – a multifunctional protein

Na^+/K^+ ATPase, the largest member of P-type cation pumps, is responsible for the transport of three Na^+ ions out of and two K^+ ions into the cell against their physiological concentration gradient[28]. This transport is powered by ATP hydrolysis and is estimated to account for 30% of all cell's energy consumption at rest[29]. Active transport of Na^+ and K^+ ions in and out of the cell generates an electric potential gradient across the plasma membrane and maintains the resting potential of cells and thus the activity of this pump is critical for regulation of cell volume, contraction of heart muscle cells and mobilization of ions such as calcium and other molecules in and out of the cell[28].

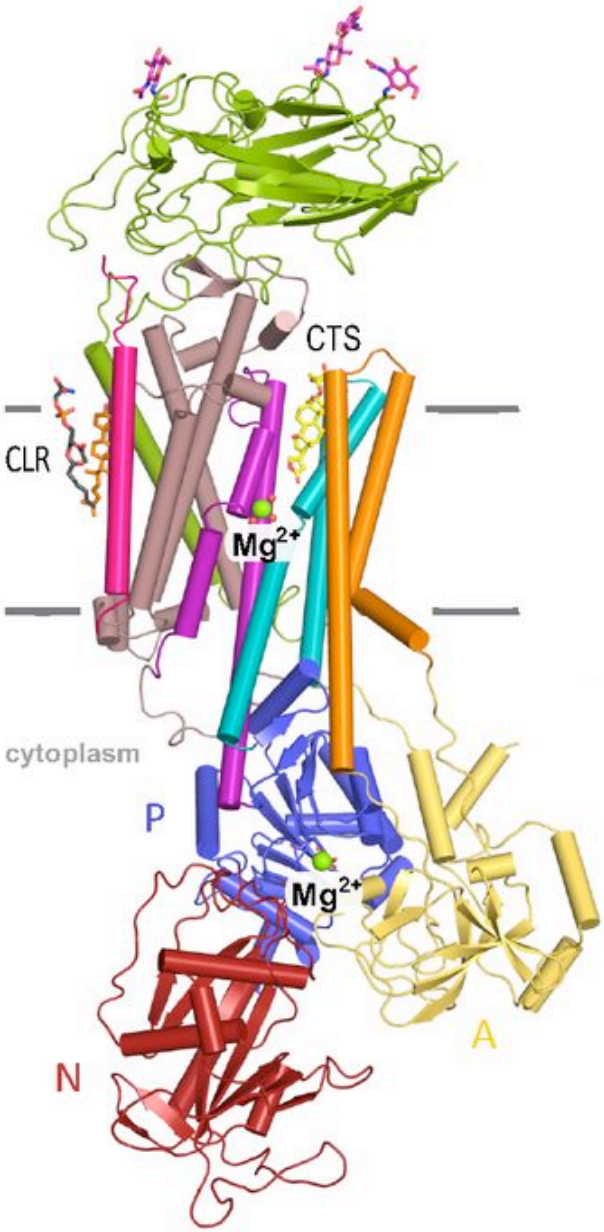

Fig. 2-7. Cartoon representation of X-ray cystal structure of the high-affinity Na^+/K^+ ATPase E2P–ouabain complex (3.4 A resolution)[30]. The E2P–ouabain complex is depicted using the following color codes: red [nucleotide binding (N) domain], blue [phosphorylation (P) domain], light yellow [actuator (A) domain], orange (αM1–2), teal (αM3–4), purple (αM5–6), brown (αM7–10), green (β-subunit), and deep pink (γ-subunit). The CTS binding site is marked CTS. Ouabain is represented by yellow sticks, Mg^{2+} and the three water molecules by light green and red spheres, respectively. The figure was reused from reference 30.

In general the Na^+/K^+ ATPase consists of three subunits (Fig. 2-7)[30]. The larger α subunit is the catalytic site. It contains the nucleotide binding (N), phosphorylation (P), and actuator (A) domains, and the biniding sites for Na^+, K^+, Mg^{2+} as well as the highly conserved cardiac glycoside binding site in a vestibule formed by the αM1-M6 helices. It also contains the controversial phosphorylation sites proposed to be involved in the signaling function of the Na^+/K^+ pump[31]. The β subunit is the extracellular glycoprotein (green) mainly important for the recruitment of the α subunit to the plasma membrane. The γ (FXYD) subunit regulates the kinetic properties of the pump as well as its tissue specificity. To add to the complexity of this pump, the α and β subunits exists in different isoforms depending on the cell type: the α subunit exists in four isoforms (α1-4) while the β in three (β1-3)[28].

Besides the ion-transport function, the Na^+/K^+ ATPase also probably has a signaling function. One theory is that a population of non-pumping Na^+/K^+ ATPase exist in a caveolae and forms a multi-protein signaling complex comprised of Src kinase, epidermal growth-factor receptor (EGFR), inositol 1,4,5 – triphosphate (IP3) receptor, and caveolins[31]. This signaling complex was proposed to activate two downstream signaling pathways. The first one is through the IP3 receptor-mediated calcium release that affects intracellular calcium oscillation[31c]. The second one is a protein-kinase cascade initiated by Src[31a, 31b]. These signaling cascades affect various cellular processes such as cell growth, motility, gene expression and some metabolic pathways.

2.5.3 Context-dependent dual mechanisms of actions of cardiac glycosides

Upon binding of cardiac glycosides to the α subunit of Na^+/K^+ ATPase, various biological and physiological effects were observed depending on the concentration of cardiac glycosides and the cell type used. Two mechanisms explain the sometimes, opposing cellular and physiological effect of cardiac glycoside[32].

2.5.3.1 The classical "Na^+ lag" model

The Na^+ lag model explains the positive inotropic effect of cardiac glycoside and its use as drugs for treatment of cardiac arrhythmia[33]. At concentrations >100 nM, cardiac glycosides cause the classical inhibition of ion transport function of the Na^+/K^+ ATPase. This inhibition leads to an increase in intracellular Na^+ ion which then activates the reverse mode of Na^+/Ca^{2+} exchanger resulting in an increased intracellular Ca^{2+} concentration. Increase in intracellular calcium leads to increase in muscle contraction, blood pressure and Na^+ excretion (Fig. 2-8a).

2.5.3.2 The Na^+K^+ ATPase signalosome model

The receptor function of Na^+/K^+ ATPase is explained by the Na^+/K^+ ATPase signalosome model[31]. This model calls for the existence of a population of nonpumping Na^+/K^+ ATPases that resides in a caveoli and act as a scaffold for the assembly of multi-protein signaling domain that transmits signals to different intracellular compartments. Some members of this complex that has been identified include Src kinase, epidermal growth-factor receptor (EGFR), inositol 1,4,5-triphosphate (IP3) receptor and caveolins. The model explains that low concentrations of ouabian is not enough for the inhibition of

the pumping Na^+/K^+ ATPase but is enough to activate the non pumping population and trigger a signaling cascade that affects a number of cellular processes such as gene expression, proliferation and adhesion.

At least two signaling mechanisms were proposed to get activated by binding of cardiac glycosides to the Na^+/K^+ ATPase signalosome. The first is the signaling through alterations in intracellular calcium oscillations[31c]. Although not yet fully defined, it was proposed that phospholipase C (PLC) and IP3 are recruited in the Na^+/K^+ ATPase signalosome and forms a functional microdomain. This brings the cytosolic part of the sodium pump in direct contact with IP3 receptor of the endoplasmic reticulum, which results to repeated transient oscillation of calcium ions. The other signaling proposed is through Ras activation[31a, 31b] (Fig. 2-8b). Binding of low concentrations of cardiac glycoside to the Na^+/K^+ ATPase signalosome releases Src, which transactivates the EGFR that eventually lead to activation of mitogen-activated protein (MAP) kinase cascade that affects various cellular processes under the control of MAP kinase such as gene expression, proliferation and some metabolic processes.

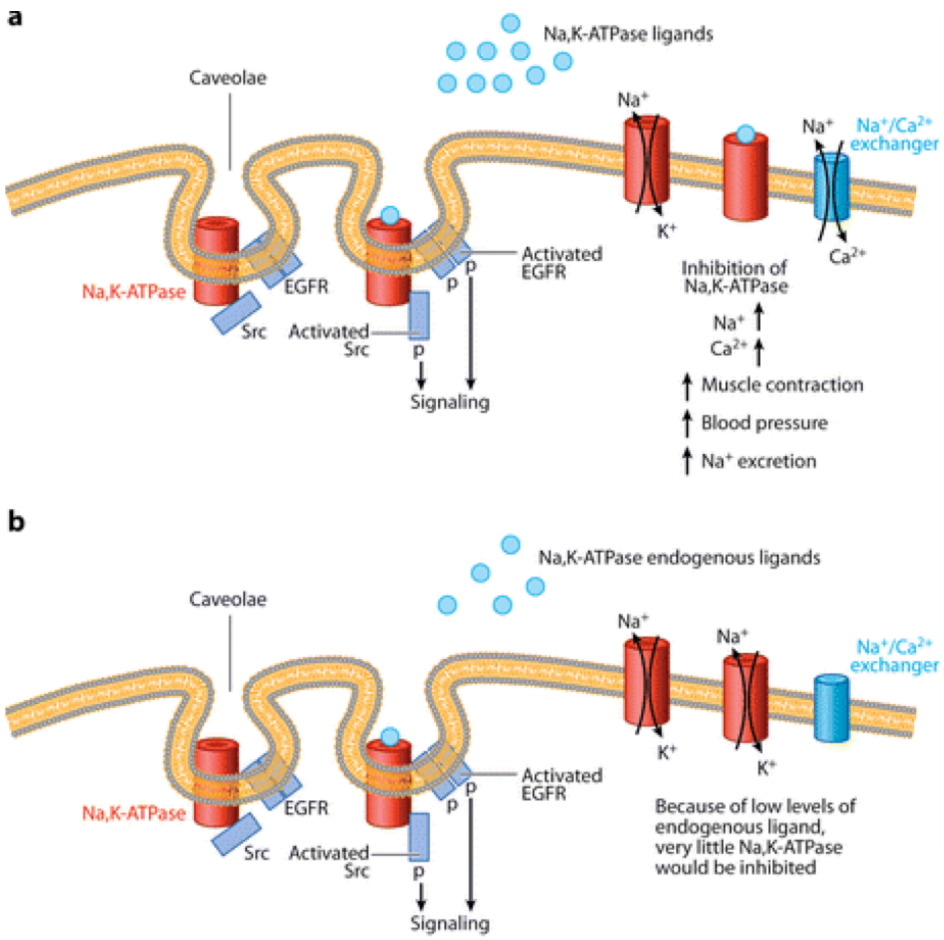

Fig. 2-8. Two models that explain the dual mechanisms of actions of cardiac glycosides are the (a) Na^+ lag hypothesis and (b) Na^+/K^+ ATPase signalosome model. The figure was reused from reference 32.

2.6 Investigation of the antimigratory mechanism of action of cardiac glycosides in MDA-MB-231 breast cancer cell migration

2.6.1 Motivation and research question

The dual function of the Na^+/K^+ ATPase result in dual mechanisms of actions attributed to cardiac glycoside's biological activities. The specific operative mechanism of action of cardiac glycosides is highly dependent on the concentration of cardiac glycoside and the cell type used. Some examples of the context-dependent mechanism of action of cardiac glycoside are discussed below.

Some cardiac glycosides inhibit the migration and proliferation of various cell types without affecting the ion-transport function of the Na^+/K^+ ATPase, thus supporting the nonclassical Na^+/K^+ ATPase signalosome model for mode of action of cardiac glycosides. Marinobufagenin, an endogenous mammalian cardiotonic steroid inhibits proliferation and growth factor induced migration and invasion of cytotrophoblast and Chinese hamster ovarian cells in vitro at low nanomolar concentration[34] . The mechanism involved a decrease in ERK1/2 activity and activation of p38 and Jnk pathways. Since ouabain showed similar activities in both cell lines, they speculated that Na^+/K^+ ATPase might be involved; however, no direct correlation was made between inhibition of cell migration and inhibition of Na^+/K^+ ATPase[35]. UNBS-1450 is another novel cardenolide that inhibited the proliferation and migration of non-small cell lung cancer cells, glioma cells, prostate cancer cells and metastatic melanoma cells at concentrations that does not affect the ion transport activity of the pump[36]. Inhibition of the α sub-unit of Na^+/K^+ ATPase by UNBS-1450 led to a sharp decrease in intracellular ATP concentration

causing disorganization of actin cytoskeleton and induction of proautophagic cytotoxic effects[37].

After discovering that cardiac glycosides inhibit the migration of MDA-MB-231 cells, we endeavored to define the specific role of Na^+/K^+ ATPase (classical versus nonclassical) in migration of MDA-MB-231 breast cancer cells. Understanding which of the two functions of Na^+/K^+ ATPase is operative in the observed antimigratory activities of cardiac glycoside in MDA-MB-231 breast cancer cell migration can contribute to a fundamental understanding of triple negative breast cancer migration and can potentially open up new avenues for therapeutic interventions.

2.6.2 Research design and strategy

To investigate which function of the Na^+/K^+ ATPase is operative in the antimigratory activity of cardiac glycosides (CGs); we developed a strategy called correlative SAR. Traditional SAR studies guide improvements of small molecule potency and selectivity for a given target. On the other hand, we define correlative SAR as a strategy to expand the use of existing biologically active compounds to address some of the major challenges in the postgenomic era: annotating protein functions and linking those functions to an observed phenotype. In contrast to traditional SAR, correaltive SAR takes advantage of a distinct pattern of structural requirements for activity by a group of related molecules (SAR profile) across a series of assays. The SAR profiles are then used to establish relationships between a protein or cellular system and bona fide biological processes, that is, linking specific protein function to a cellular phenotype (Fig. 2-9). Direct correlation of SAR profiles for protein function and a cellular phenotype then

implicates a role for the protein in the phenotype. The correlative SAR strategy is especially useful for multifunctional proteins and moonlighting proteins[38]. Correlative SAR employs small molecule probes and thus shares the complementarity and advantages of small molecules over genetics and RNA interference techniques for annotating protein functions.

In this study, we use correlative SAR to determine what role the Na^+/K^+ ATPase plays (classical versus non-classical) in migration of MDA-MB-231 breast cancer cells (Fig. 2-9). Our strategy first involved synthesis of analogs containing modifications on key parts of ouabain and digitoxin – two widely studied cardiac glycosides. The analogs contain a modification on the sugar, steroid core or lactone ring of each CG. Next, SAR was established at different levels of resolution with respect to inhibition of cell migration (cellular), inhibition of the Na^+/K^+ ATPase activity in vitro (molecular), and orientation in the cardiac glycoside binding site of Na^+/K^+ ATPase (atomic). We evaluated whether inhibition of cell migration was separable from inhibition of the Na^+/K^+ antiport pump by correlating the SAR profiles of ouabain in each of these assays. In addition, to determine whether the inhibition of cell migration resulted from general inhibition of the Na^+/K^+ ATPase or if it is confined to an effect of CGs, other structurally unique Na^+/K^+ ATPase inhibitors were tested for their antimigratory activity. A small molecule inhibitor that does not activate the Src signaling pathway but inhibits the ion pump was also tested in the cell migration assay. To our knowledge, no SAR study on the antimigratory activity of cardiac glycosides in MDA-MB-231 breast cancer cells has been reported prior to this work. Furthermore, the current study shows the utility of

correlative SAR to establish links between specific protein functions and cellular phenotypes.

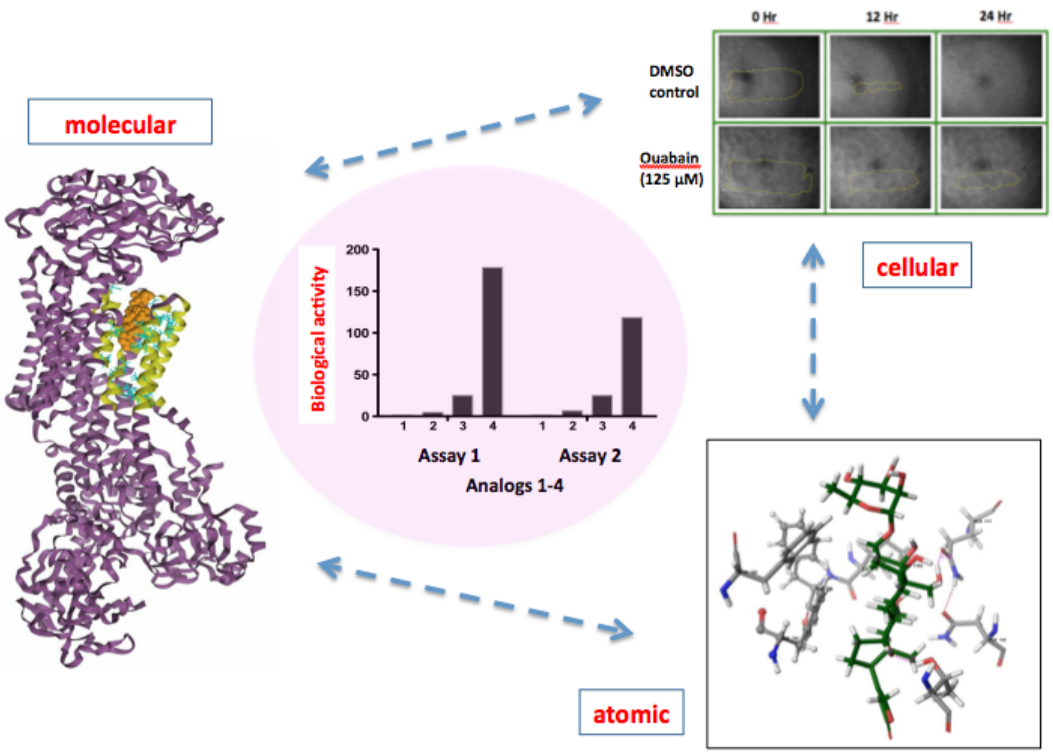

Fig. 2-9. Research strategy – correlative SAR. The pattern of activity modulation by different analogs in different assays (i.e. correspondence in decrease in potency between different analogs) is used as a probe to link various biochemical and cellular activities of small molecules. If the pattern correlates, then the biological activities are more probably directly related. Three analogs of a cardiac glycoside, ouabain, was synthesized and assayed with respect to inhibition of cell migration (cellular), inhibition of the Na^+/K^+ ATPase activity in vitro (molecular), and orientation in the cardiac glycoside binding site of Na^+/K^+ ATPase (atomic). The SAR profiles in each of these assays were correlated to look at the relationship between ouabain- Na^+/K^+ ATPase interaction at atomic and molecular level and the observed effect of ouabain in cellular migration.

2.7 Correlative SAR of ouabain and analogs in cellular and molecular level

2.7.1 Semi-synthesis of ouabain analogs

Three analogs of ouabain **2-8** were synthesized (**2-9** – **2-11**, Scheme 1) by methods that had been reported previously in the literature[39]. The derivatives were prepared, starting from ouabain itself, by removal of the sugar moiety (**2-9**), reduction of the lactone ring (**2-10**) and modification of the steroid core (**2-11**). Hydrolysis of the glycosidic linkage between the L-rhamnose and steroid core provided ouabagenin **2-9**. Reduction of the butenolide olefin by hydrogenation provided analog **2-10**. Compound **2-11** contains an acetonide group that links the C1 and C19 hydroxyl groups. The analogs were chosen because they were synthetically accessible and because they consisted of variations of the key structural segments of the parent compound in a way that would allow for a reasonably comprehensive SAR profile.

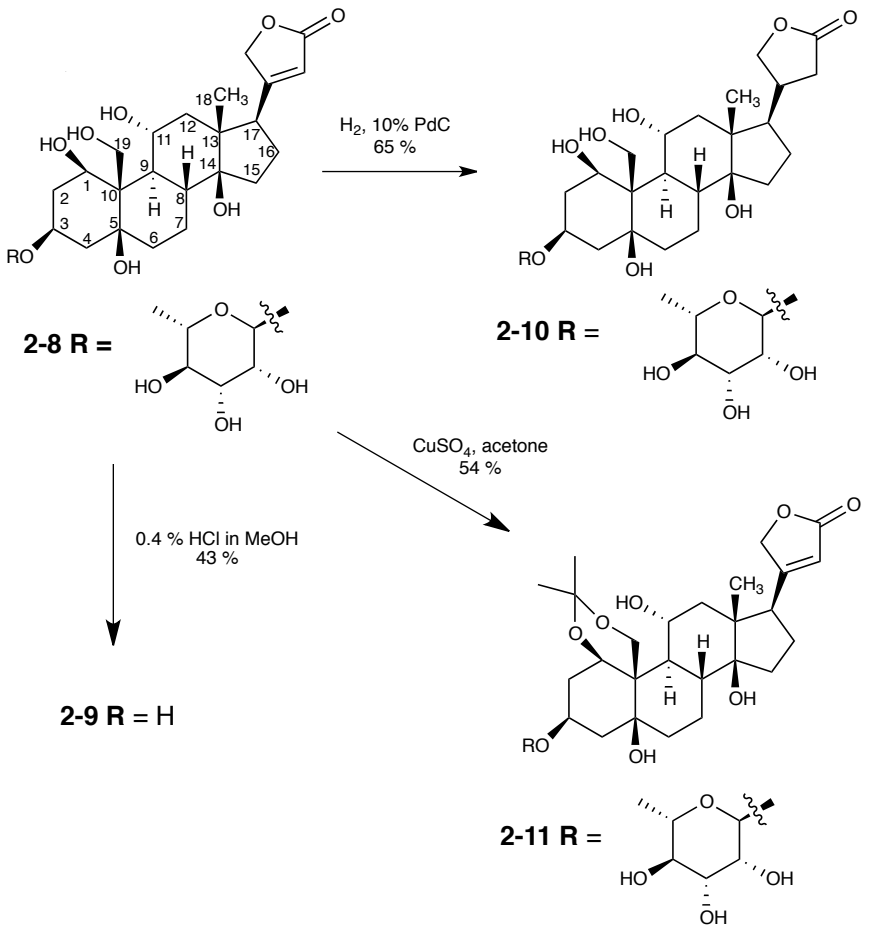

Scheme 2-1. Semi-synthesis of ouabain analogs.

2.7.2 SAR profile of ouabain and analogs in MDA-MB-231 breast cancer cell migration assay

The MDA-MB-231 breast cancer cell line was chosen for the scratch-wound cell migration assay. MDA-MB-231, a cellular model for triple negative breast cancer has an invasive phenotype and is metastatic in animal models. The assay involved mechanical wounding of a confluent monolayer of cells with a pipet tip after treatment with different concentrations of compounds or DMSO (vehicle) alone. The progress of wound closure was monitored by analysis of digital microscope images of the wounds at different times

postwounding. The area of the wound at each time point was calculated with the public-domain ImageJ program, and statistical significance was tested with a two-tailed Student's *t*-test. Three independent experiments were done with triplicates for each concentration of each compound.

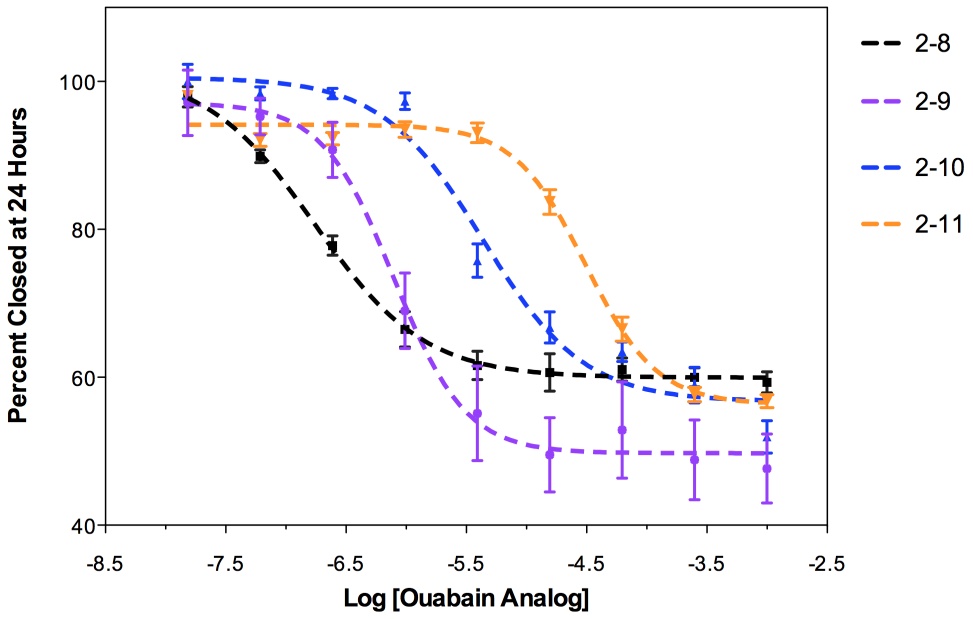

Fig. 2-10. IC_{50} curves for cell migration inhibition by ouabain **2-8** and analogs **2-9** to **2-11**.

Based on the IC_{50} values for inhibition of wound closure (Fig. 2-10 and Table 2-4), none of the synthesized analogs was more potent than the parent compound, ouabain **2-8** with an IC_{50} of 173 nM. However, the potency of the analogs varied with respect to the type of modification made to the structure of **2-8**. Ouabagenin **2-9**, which lacks the sugar moiety, had an IC_{50} value of 790 nM. The olefin of the butenolide was reduced to prepare compound **2-10**; its IC_{50} of 4.3 μM demonstrates that a simple modification to the

lactone segment results in a drop in potency by a factor of 25. It further suggests that the olefin is relatively important to the ability of cardiac glycosides to inhibit cell migration. A major decrease in potency (178-fold) was observed for ouabain analog **2-11**, which contains a C1, C19 acetonide group. Modification to the steroid core and specifically the introduction of a bulky group on the concave face of the cup-shaped steroid greatly reduced the antimigratory activity of ouabain. The SAR profile (pattern of structural requirement for activity modulation) for antimigratory activity is: modification on steroid core > modification on lactone ring > modification on sugar in decreasing impact on potency (Fig. 2-11a).

2.7.3 Correlative SAR of ouabain and analogs in MDA-MB-231 breast cancer cell migration assay (cellular level) and Na/K ATPase assay (molecular level)

Ouabain is a potent and specific inhibitor of the Na^+/K^+ ATPase. The Na^+/K^+ ATPase is a transmembrane antiport ion transporter that pumps three Na^+ ions out of the cell for every two K^+ ions pumped into the cell against their concentration gradients for each molecule of ATP hydrolyzed. Besides its ion-transport function, this protein complex also functions as a receptor for ouabain and has been implicated in processes and key cellular elements that affect cell motility such as cell tight junctions[40] cell contacts[41] and actin dynamics[42]. We investigated whether the antimigratory effect of ouabain was linked to the classical inhibition of Na^+/K^+ ATPase or stimulation of its receptor function[31] using correlative SAR. Specifically, we looked at the SAR profile of ouabain in a Na^+/K^+ ATPase activity assay and correlated it to the SAR profile for antimigratory activity.

Table 2-4. IC_{50} values (μM) for the inhibitory activity of ouabain and analogs in the Na^+/K^+ ATPase assay and cell migration assay

Ouabain and analogs	Na^+/K^+ ATPase		Cell migration	
	IC_{50} (μM)	**95% CI**	**IC_{50}**	**95% CI**
2-8 (ouabain)	0.105	0.031 - 0.352	0.173	0.100-0.300
2-9	0.669	0.526 – 0.850	0.790	0.637 – 0.979
2-10	2.6	0.823 – 8.46	4.3	3.02 – 6.21
2-11	12.4	8.98 – 17.2	30.9	25.2 – 38.0

The SAR profile in Na^+/K^+ ATPase inhibition is similar to inhibition of cell migration (Table 2-4 and Fig. 2-11a). Compound **2-9**, with the cleaved sugar moiety, had a potency that is relatively similar to the parent compound ouabain **2-8**. This implies that for inhibition of Na^+/K^+ ATPase activity, as for inhibition of cell migration, the sugar moiety is less important than other parts of the molecule. Compound **2-10**, with the saturated lactone ring, displays the next lowest decrease in potency, while **2-11**, with the bulky acetonide group on the steroid core, shows the greatest decrease in potency. The IC_{50} values of ouabain and its analogs for inhibition of Na^+/K^+ ATPase activity and the values for inhibition of cell migration fall within the same range. The distinct pattern of modulation in Na^+/K^+ ATPase activity by ouabain and the analogs, as measured by both IC_{50} (Figs. 2-11a,b) and dose–response for ouabain alone (Fig. 2-11c) and for combined ouabain and analogs (Fig. 2-11d) correlates well with the pattern observed for their effect on cell migration. The correlation suggests that the inhibition of cell migration is directly related to the inhibition of Na^+/K^+ ATPase activity.

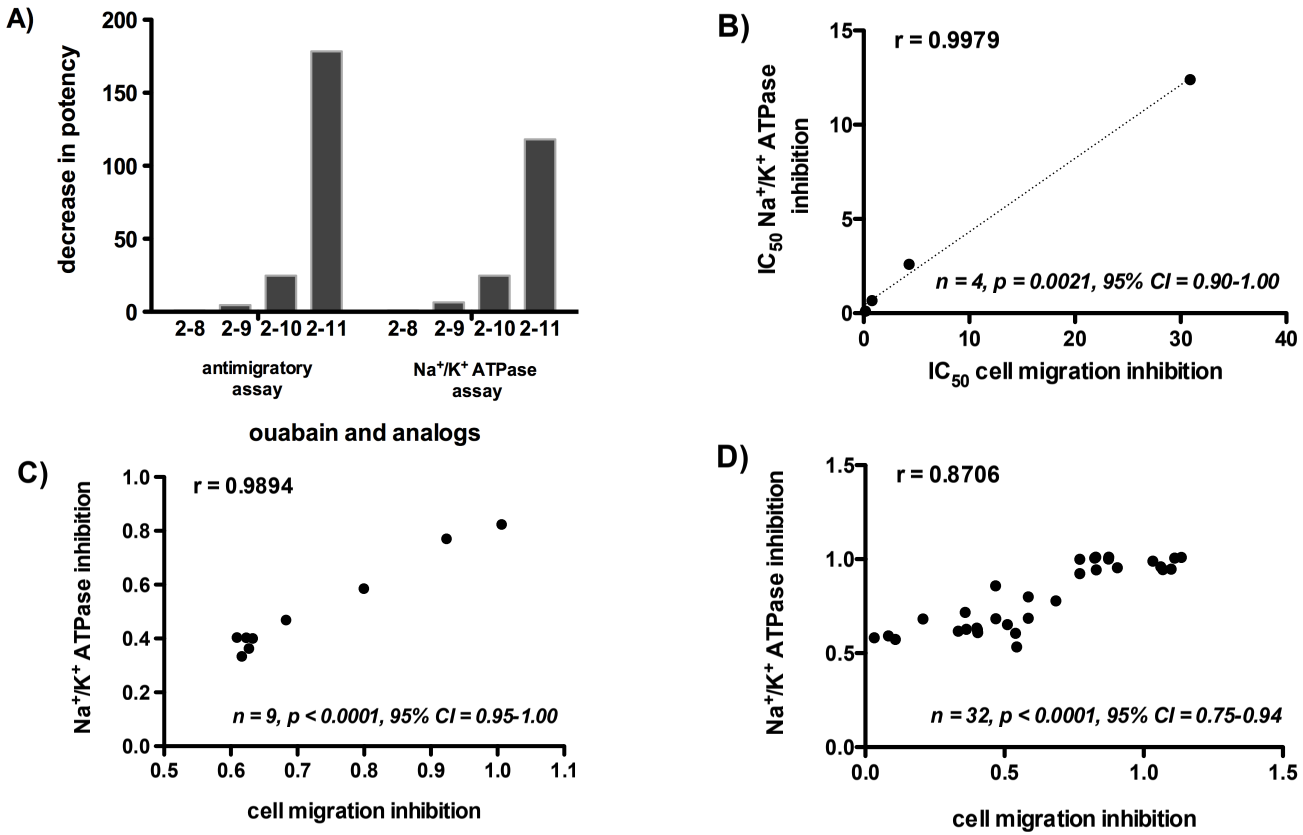

Fig. 2-11. Correlative SAR of ouabain and analogs at molecular and cellular levels**.** (A) Decrease in potency of ouabain analogs in the cell migration assay and the Na^+/K^+ ATPase assay (SAR profile). (B) Pearson correlation plot for IC_{50} values of ouabain and analogs in the antimigratory assay and the Na^+/K^+ ATPase assay (correlative SAR). (C) Pearson correlation plot for ouabain's inhibition of Na^+/K^+ ATPase and cell migration at different concentrations. (D) Pearson correlation plot for inhibition of Na^+/K^+ ATPase and cell migration by ouabain and analogs at different concentrations.

2.8 Correlative SAR of digitoxin and analogs in cellular and molecular levels

We were curious to see if the SAR results for ouabain apply to other members of cardiac glycoside family of natural products. Evidence showed that ouabain and digitalis cardiac glycosides develop their effect in different cellular spaces and thus have different therapeutic profiles[43]. Ouabain's mode of action starts by binding to the α subunit of the Na^+/K^+ pump from the extracellular side. This binding affects cellular functions either through activation of different signal transduction pathways (Src and IP3) or through perturbation of intracellular Na^+, K^+ and Ca^+ ion concentrations. Digitalis cardiac glycosides such as digitoxin on the other hand penetrates the cell's interior and interacts with intracellular ryanodine receptors leading to the release of Ca^{2+} from the sarcoplasmic reticulum[43]. To explore if the SAR-correlation results for ouabain applies to other cardiac glycosides, analogs of digitoxin were synthesized employing the same transformation as that used for ouabain **2-8** followed by correlative SAR. It would be interesting to know if the correlative SAR for digitoxin would be similar to ouabain despite having different modes of action.

2.8.1 Semisynthesis of digitoxin and analogs

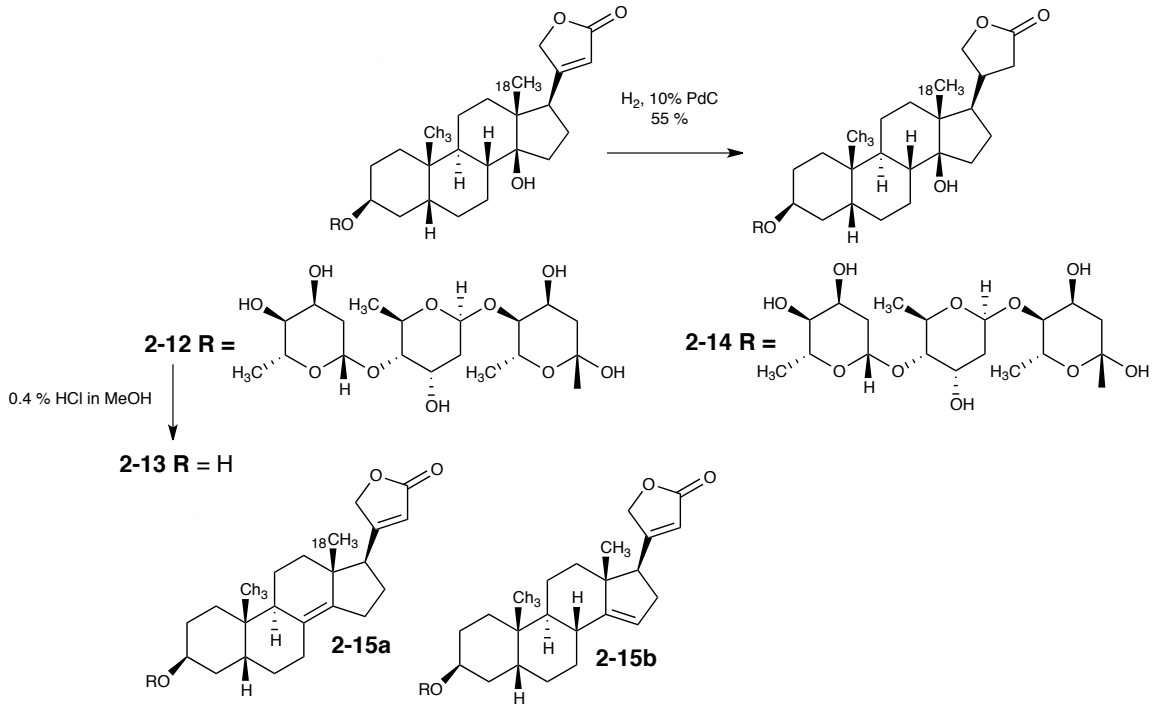

Scheme 2-2. Semi-synthesis of digitoxin analogs **2-13** to **2-15**.

Scheme 2 shows the reactions for the partial synthesis of digitoxin analogs **2-13** to **2-15**. An additional product from the deglycosylation of digitoxin, a side product (**2-15a, 2-15b**), was obtained which was found to be a mixture of alkene isomers produced from dehydration across the hydroxyl-containing carbon of rings C and D and the carbon directly adjacent to it which is at the junction of rings B and C. Similar to ouabain analogs, the synthesized digitoxin analogs each contains modification on either the sugar, lactone or steroid core. Compound **2-13** contains modification on sugar, compound **2-14**

on lactone ring while compounds **2-15a** and **2-15b** contain modification on the cup shaped steroidal core.

2.8.2 Correlative SAR of digitoxin and analogs in MDA-MB-231 breast cancer cell migration assay (cellular level) and Na^+/K^+ ATPase assay (molecular level)

The same experimental approach (correlative SAR) done on oubain and analogs (**2-8** to **2-11**) was performed on digitoxin and analogs (**2-12** to **2-15**). The results (Table 2-5 and Fig. 2-12) were similar to that of the ouabain series. A SAR trend in cell migration inhibition assay was observed in Na^+/K^+ ATPase assay (Fig. 2-12a). The analog in which sugar is cleaved is the most potent (compound **2-13**) followed by compound **2-14** with modification on the lactone ring and the least potent ones are compounds **2-15a** and **2-15b** with modification on the steroid core. Similar to addition of a bulky acetonide group that links the C1 and C19 hydroxyl groups of oubain's steroidal core, introduction of unsaturation to either ring B or C of digitoxin through the dehydration of the C-14 hydroxyl greatly reduced the potency of digitoxin. These results imply that, similar to oubain, the sugar is not that important while the structure of the steroid core is highly necessary for the inhibition of both cell migration and Na^+/K^+ ATPase. However, it seemed like modifying the structure of digitoxin has more pronounced effect in its ability to inhibit Na^+/K^+ ATPase than in its ability to inhibit cell migration as shown by the decrease in potency of digitoxin analogs for the two assays (Fig. 2-12a). Again, similar to the correlation of oubain SAR, the IC_{50}s of digitoxin for both antimigratory and Na^+/K^+ ATPase assays correlate very well (Fig. 2-12b). This result corroborates the initial conclusion that the observed antimigratory effect of cardiac

glycosides in MDA-MB-231 breast cancer cells is due to the inhibition of Na^+/K^+ ATPase's ion-transport function. The direct relationship between inhibition of Na^+/K^+ ATPase ion transport function and inhibition of cell migration seemed to be applicable to other members of the cardiac glycoside family of natural products.

Table 2-5. IC_{50} values (μM) for the inhibitory activity of digitoxin and analogs in Na^+/K^+ ATPase assay and cell migration assay.

Digitoxin and analogs	IC_{50} (μM) Na^+/K^+ ATPase inhibition	IC_{50} (μM) cell migration inhibition
2-12 (digitoxin)	0.005	0.046
2-13	0.097	0.260
2-14	0.691	2.15
2-15a and 2-15b	3.2	10.8

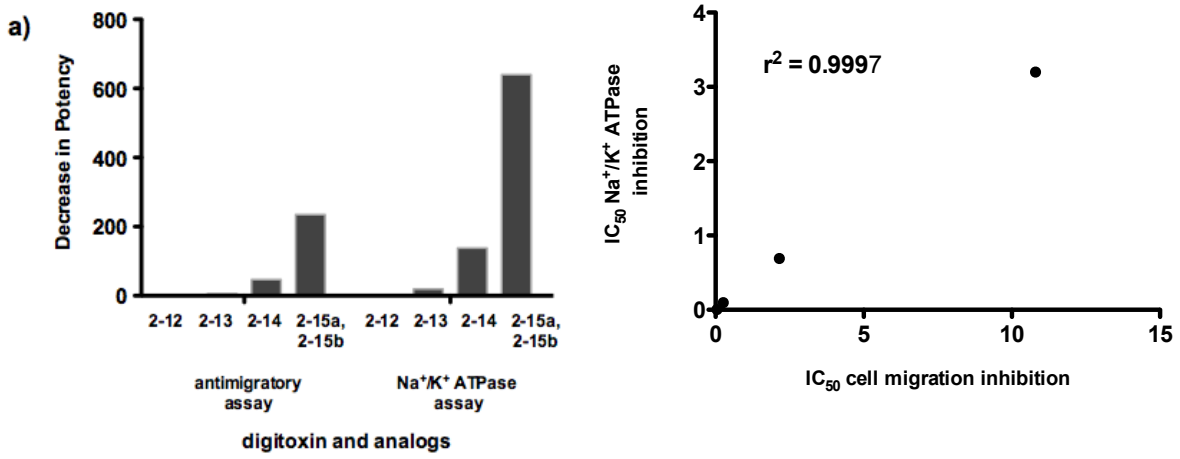

Fig. 2-12. (a) Decrease in potency of digitoxin analogs in antimigratory assay and Na^+/K^+ ATPase assays. (b) Pearson correlation plot for IC_{50} values of digitoxin and analogs in antimigratory assay and Na^+/K^+ ATPase assays.

2.9 Correlative SAR of ouabain and analogs at cellular, molecular and atomic level

One of the advantages of correlative SAR is its applicability in looking at small molecule effects in various level of resolution (cellular, molecular and atomic). Depending on the assay used, which probes for specific biological activities (biochemical or cellular; *in vitro* or in cellulo) or specific small molecule-protein interactions (using either actual small molecule-protein complex crystal structure or molecular docking experiments), the same set of structurally similar molecules can be used to link specific biochemical or cellular activities to protein-small molecule interactions at atomic level. We used molecular docking experiments to probe for SAR of ouabain and its analogs to its binding site on the Na^+/K^+ ATPase and use correlative SAR to link it to the SAR profile in cellular and molecular level discussed previously.

2.9.1 Molecular docking of ouabain and analogs in the α subunit of Na^+/K^+ ATPase

The ouabain binding site on the extracellular side of the α-subunit of the Na^+/K^+ ATPase is located in a cleft between the transmembrane segments αM1 and αM6[30, 44] (Fig. 2-13). Two orientations of ouabain to this site were originally proposed, one with the lactone ring facing toward the cytoplasmic side, as revealed by X-ray crystal structure studies[30, 44a, 44b] (Figs. 2-13, 2-14) and the other one with the lactone ring facing toward the extracellular side, as suggested by a lanthanide-based resonance energy transfer (LRET) experiment[44c]. Regardless of the two orientations of ouabain, all structural and functional studies agreed that the location of the cardiotonic steroid binding site is in the deep vestibule formed by the tansmembrane helices αM1–M6 (Figs. 2-13, 2-14). Most of these transmembrane helices constitute the cation permeation path (mapped in Fig. 2-13

and 2-14 as residues in cyan) that traverses the Na^+/K^+ pump from one side of the membrane to the other and passes through the ion-binding site II[45] (Figs. 2-13, 2-14, red circle), suggesting that ouabain acts by directly blocking the path of ions to prevent them from accessing their binding sites (Figs. 2-13, 2-14). Another possibility is that ouabain binding may lock the cation transport region into a configuration that prevents the pump from undergoing the conformational change required for ion transport[46]. Prior to this work, no experimental evidence linking ouabain's orientation to the cation permeation path and inhibition of Na^+/K^+ ATPase was available.

We investigated the interactions of ouabain and its analogs to Na^+/K^+ ATPase at the atomic level (Figs. 2-15, 2-16) by molecular docking experiments in an effort to rationalize the SAR results with respect to inhibition of Na^+/K^+ ATPase ion-transport function and cell migration. Fig. 2-16 shows the overlay between the docked ouabain and analogs and the actual ouabain-Na^+/K^+ ATPase crystal structure[30]. We explored how each modification on the ouabain structure affects binding energy (evaluated in the form of a docking score) and orientation relative to ouabain's structure in the cocrystal (evaluated in terms of a root-mean-square-deviation, RMSD) (Table 2-6). We then correlated the SAR profile for calculated RMSD (Fig. 2-17) and binding energy (Fig. 2-18) to the SAR profile for inhibition of Na^+/K^+ ATPase activity and inhibition of cell migration.

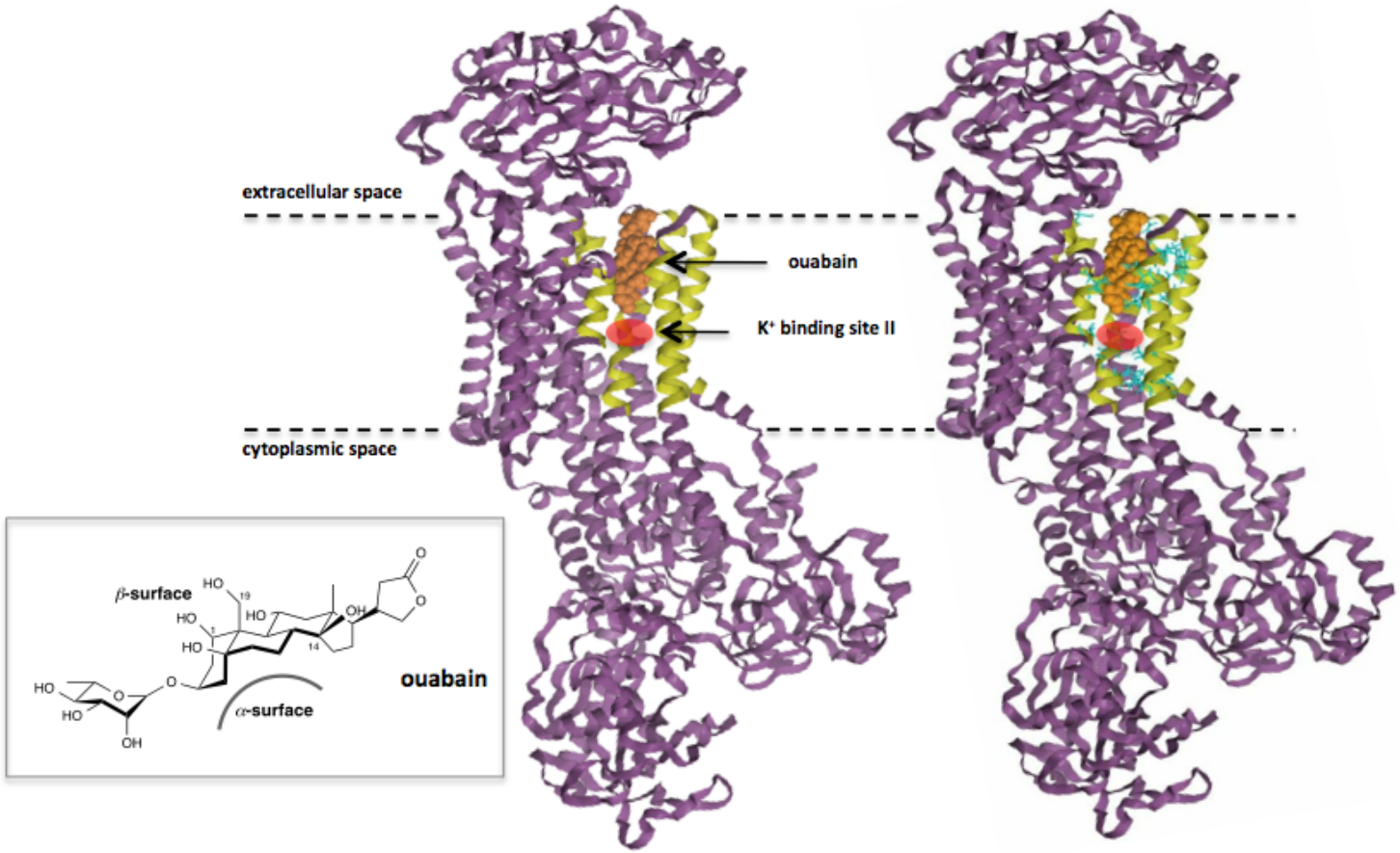

Fig.2-13. (A) Crystal structure (4HYT) of Na^+/K^+ ATPase with bound ouabain (orange) showing the binding site for ouabain – the vestibule formed by the αM1- αM6 helices (yellow). Shown in cyan are the residues involved in the cation permeation path and the K^+ binding site II. Structure in the box is the cup-shaped ouabain structure showing the hydrophobic α-surface and the polar β-surface.

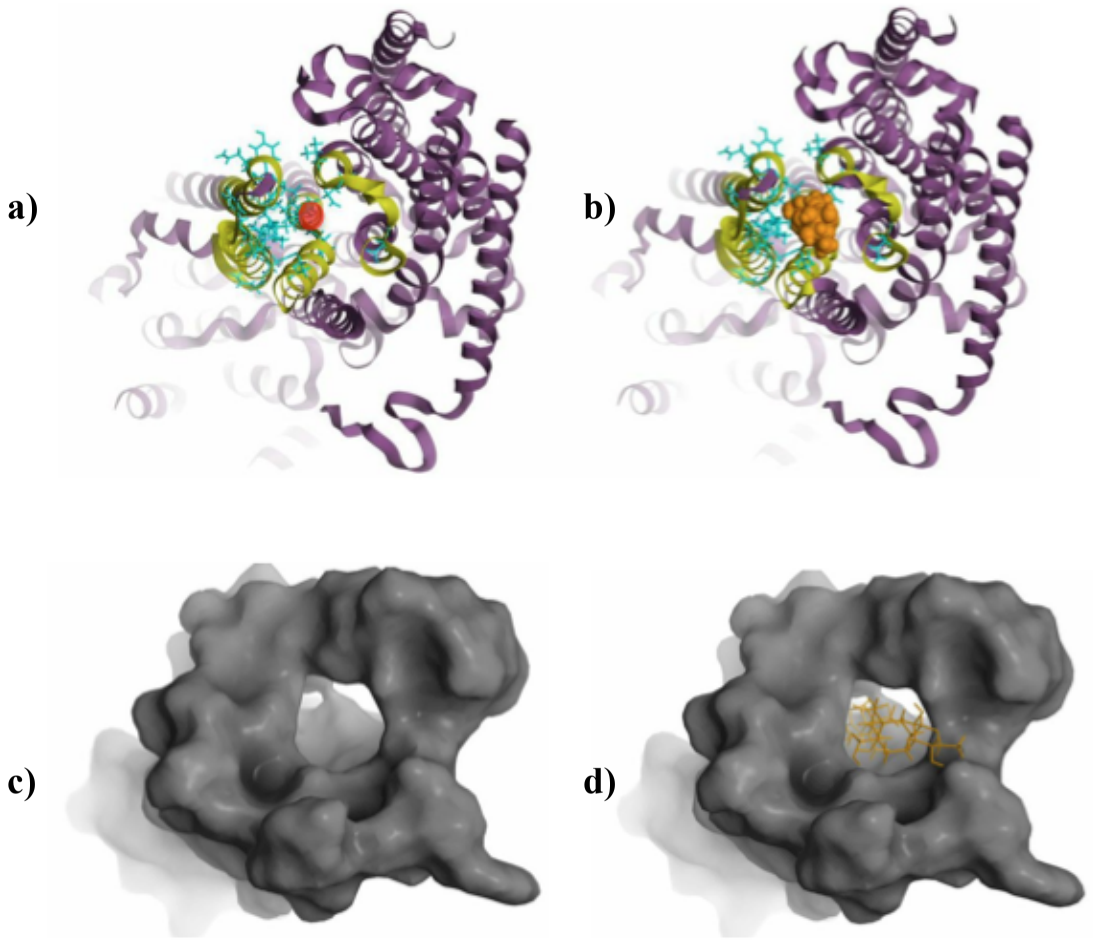

Fig. 2-14. The binding site of ouabain (orange) includes the residues (cyan) that form the cation permeation path in Na^+/K^+ ATPase which traverse the K^+ binding site II (red dot), suggesting than ouabian acts by blocking the ion permeation path. Figure shows the extracellular view of the cation permeation path (a) with bound ouabain (b). Figures c and d show the same view in space-filling representation.

The observations of the structural interactions of ouabain and its analogs with the Na^+/K^+ ATPase are consistent with the observed experimental SAR profile for their inhibition of Na^+/K^+ ATPase ion-transport function and breast cancer cell migration. The docked analogs **2-9** and **2-10** (Figs. 2-15b,c), which are the two most potent analogs (5× and 25× less potent than ouabain, respectively) adapted a similar orientation to the crystal structure of ouabain bound to Na^+/K^+ ATPase (Fig. 2-15a). The concave nonpolar α-surface of ouabain **2-8** (Fig. 2-13 - chemdraw) and analogs **2-9** and **2-10** are stabilized by hydrophobic residues such as I315, F316, F783, and F786 (Fig. 2-15a-c). The hydroxyl groups of the polar β-surface, on the other hand, are stabilized by H-bonding interactions (between C19-OH and the highly conserved C14-OH of cardiac glycosides and N111 and T797 of αM1 and αM6, respectively). The C14-hydroxyl–T797 interaction for analog **2-10**, however, was slightly shifted, and thus the H-bonding angle was less than ideal (Fig. 2-17), possibly due to reduction of lactone ring olefin. This could explain the 25× decrease in potency observed for both the pump and cell migration inhibition. On the other hand, the least potent analog **2-11** (Fig. 2-15d) adapted a different pose in the ion permeation path altogether (Figs. 2-15d and 2-18). Analog **2-11** took up a shallow position and was oriented in the opposite direction with its polar β-surface facing the helices M4 and M5, while the apolar α-surface faced the helices M1, M2, and M6. This orientation does not allow for H-bonding interactions with Q111 and T797 (Figs. 2-15d and 2-18), residues identified by mutagenesis studies[47] to be critical for ouabain's inhibition of Na^+/K^+ ATPase. However, the orientation of the docked analog **2-11** is possibly stabilized by hydrophobic interactions of I315, F316, and F783 with the steroid

rings C and D, and H-bonding interaction of C19-hydroxyl with E117 instead of Q111 (Figs. 2-15d and 2-18).

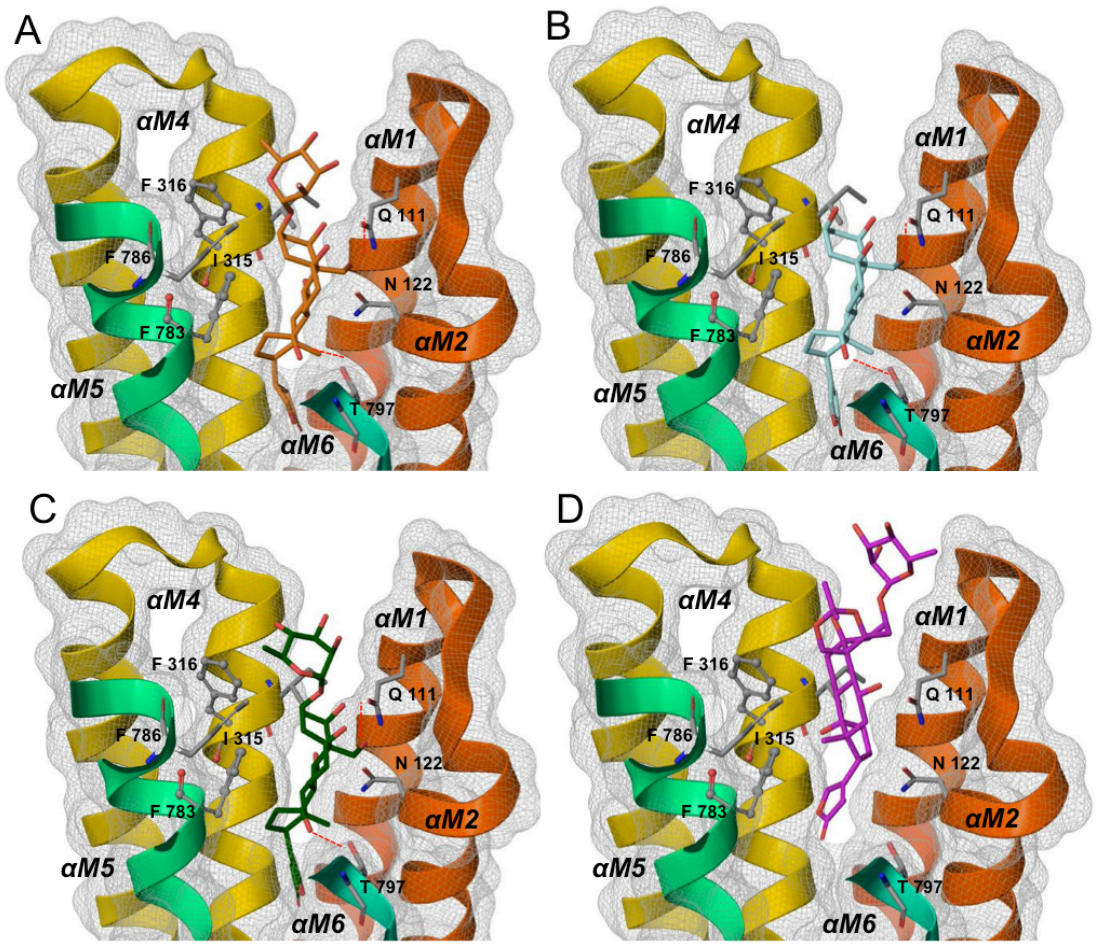

Fig. 2-15. (A) Acual orientation of ouabain in the crystal structure of ouabain-Na^+/K^+ ATPase complex. Orientations of docked analog **2-9** (C), docked analog **2-10** (D), and docked analog **2-11** (E) to cardiac glycoside binding site in the Na^+/K^+ ATPase. Shown are the αM1- αM6 helices that form the binding site for oubain. Also shown are the key residues in the binding site that are responsible for the high-affinity binding of ouabain to the cardiac glycoside binding site

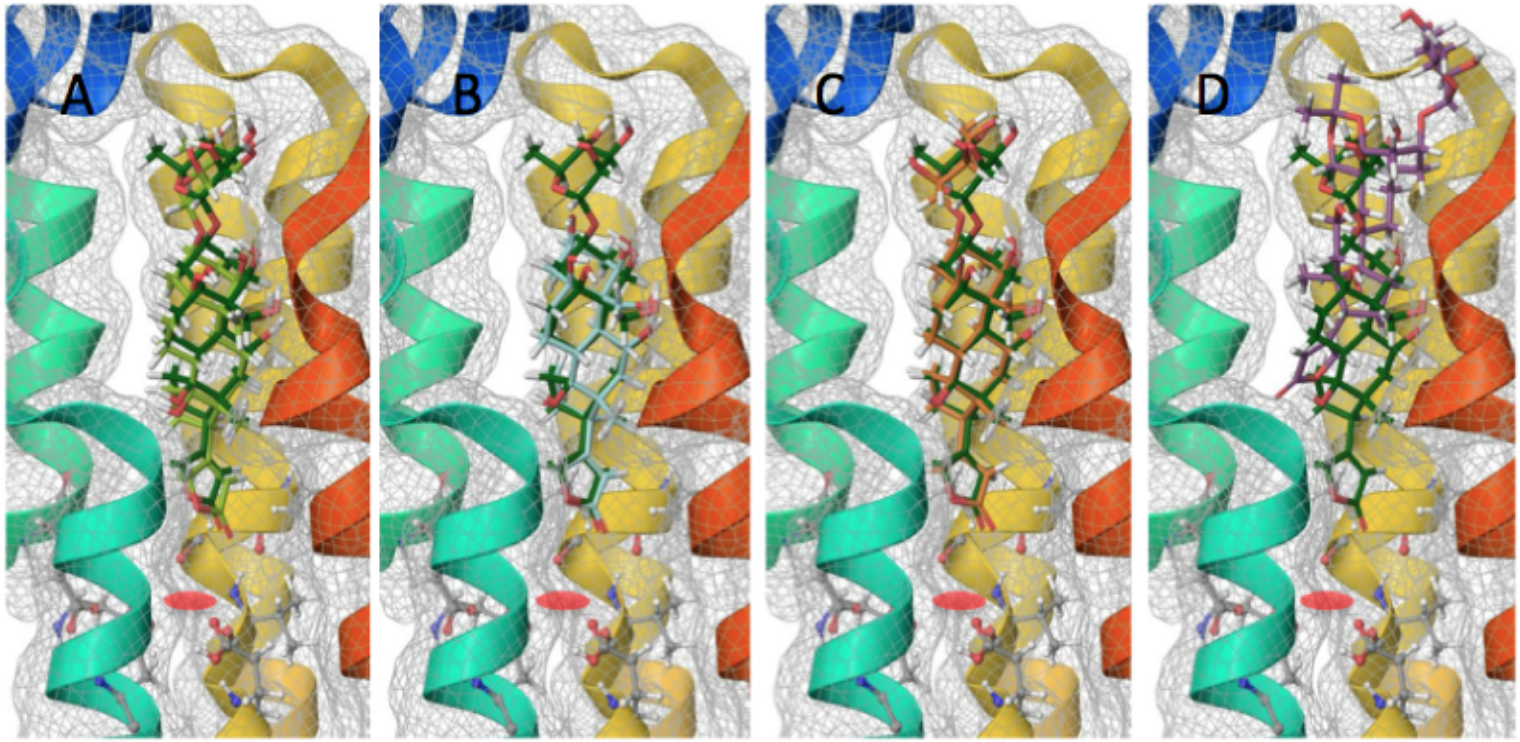

Fig. 2-16. Overlay of crystal structure of ouabain-Na^+/K^+ ATPase complex (ouabain is in orange) with (a) docked ouabain – green, (b) docked analog **2-9** - cyan**,** (c) docked analog **2-10** - orange and (d), docked analog **2-11 –** purple. The orientation of docked ouabain to the cardiac glycoside binding site is very similar to the orientation of ouabian in the actual crystal structure of ouabain-Na^+/K^+ ATPase complex showing that the molecular docking method used closely approximate the actual binding orientation of ouabain.

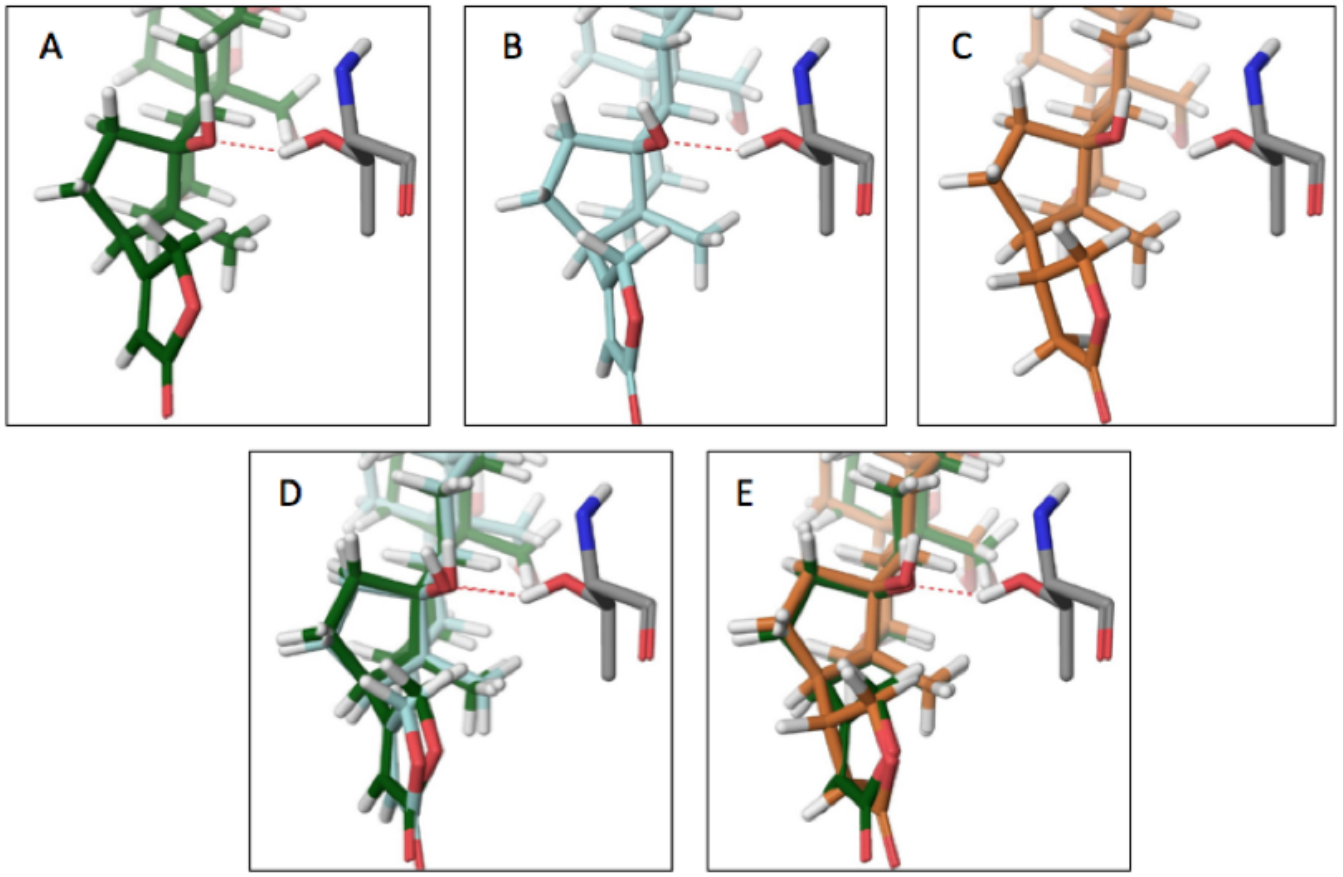

Fig. 2-17. One of the critical interactions for inhibition of Na^+/K^+ ATPase by cardiac glycoside is the interaction between the well conserved T797 and C14-OH of oubain (**A**). This interaction is similarly accessible in (**B**) analog **2-9** but is not accessible in (**C**) analog **2-10,** in which the C14-OH was shifted in an orientation that might have resulted to a less ideal H-bonding angle with T797. This shift in orientation in analog **2-11** could be due to the hydrogenation of the lactone ring olefin of ouabian. The effect of modifications (deglycosylation (analog **2-9**) and hydrogenation (analog **2- 10**)) on cardiac glycoside to this critical hydrogen-bonding interaction might explain the 5x and 25x decrease in potency for analogs **2-9** and **2-10** respectively.

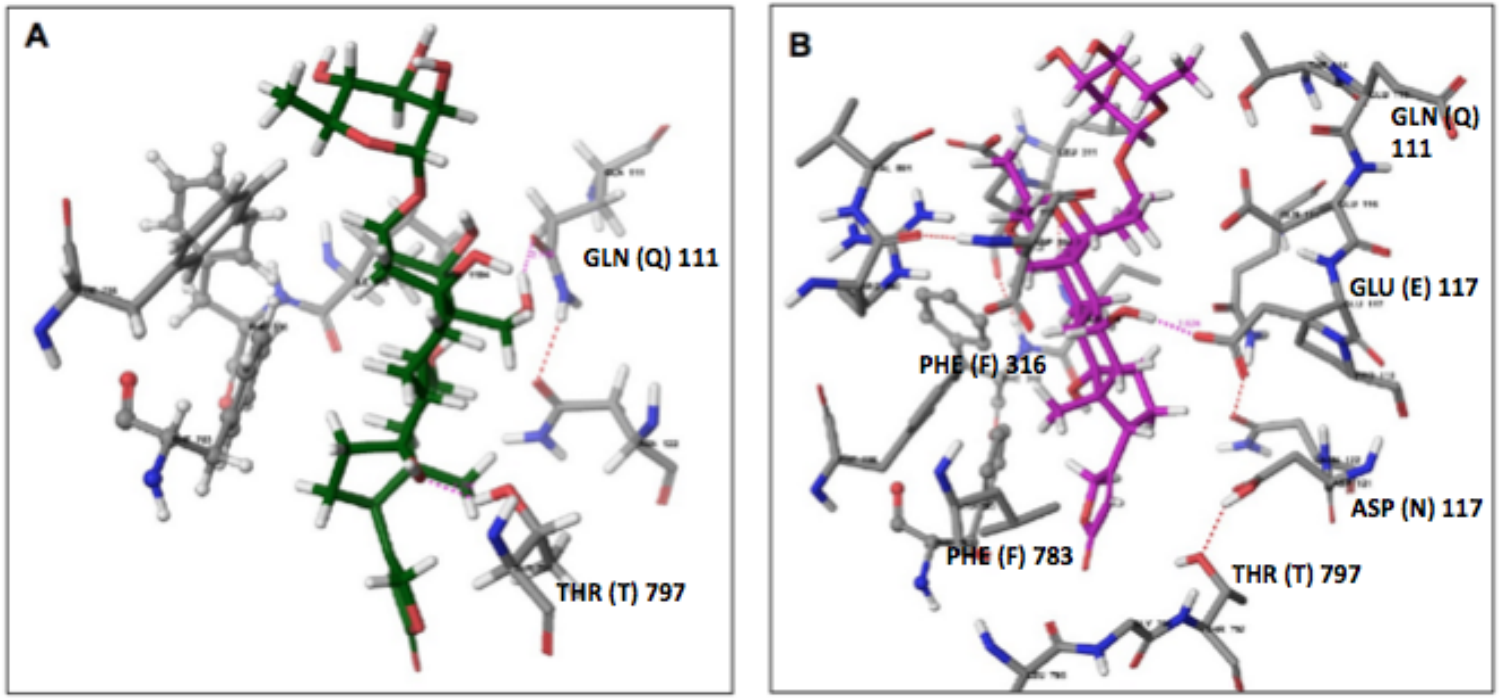

Fig. 2-18. Ouabain (**A**) and analog **2-11** (**B**) hydrophobic and H-bonding interactions with amino acid residues in Na^+/K^+ ATPAse. The orientation of analog **2-11** does not allow for H-bonding interactions with Q111 and T797, residues identified by mutagenesis studies to be critical for ouabain's inhibition of Na^+/K^+ ATPAse. In docked analog **2-11**, T797 is now H-bonding with N111. The high binding energy of analog **2-11** is however possibly stabilized by hydrophobic interactions of I315, F316, F783 with the steroid rings C and D, and H-bonding interaction of C19-hydroxyl with E117 instead of Q111.

2.9.2 Correlative SAR of ouabain and analogs in MDA-MB-231 breast cancer cell migration assay, Na^+/K^+ ATPase assay, binding energy and orientation in Na+/K+ ATPase binding site

The binding energy and RMSD were calculated for the docked compounds to quantify the effect of each structural modification on the ouabain-Na^+/K^+ ATPase interaction. These parameters were then correlated to the experimental results from in vitro Na^+/K^+ ATPase inhibition and breast cancer cell migration assays (Table 2-6). Considering that the docking score is only an approximate measure of true free energies of binding, both the IC_{50} values for inhibition of Na^+/K^+ ATPase and inhibition of cell migration by ouabain and analogs correlate reasonably well with the calculated binding energy (Fig. 2-20) for analogs **2-9** and **2-10**. That is, analogs **2-9** and **2-10** have less negative energy of binding compared with **2-8**, although with similar orders of magnitude, which is consistent with lower potency. A proper orientation relative to the cardiac glycoside binding site seemed to be highly critical to Na^+-pump inhibition (Fig. 2-19). The more negative binding energy calculated for the least potent analog **2-11** probably results from a stable analog **2-11**–Na^+/K^+ ATPase complex (possibly resulting from some hydrophobic and H-bonding interactions discussed earlier) (Fig. 2-18), but the orientation of analog **2-11** to the ion permeation path might not be as effective in blocking ion permeation as that of ouabain. In other words, despite analog **2-11** being more tightly bound, it is noticeably positioned in a region of the binding site much closer to the surface, and therefore less able to stop the permeation of ions deep inside the pocket (Figs. 2-16d and 2-17d). On the other hand, both the IC_{50} values for inhibition of Na^+/K^+

ATPase and inhibition of cell migration by ouabain analogs correlate very well with the RMSD (Fig. 2-19), implying that deviation from ouabain's orientation in the cation permeation of Na^+/K^+ ATPase is directly proportional to the decrease in its inhibitory activity.

Table 2-6. Calculated binding energies and RMSD of ouabain and analogs from molecular docking experiments and the IC50 values for cell migration and Na^+/K^+ ATPase assays

Docked ouabain and analogs	Binding energy (amber score) kcal/mol	RMSD (non-hydrogen atoms)	Na^+/K^+ ATPase IC_{50} (μM)	Cell migration IC_{50} (μM)
2-8	–5420.51	0.0000	0.105	0.173
2-9	–5399.66	0.5807	0.669	0.790
2-10	–5412.08	0.9367	2.6	4.3
2-11	–5584.89	6.5933	12.4	30.9

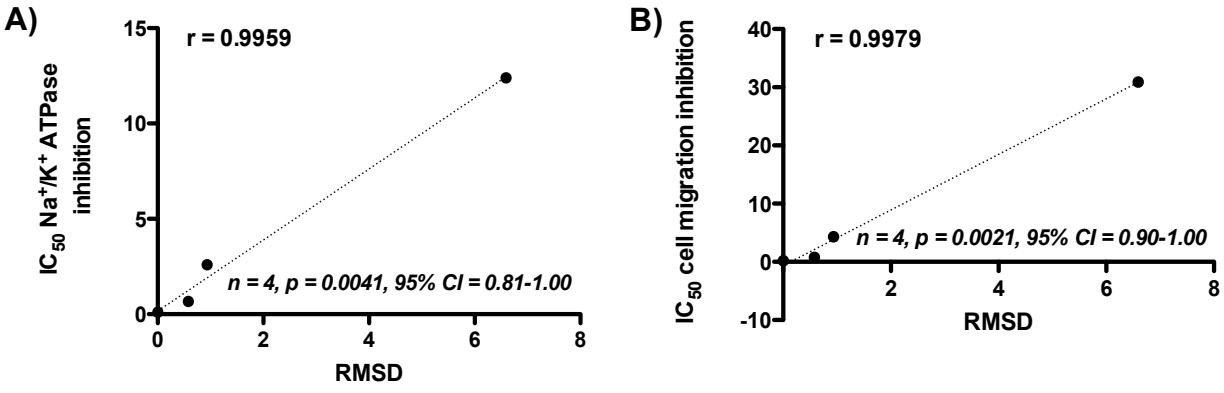

Fig. 2-19. (A) Pearson correlation plot for IC_{50} values of ouabain and analogs in the Na^+/K^+ ATPase assay and the RMSD. (B) Pearson correlation plot for IC_{50} values of ouabain and analogs in the cell migration assay and the RMSD.

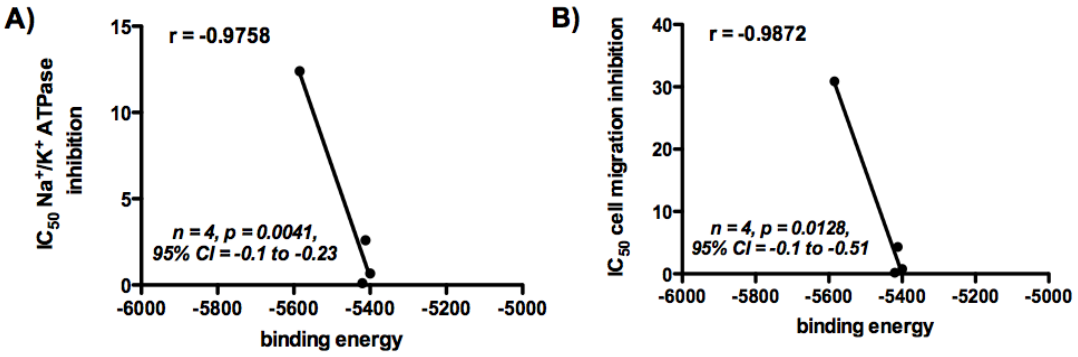

Figure 2-20. (A) Pearson correlation plot for IC_{50} values of ouabain and analogs in the Na^+/K^+ ATPase assay and the RMSD. (B) Pearson correlation plot for IC_{50} values of ouabain and analogs in the cell migration assay and the RMSD.

2.10. Antimigratory activities of other Na^+/K^+ ATPase inhibitors that are not structurally related to cardiac glycosides

To explore whether the inhibition of cell migration results from general inhibition of the Na^+/K^+ ATPase or is specific for cardiac glycosides, the antimigratory effect of other Na^+/K^+ ATPase inhibitors that are structurally distinct from cardiac glycosides was determined. All of the non-cardiac-glycoside Na^+/K^+ ATPase inhibitors tested also inhibited cell migration with varying potencies (Table 2-7). Compound **2-16**, a nonspecific inhibitor of Na^+/K^+ ATPase, is the most potent; however, it was also toxic and its IC_{50} is very close to its minimum lethal concentration, which is likely due to its effect on other cellular targets. The next most potent is compound **2-18**. This Na^+/K^+ ATPase inhibitor is particularly interesting because it was reported that, unlike ouabain, it does not activate the Na^+/K^+ ATPase/Src complex nor does it stimulate the protein kinase

cascades[48] . Compound **2-18** is a useful small molecule probe since it can inhibit only one function (Na^+/K^+ ATPase enzymatic activity) of the pump without activating its receptor function. This allows exploration and differentiation of the functional consequences of the enzymatic versus receptor function of the Na^+/K^+ ATPase. Since **2-18** also inhibits cell migration, the antimigratory activity of cardiac glycosides does not primarily entail activation of the receptor function of Na^+/K^+ ATPase. Furthermore, any of the compounds tested that inhibit Na^+/K^+ ATPase also inhibit MDA-MB-231 breast cancer cell migration. Therefore, the cardiac glycosides do not have a unique antimigratory effect among inhibitors of the Na^+/K^+ ATPase.

Table 2-7. Inhibitory effect of Na^+/K^+ ATPase inhibitors that are structurally different from cardiac glycoside in the Na^+/K^+ ATPase assay and the cell migration assay

Compounds	Literature IC_{50} for inhibition of the Na^+/K^+ ATPase	IC_{50} for inhibition of cell migration	Minimum lethal concentration
(2-16) Na_3VO_4	40nM[49]	5.6 μM	15.6 μM
(2-17) 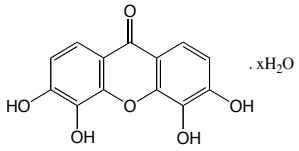	19 μM[50]	34.4 μM	>250 μM
(2-18) 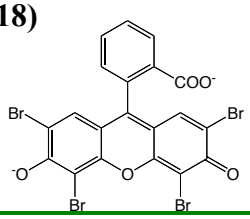	1.5 μM [48]	7.86 μM	>250 μM

2.11. Hypothesis on how cardiac glycoside's inhibition of Na^+/K^+ ATPase leads to inhibition of MDA-MB-231 breast cancer cell migration

The increase in $[Ca^{2+}]_i$, through the activation of the reverse Na^+/Ca^{2+} exchanger resulting from the "classical" inhibition of the ion transport function of the Na^+/K^+ ATPase, might explain the observed inhibitory activity of Na^+/K^+ ATPase inhibitors in MDA-MB-231 breast cancer cell migration. Ca^{2+} signaling is a crucial coordinator of cell migration through various mechanisms. Some of these mechanisms include activation of myosin light chain kinase (MLCK), modulation of nascent focal adhesions, and retraction–adhesion of lamellipodia through local calcium pulses near the leading edge of migrating cells[51]. Consequently, inhibition of key regulators of calcium homeostasis affects cell migration. In the wound-closure assay, thapsigargin, a specific and irreversible inhibitor of sarco/endoplasmic reticulum Ca^{2+} ATPase (SERCA), inhibited the migration of bovine aortic endothelial cells (BAEC). In this migrating BAEC, thapsigargin treatment elicited a rapid increase in $[Ca^{2+}]_i$ due to depletion of Ca^{2+} store sites[52]. Interestingly, through chemical genetic screening using the same wound-closure assay, we found that thapsigargin **2-19** and an analog **2-20** inhibited MDA-MB-231 breast cancer cell migration below their cytotoxic concentration (Fig. 2-21). Besides small molecule inhibition, it was reported that siRNA knockdown of SERCA and other key Ca^{2+} regulators such as plasma membrane calcium ATPase (PMCA) and components of store-operated Ca^{2+} (SOC) influx pathway also altered the basal $[Ca^{2+}]_i$. An inverse correlation between the effect of small molecule and siRNA knockdown to $[Ca^{2+}]_i$ and

cell migration was observed, where an increase in $[Ca^{2+}]_i$ reduced the speed of human umbilical vein endothelial cells (HUVECs) and vice versa[51b]. The aim of the present study is to illustrate the utility of correlative SAR as a strategy to link a specific protein function of a multifunctional protein to an observed cellular phenotype. Although the present study did not explore the effect of Na^+/K^+ ATPase inhibitors in Ca^{2+} signaling, we showed that the antimigratory effect of Na^+/K^+ ATPase inhibitors in MDA-MB-231 breast cancer cell migration is directly related to inhibition of the ion-transport function of the Na^+ pump. It is established that this classical inhibition of Na^+/K^+ ATPase leads to an increase in intracellular $[Ca^{2+}]_I$[33] and thus, it is possible that the observed antimigratory effect of Na^+/K^+ ATPase inhibitors in MDA-MB-231 breast cancer cells might be due to the increase in $[Ca^{2+}]_i$, probably in a similar manner that thapsigargin inhibited the migration of this cell line.

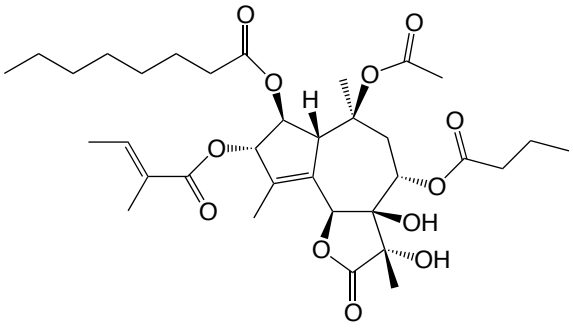

2-19 (tapsigargin)

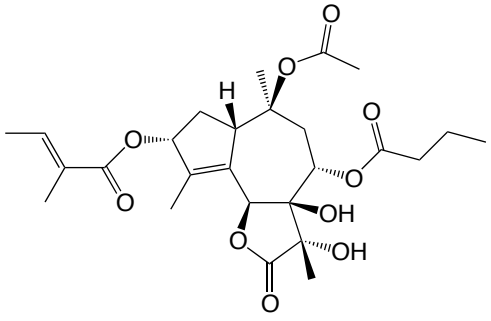

2-20 (tapsogargin analog)

Fig. 2-21. Thapsigargin **2-19** and analog **2-20** were found to inhibit the migration of MDA-MB-231 breast cancer cell from chemical genetic scre ening. Both **2-19** and **2-20** were toxic above 10 μM (Maximum Lethal Concentration) in MDA-MD-231 and have antimigratory activity above 400 nM (Minimum Inhibitory Concentration).

2.12 Conclusion

In this study, correlative SAR of cardiac glycosides and analogs were used to link the ion transport function of Na^+/K^+ ATPase to MDA-MB-231 breast cancer cell migration. Analogs of representative cardiac glycosides ouabian and digitoxin that contain modifications in each part of the tripartite cardiac glycoside were synthesized. The effect of each structural modification on cardiac glycosides to their activities in both inhibition of Na^+/K^+ ATPase (molecular) and cell migration (cellular) provided a distinct pattern (SAR profile). Our results showed that modification on steroid core > modification on lactone ring > modification on sugar in decreasing impact on potency. These SAR profiles correlated in both experimental assays, showing a direct relationship between inhibition of MDA-MB-231 breast cancer cell migration and inhibition of Na^+/K^+ ATPase ion transport function. The interactions of ouabain and analogs to Na^+/K^+ ATPase were also investigated at the atomic level using molecular docking experiments. Their activities in both inhibition of Na^+/K^+ ATPase and cell migration correlated quite well with the degree of similarity in orientation with respect to the known ouabian orientation and reasonably well with binding energy calculations, provided that the analog completely blocks the permeation path. A cardiac glycoside analog may have a higher binding energy to Na^+/K^+ ATPase, but if its orientation does not allow for effective blocking of the ion permeation path, binding of that analog may not result in efficient inhibition.

Based on these results, we conclude that it is the ion-transport function of Na^+/K^+

ATPase that is involved in MDA-MB-231 breast cancer cell migration and not the receptor function. This conclusion is further corroborated by the observed inhibition of breast cancer cell migration by other Na^+/K^+ ATPase inhibitors that are structurally distinct from cardiac glycosides. In particular, a Na^+/K^+ ATPase inhibitor that does not activate Na^+/K^+ ATPase/Src complexes nor the protein kinase cascades still inhibited cell migration, implying that the antimigratory effect of Na^+/K^+ ATPase inhibitors does not involve activation of its receptor function. We speculate that a mechanism in which perturbation of intracellular Na^+ and K^+ and therefore Ca^+ ion concentrations leads to inhibition of breast cancer cell migration. Further studies on how exactly perturbations of ion homeostasis affect the migration of MDA-MB-231 cells could help contribute to understanding the overall mechanism of triple negative breast cancer cell migration. This report also provides an example of how correlative SAR can help establish new relationships between specific biochemical functions and higher-level cellular processes by providing a quantitative way to link the effect of small molecules at the cellular, molecular, and atomic level.

2.13 Experimental

Chemical genetic screening for MDA-MB-231 breast cell migration inhibitors

A previously published high-throughput protocol for screening of inhibitors of epithelial cell sheet migration (ref) was adopted for chemical genetic screening (of around 12,000 natural products and synthetic compounds) of MDA-MB 231 breast cancer cell migration inhibitors. MDA-MB 231 breast cancer cells were plated on 96-well tissue culture plates and cultured at 37 °C and 5 % CO_2 with Dulbecco's Modified Eagle Medium and 10% FBS until confluent. Test compounds from the library (dissolved in DMSO) and DMSO alone (as a control) were added with fresh medium to the confluent cell cultures at an initial screening concentration of 50 μm (1% v/v DMSO/medium). We found that 1% DMSO had no detectable effect on the migration or growth of MDA-MB 231 cells compared to medium alone. After 30 min, the cell monolayers were scraped with a micropipet tip to produce oval-shaped wounds of 0.5–1.0 mm^2 in area. Progress of wound closure was followed by observation on an inverted microscope at 12 h and 24 h. At each time point, wounds were scored as either closed or opened realative to DMSO control to determine possible inhibitory or acceleratory effects of the test compounds on wound closure. Compounds that resulted in wounds that were still open after the wounds for the control DMSO treatments were closed were considered antimigratory. Compounds that were antimigratory at 50 μM were cherry-picked, pooled and screened again at lower concentrations (10 μM, 2 μM, 400 nM and down to 16 nM) to gauge the compound's potency.

Quantitative cell migration assay

Quantitative wound closure assay was performed on compounds that were active at sub micromolar concentrations to evaluate their concentration-response profiles. Similar to the primary wound closure assay, confluent monolayers of MDA-MB-231 breast cancer cells were wounded 30 min after treatment with different concentrations of these compounds or DMSO alone. Instead of a qualitative open or close wound evaluation, the progress of the wound closure was followed quantitatively by taking digital images of the wounds at 3 h, 6 h, 12 h and 24 h post-wounding. Using the NIH ImageJ software (http://rsbweb.nih.gov/ij/), the remaining open area of the wound at each time point was calculated by tracing the wound margin in each images. Microsoft Excel and GraphPad Prism software were used to tabulate and analyze the corresponding data. GraphPad Prism software was used to determine the IC_{50} for inhibition of wound closure from dose-response data and two-tailed Student's *t*-test ($p > 0.05$) was used to statistically determine significant differences. Among the antimigratory compound hits from screening of MDA-MB 231 breast cancer cell migration inhibitors, cardiac glycosides were chosen for further characterization of their mechanism of action in relation to inhibition of MDA-MB 231 breast cancer cell migration. Analogs of reperesentative cardiac glycosides, ouabain and digitoxin were synthesized and analyzed for their effect on MDA-MB 231 breast cancer cell migration using the same quantitative cell migration assay.

Molecular Docking

A model of the complex between oubain bound sodium-potassium transporting ATPase was obtained from the available crystallographic data at the RSCB website (4HYT) and refined using Chimera GUI. Duplicate chains (C, D, and E) and chain G were deleted, as they were not needed in the ligand docking. All residues were protonated based on neutral pH after the assignment of bond orders using the Dock prep tool in Chimera. Histidine tautomers were determined based on the ability to form Hydrogen bonds with the neighboring residues. Ions, solvent molecules, extraneous molecules and substitution codes for the side chains were also deleted.

The protein was assigned Amber force field parameters while antechamber was used to assign the ligand and non-standard residues' parameters. The charge set used for the ligand was AM1-BCC charges; the structure was then minimized and duplicated – one part had the ligand deleted (the receptor) while the other had the protein part deleted (the ligand). The ligand was duplicated again one part was modified and minimized, while the other served as a control.

Docking followed the standard docking procedure in the Dock6 manual. Molecular surface was constructed using the **dms** program inbuilt in UCSF's Chimera using a probe radius of 1.4Å. The spheres were then generated using **sphgen_cc** implemented in Dock6 suite and the X-ray structure (reference) ligand was used to select the hotspot upto 10Å from the position of the heavy atoms of the reference ligand. A site box and the generated

spheres were then prepared using the **showbox** and **showsphere** modules. The grid box enclosing the selected spheres had an extra 5Å added in every dimension. Grids were computed using a grid spacing of 0.3A, distance dielectric of 4 with a combination of contact and energy scores using the Van der Waals parameters of Amber99 force field.

Docking was performed through grid scoring and automated ligand orientation and matching first with a rigid ligand then choosing 10 best poses and redocking while keeping the ligand flexible. To account for receptor flexibility an ensemble docking was attempted with Amber force field parameters and running a molecular dynamics simulation; this instead did not give an improvement in the docking poses but produced fluctuations in the structure. The final rescoring was done on the top most poses from the grid score, using amber score (binding energy)

In vitro Na^+/K^+ ATPase assay

The enzymatic activity of *Na^+/K^+ ATPase (purchased from Sigma as lyophilized powder from porcine cerebral cortex)* was measured by colorimetric quantification of Pi released during ATP hydrolysis. A previously published procedure[47] was adapted with some modifications. The reaction was started by incubating 10µL of Na^+/K^+ ATPase (600 units/mL) with 2.5 µL of KCl/NaCl solution (45mM KCl and 2M NaCl) at 37^{o}C for 30 minutes with either 5 µL DMSO (control) or 5 µL test compounds in 67.5 µL buffer (24mM Tris HCl buffer with 0.68 mM Ethylenediaminetetraacetic acid and 6.0 mM Magnesium chloride, pH 7.8). 5µL of 80mM ATP was then added and the reaction mixture was incubated again at 37^{o}C for 15 minutes. 30 µL of 100% w/v Tricholoroacetic acid was then added to the reaction mixture followed by centrifugation for 3 minutes. 50µL of the supernatant was transferred to a 96-well plate containing 100µL of Taussky-Shorr reagent. The absorbance at 660nm was read after incubation at room temperature for 5 minutes. The concentration of phosphate released in the enzymatic reaction was measured from the absorbance at 660nm using a standard curve. The effect of test compounds on enzymatic activity (percent inhibition) was calculated by taking the ratio of the concentration of liberated phosphate after compound treatment against that of DMSO control. Dose-response (using 9 concentrations starting from 1mM to 15 nM) for Na^+/K^+ ATPase inhibition was obtained for each test compounds for 3 trials with 3 replicates each trial. GraphPad Prism software was used to determine the IC_{50} for Na^+/K^+ ATPase inhibition from dose-response data and two-tailed Student's *t*-test ($p > 0.05$) was used to statistically determine significant differences. GraphPad Prism software was also

used to calculate and generate correlation plots for the inhibitory effect of test compounds on the Na^+/K^+ ATPase enzymatic activity and MDA-MB 231 breast cancer cell migration using Pearson correlation.

2.14. References

1. Horwitz, R.; Webb, D., Cell migration. *Current Biology* **2003,** *13* (19), R756-R759.

2. Montell, D. J., The genetics of cell migration in Drosophila melanogaster and Caenorhabditis elegans development. *Development* **1999,** *126* (14), 3035-3046.

3. Yamaguchi, H.; Wyckoff, J.; Condeelis, J., Cell migration in tumors. *Current Opinion in Cell Biology* **2005,** *17* (5), 559-564.

4. Fenteany, G.; Zhu, S., Small-molecule inhibitors of actin dynamics and cell motility. *Curr Top Med Chem* **2003,** *3* (6), 593-616.

5. Jordan, A.; Hadfield, J. A.; Lawrence, N. J.; McGown, A. T., Tubulin as a target for anticancer drugs: Agents which interact with the mitotic spindle. *Medicinal Research Reviews* **1998,** *18* (4), 259-296.

6. Schiff, P. B.; Horwitz, S. B., Taxol stabilizes microtubules in mouse fibroblast cells. *Proceedings of the National Academy of Sciences of the United States of America* **1980,** *77* (3), 1561-1565.

7. Cooper, J. A., Effects of cytochalasin and phalloidin on actin. *The Journal of Cell Biology* **1987,** *105* (4), 1473-1478.

8. Bubb, M. R.; Senderowicz, A. M.; Sausville, E. A.; Duncan, K. L.; Korn, E. D., Jasplakinolide, a cytotoxic natural product, induces actin polymerization and competitively inhibits the binding of phalloidin to F-actin. *Journal of Biological Chemistry* **1994,** *269* (21), 14869-14871.

9. Kovács, M.; Tóth, J.; Hetényi, C.; Málnási-Csizmadia, A.; Sellers, J. R., Mechanism of Blebbistatin Inhibition of Myosin II. *Journal of Biological Chemistry* **2004,** *279* (34), 35557-35563.

10. Saitoh, M.; Ishikawa, T.; Matsushima, S.; Naka, M.; Hidaka, H., Selective inhibition of catalytic activity of smooth muscle myosin light chain kinase. *Journal of Biological Chemistry* **1987,** *262* (16), 7796-7801.

11. Uehata, M.; Ishizaki, T.; Satoh, H.; Ono, T.; Kawahara, T.; Morishita, T.; Tamakawa, H.; Yamagami, K.; Inui, J.; Maekawa, M.; Narumiya, S., Calcium sensitization of smooth muscle mediated by a Rho-associated protein kinase in hypertension. *Nature* **1997,** *389* (6654), 990-994.

12. Williams, D. E.; Lassota, P.; Andersen, R. J., Motuporamines A–C, Cytotoxic Alkaloids Isolated from the Marine Sponge Xestospongia exigua (Kirkpatrick). *The Journal of Organic Chemistry* **1998,** *63* (14), 4838-4841.

13. Roskelley, C. D.; Williams, D. E.; McHardy, L. M.; Leong, K. G.; Troussard, A.; Karsan, A.; Andersen, R. J.; Dedhar, S.; Roberge, M., Inhibition of Tumor Cell Invasion and Angiogenesis by Motuporamines. *Cancer Research* **2001,** *61* (18), 6788-6794.

14. Vedula, S. R. K.; Ravasio, A.; Lim, C. T.; Ladoux, B., *Collective Cell Migration: A Mechanistic Perspective*. 2013; Vol. 28, p 370-379.

15. Harden, N., Signaling pathways directing the movement and fusion of epithelial sheets: lessons from dorsal closure in Drosophila. *Differentiation* **2002,** *70* (4–5), 181-203.

16. Farooqui, R.; Fenteany, G., Multiple rows of cells behind an epithelial wound edge extend cryptic lamellipodia to collectively drive cell-sheet movement. *Journal of Cell Science* **2005,** *118* (1), 51-63.

17. Mc Henry, K. T.; Ankala, S. V.; Ghosh, A. K.; Fenteany, G., A Non-Antibacterial Oxazolidinone Derivative that Inhibits Epithelial Cell Sheet Migration. *ChemBioChem* **2002,** *3* (11), 1105-1111.

18. Kahsai, A. W.; Zhu, S.; Fenteany, G., G Protein-Coupled Receptor Kinase 2 Activates Radixin, Regulating Membrane Protrusion and Motility in Epithelial Cells. *Biochimica et biophysica acta* **2010,** *1803* (2), 300-310.

19. Zhu, S.; Mc Henry, K. T.; Lane, W. S.; Fenteany, G., A Chemical Inhibitor Reveals the Role of Raf Kinase Inhibitor Protein in Cell Migration. *Chemistry & Biology 12* (9), 981-991.

20. Beshir, A. B.; Argueta, C. E.; Menikarachchi, L. C.; Gascón, J. A.; Fenteany, G., Locostatin Disrupts Association of Raf Kinase Inhibitor Protein With Binding Proteins by Modifying a Conserved Histidine Residue in the Ligand-Binding Pocket. *Forum on immunopathological diseases and therapeutics* **2011,** *2* (1), 47-58.

21. Magpusao, A. N.; Desmond, R. T.; Billings, K. J.; Fenteany, G.; Peczuh, M. W., Synthesis and evaluation of antimigratory and antiproliferative activities of lipid-linked [13]-macro-dilactones. *Bioorganic & medicinal chemistry letters* **2010,** *20* (18), 5472-5476.

22. Strober, W., Trypan Blue Exclusion Test of Cell Viability. In *Current Protocols in Immunology*, John Wiley & Sons, Inc.: 2001.

23. Chavez, K. J.; Garimella, S. V.; Lipkowitz, S., Triple Negative Breast Cancer Cell Lines: One Tool in the Search for Better Treatment of Triple Negative Breast Cancer. *Breast disease* **2010,** *32* (1-2), 35-48.

24. Rahimtoola, S. H.; Tak, T., The use of digitalis in heart failure. *Current Problems in Cardiology* **1996,** *21* (12), 781-853.

25. Mijatovic, T.; Van Quaquebeke, E.; Delest, B.; Debeir, O.; Darro, F.; Kiss, R., Cardiotonic steroids on the road to anti-cancer therapy. *Biochimica et Biophysica Acta (BBA) - Reviews on Cancer* **2007,** *1776* (1), 32-57.

26. Schönfeld, W.; Weiland, J.; Lindig, C.; Masnyk, M.; Kabat, M.; Kurek, A.; Wicha, J.; Repke, K. H., The lead structure in cardiac glycosides is 5 β,14 β-androstane-3 β,14-diol. *Naunyn-Schmiedeberg's Arch. Pharmacol.* **1985,** *329* (4), 414-426.

27. Wang, H.-Y. L.; Rojanasakul, Y.; O'Doherty, G. A., Synthesis and Evaluation of the α-d-/α-l-Rhamnosyl and Amicetosyl Digitoxigenin Oligomers as Antitumor Agents. *ACS Medicinal Chemistry Letters* **2011,** *2* (4), 264-269.

28. Kaplan, J. H., BIOCHEMISTRY OF NA,K-ATPASE. *Annual Review of Biochemistry* **2002,** *71* (1), 511-535.

29. Aperia, A., New roles for an old enzyme: Na,K-ATPase emerges as an interesting drug target. *Journal of Internal Medicine* **2007,** *261* (1), 44-52.

30. Laursen, M.; Yatime, L.; Nissen, P.; Fedosova, N. U., Crystal structure of the high-affinity Na(+),K(+)-ATPase–ouabain complex with Mg(2+) bound in the cation binding site. *Proceedings of the National Academy of Sciences of the United States of America* **2013,** *110* (27), 10958-10963.

31. (a) Haas, M.; Askari, A.; Xie, Z., Involvement of Src and Epidermal Growth Factor Receptor in the Signal Transducing Function of Na+/K+-ATPase. *Journal of Biological Chemistry* **2000**; (b) Haas, M.; Wang, H.; Tian, J.; Xie, Z., Src-mediated Inter-receptor Cross-talk between the Na+/K+-ATPase and the Epidermal Growth Factor Receptor Relays the Signal from Ouabain to Mitogen-activated Protein Kinases. *Journal of Biological Chemistry* **2002,** *277* (21), 18694-18702; (c) Yuan, Z.; Cai, T.; Tian, J.; Ivanov, A. V.; Giovannucci, D. R.; Xie, Z., Na/K-ATPase Tethers Phospholipase C and IP3 Receptor into a Calcium-regulatory Complex. *Molecular Biology of the Cell* **2005,** *16* (9), 4034-4045.

32. Lingrel, J. B., The Physiological Significance of the Cardiotonic Steroid/Ouabain-Binding Site of the Na,K-ATPase. *Annual Review of Physiology* **2010,** *72* (1), 395-412.

33. Dostanic, I.; Schultz, J. E. J.; Lorenz, J. N.; Lingrel, J. B., The α1 Isoform of Na,K-ATPase Regulates Cardiac Contractility and Functionally Interacts and Co-localizes with the Na/Ca Exchanger in Heart. *Journal of Biological Chemistry* **2004,** *279* (52), 54053-54061.

34. Uddin, M. N.; Horvat, D.; Glaser, S. S.; Danchuk, S.; Mitchell, B. M.; Sullivan, D. E.; Morris, C. A.; Puschett, J. B., Marinobufagenin Inhibits Proliferation and Migration of Cytotrophoblast and CHO Cells. *Placenta 29* (3), 266-273.

35. Uddin, M. N.; Horvat, D.; Glaser, S. S.; Mitchell, B. M.; Puschett, J. B., Examination of the Cellular Mechanisms by Which Marinobufagenin Inhibits Cytotrophoblast Function. *Journal of Biological Chemistry* **2008,** *283* (26), 17946-17953.

36. Mijatovic, T.; Roland, I.; Van Quaquebeke, E.; Nilsson, B.; Mathieu, A.; Van Vynckt, F.; Darro, F.; Blanco, G.; Facchini, V.; Kiss, R., The α1 subunit of the sodium pump could represent a novel target to combat non-small cell lung cancers. *The Journal of Pathology* **2007,** *212* (2), 170-179.

37. Lefranc, F.; Mijatovic, T.; Kondo, Y.; Sauvage, S.; Roland, I.; Debeir, O.; Krstic, D.; Vasic, V.; Gailly, P.; Kondo, S.; Blanco, G.; Kiss, R., Targeting the alpha 1 subunit of the sodium pump to combat glioblastoma cells. *Neurosurgery* **2008,** *62* (1), 211-21; discussion 221-2.

38. Jeffery, C. J., Multifunctional proteins: examples of gene sharing. *Annals of Medicine* **2003,** *35* (1), 28-35.

39. (a) Hong, B.-C.; Kim, S.; Kim, T.-S.; Corey, E. J., Synthesis and properties of several isomers of the cardioactive steroid ouabain. *Tetrahedron Letters* **2006,** *47* (16), 2711-2715; (b) Middleton, D. A.; Rankin, S.; Esmann, M.; Watts, A., Structural insights into the binding of cardiac glycosides to the digitalis receptor revealed by solid-state NMR. *Proceedings of the National Academy of Sciences of the United States of America* **2000,** *97* (25), 13602-13607.

40. Larre, I.; Lazaro, A.; Contreras, R. G.; Balda, M. S.; Matter, K.; Flores-Maldonado, C.; Ponce, A.; Flores-Benitez, D.; Rincon-Heredia, R.; Padilla-Benavides, T.; Castillo, A.; Shoshani, L.; Cereijido, M., Ouabain modulates epithelial cell tight junction. *Proceedings of the National Academy of Sciences of the United States of America* **2010,** *107* (25), 11387-11392.

41. Cereijido, M.; Contreras Rg Fau - Shoshani, L.; Shoshani L Fau - Larre, I.; Larre, I., The Na+-K+-ATPase as self-adhesion molecule and hormone receptor. (1522-1563 (Electronic)).

42. Barwe, S. P.; Anilkumar G Fau - Moon, S. Y.; Moon Sy Fau - Zheng, Y.; Zheng Y Fau - Whitelegge, J. P.; Whitelegge Jp Fau - Rajasekaran, S. A.; Rajasekaran Sa Fau - Rajasekaran, A. K.; Rajasekaran, A. K., Novel role for Na,K-ATPase in phosphatidylinositol 3-kinase signaling and suppression of cell motility. (1059-1524 (Print)).

43. Fuerstenwerth, H., On the Differences Between Ouabain and Digitalis Glycosides. *American Journal of Therapeutics* **2014,** *21* (1), 35-42.

44. (a) Ogawa, H.; Shinoda, T.; Cornelius, F.; Toyoshima, C., Crystal structure of the sodium-potassium pump (Na(+),K(+)-ATPase) with bound potassium and ouabain. *Proceedings of the National Academy of Sciences of the United States of America* **2009,** *106* (33), 13742-13747; (b) Yatime, L.; Laursen, M.; Morth, J. P.; Esmann, M.; Nissen, P.; Fedosova, N. U., Structural insights into the high affinity binding of cardiotonic steroids to the Na+,K+-ATPase. *Journal of Structural Biology* **2011,** *174* (2), 296-306; (c) Sandtner, W.; Egwolf, B.; Khalili-Araghi, F.; Sánchez-Rodríguez, J. E.; Roux, B.; Bezanilla, F.; Holmgren, M., Ouabain Binding Site in a Functioning Na+/K+ ATPase. *Journal of Biological Chemistry* **2011,** *286* (44), 38177-38183.

45. Takeuchi, A.; Reyes N Fau - Artigas, P.; Artigas P Fau - Gadsby, D. C.; Gadsby, D. C., The ion pathway through the opened Na(+),K(+)-ATPase pump. (1476-4687 (Electronic)).

46. Lingrel, J. B.; Croyle Ml Fau - Woo, A. L.; Woo Al Fau - Arguello, J. M.; Arguello, J. M., Ligand binding sites of Na,K-ATPase. (0302-2994 (Print)).

47. (a) Feng, J.; Lingrel, J. B., Analysis of amino acid residues in the H5-H6 transmembrane and extracellular domains of Na,K-ATPase alpha subunit identifies threonine 797 as a determinant of ouabain sensitivity. (0006-2960 (Print)); (b) Qiu, L. Y.; Koenderink Jb Fau - Swarts, H. G. P.; Swarts Hg Fau - Willems, P. H. G. M.; Willems Ph Fau - De Pont, J. J. H. H. M.; De Pont, J. J., Phe783, Thr797, and Asp804 in transmembrane hairpin M5-M6 of Na+,K+-ATPase play a key role in ouabain binding. (0021-9258 (Print)).

48. Zhang, Z.; Li Z Fau - Tian, J.; Tian J Fau - Jiang, W.; Jiang W Fau - Wang, Y.; Wang Y Fau - Zhang, X.; Zhang X Fau - Li, Z.; Li Z Fau - You, Q.; You Q Fau - Shapiro, J. I.; Shapiro Ji Fau - Si, S.; Si S Fau - Xie, Z.; Xie, Z., Identification of hydroxyxanthones as Na/K-ATPase ligands. (1521-0111 (Electronic)).

49. Cantley Lc Jr Fau - Josephson, L.; Josephson L Fau - Warner, R.; Warner R Fau - Yanagisawa, M.; Yanagisawa M Fau - Lechene, C.; Lechene C Fau - Guidotti, G.; Guidotti, G., Vanadate is a potent (Na,K)-ATPase inhibitor found in ATP derived from muscle. (0021-9258 (Print)).

50. Ogan, J. T.; Reifenberger Ms Fau - Milanick, M. A.; Milanick Ma Fau - Gatto, C.; Gatto, C., Kinetic characterization of Na,K-ATPase inhibition by Eosin. (1079-9796 (Print)).

51. (a) Giannone, G.; Dubin-Thaler Bj Fau - Rossier, O.; Rossier O Fau - Cai, Y.; Cai Y Fau - Chaga, O.; Chaga O Fau - Jiang, G.; Jiang G Fau - Beaver, W.; Beaver W Fau - Dobereiner, H.-G.; Dobereiner Hg Fau - Freund, Y.; Freund Y Fau - Borisy, G.; Borisy G

Fau - Sheetz, M. P.; Sheetz, M. P., Lamellipodial actin mechanically links myosin activity with adhesion-site formation. (0092-8674 (Print)); (b) Tsai, F. C.; Meyer, T., Ca2+ pulses control local cycles of lamellipodia retraction and adhesion along the front of migrating cells. (1879-0445 (Electronic)).

52. Kimura, C.; Oike M Fau - Koyama, T.; Koyama T Fau - Ito, Y.; Ito, Y., Alterations of Ca2+ mobilizing properties in migrating endothelial cells. (0363-6135 (Print)).

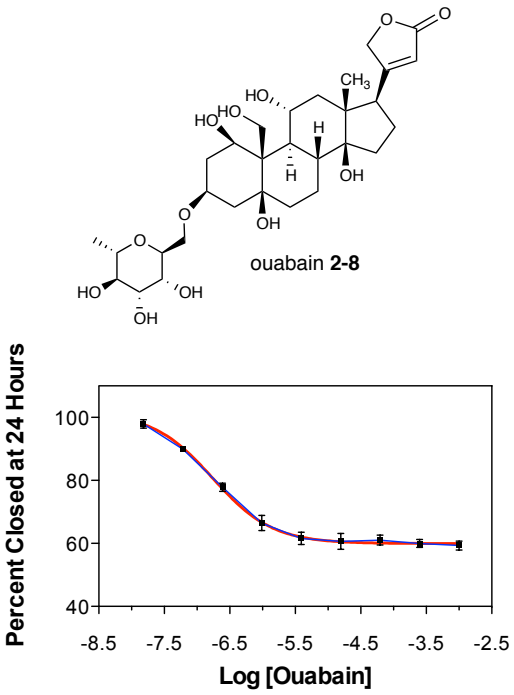

Sigmoidal dose-response (variable slope)	
Best-fit values	
Bottom	59.96
Top	101.5
LogEC50	-6.762
HillSlope	-0.9504
EC50	1.732e-007
Std. Error	
Bottom	0.8770
Top	3.693
LogEC50	0.1194
HillSlope	0.1846
95% Confidence Intervals	
Bottom	58.21 to 61.71
Top	94.16 to 108.9
LogEC50	-7.000 to -6.523
HillSlope	-1.319 to -0.5824
EC50	1.001e-007 to 2.996e-007
Goodness of Fit	
Degrees of Freedom	77
R^2	0.8889
Absolute Sum of Squares	1909
Sy.x	4.980
Number of points Analyzed	81

Figure A-1. Dose-response curve for ouabain **2-8** effect in MDA-MB-231 wound closure. IC_{50} values were determined by nonlinear regression analysis with GraphPad prism software. It was calculated for inhibition of wound closure at 24 h post-wounding with normalization to parallel controls using at least 5 different subtoxic concentrations in concentration-response experiments. The calculated IC50 value for inhibition of wound closure at 24 h by ouabain **2-8** is 173 nM.

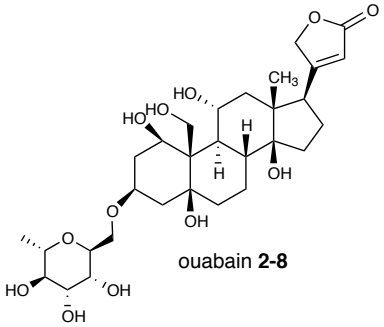

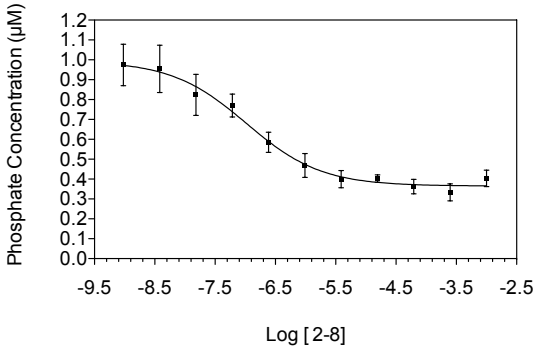

Sigmoidal dose-response (variable slope)	
Best-fit values	
Bottom	0.3652
Top	0.9949
LogEC50	-6.980
HillSlope	-0.6997
EC50	1.048e-007
Std. Error	
Bottom	0.03546
Top	0.07727
LogEC50	0.2576
HillSlope	0.2565
95% Confidence Intervals	
Bottom	0.2926 to 0.4377
Top	0.8369 to 1.153
LogEC50	-7.506 to -6.453
HillSlope	-1.224 to -0.1751
EC50	3.116e-008 to 3.525e-007
Goodness of Fit	
Degrees of Freedom	29
R^2	0.8444
Absolute Sum of Squares	0.3316
Sy.x	0.1069
Number of points Analyzed	33

Figure A-2. Dose-response curve for ouabain **2-8** effect in *in vitro* Na^+/K^+ ATPase inhibition. IC_{50} values were determined by nonlinear regression analysis with GraphPad prism software. It was calculated with normalization to DMSO control. The calculated IC_{50} value for inhibition of the Na^+/K^+ ATPase activity by ouabain **2-8** is 105 nM.

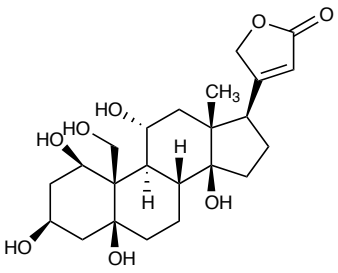

deglycosylated ouabain **2-9**

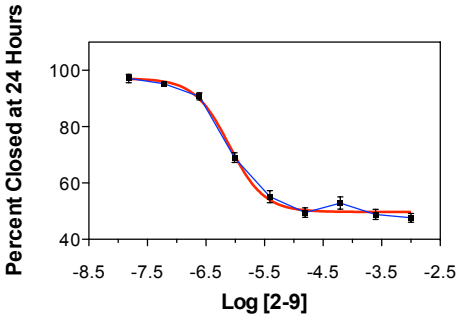

Sigmoidal dose-response (variable slope)	
Best-fit values	
Bottom	49.73
Top	97.11
LogEC50	-6.103
HillSlope	-1.453
EC50	7.896e-007
Std. Error	
Bottom	0.8659
Top	1.388
LogEC50	0.04675
HillSlope	0.2078
95% Confidence Intervals	
Bottom	48.00 to 51.46
Top	94.34 to 99.87
LogEC50	-6.196 to -6.009
HillSlope	-1.868 to -1.039
EC50	6.371e-007 to 9.787e-007
Goodness of Fit	
Degrees of Freedom	77
R^2	0.9429
Absolute Sum of Squares	1964
Sy.x	5.051
Number of points	
Analyzed	81

Figure A-3. Dose-response curve for ouabain **2-9** effect in MDA-MB-231 wound closure. IC_{50} values were determined by nonlinear regression analysis with GraphPad prism software. It was calculated for inhibition of wound closure at 24 h post-wounding with normalization to parallel controls using at least 5 different subtoxic concentrations in concentration-response experiments. The calculated IC50 value for inhibition of wound closure at 24 h by **2-9** is 790 nM.

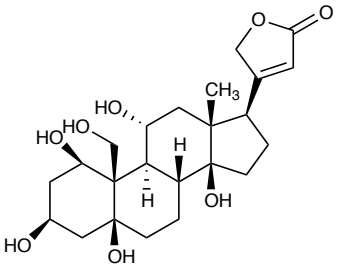

deglycosylated oubain **2-9**

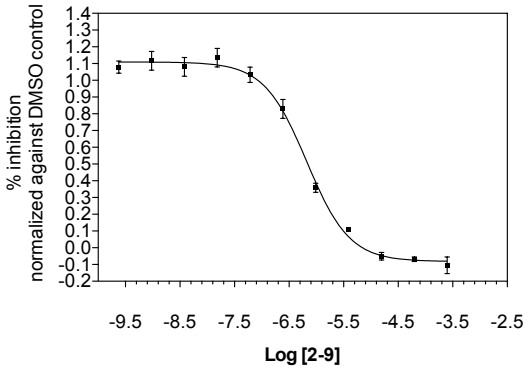

Sigmoidal dose-response (variable slope)	
Best-fit values	
Bottom	-0.08177
Top	1.109
LogEC50	-6.175
HillSlope	-1.109
EC50	6.687e-007
Std. Error	
Bottom	0.02719
Top	0.02157
LogEC50	0.05251
HillSlope	0.1310
95% Confidence Intervals	
Bottom	-0.1358 to -0.02771
Top	1.067 to 1.152
LogEC50	-6.279 to -6.070
HillSlope	-1.370 to -0.8489
EC50	5.258e-007 to 8.504e-007
Goodness of Fit	
Degrees of Freedom	95
R^2	0.9459
Absolute Sum of Squares	1.499
Sy.x	0.1256
Number of points Analyzed	99

Figure A-4. Dose-response curve for ouabain **2-9** effect in *in vitro* Na^+/K^+ ATPase inhibition. IC_{50} values were determined by nonlinear regression analysis with GraphPad prism software. It was calculated with normalization to DMSO control. The calculated IC_{50} value for inhibition of the Na^+/K^+ ATPase activity by **2-9** is 669 nM.

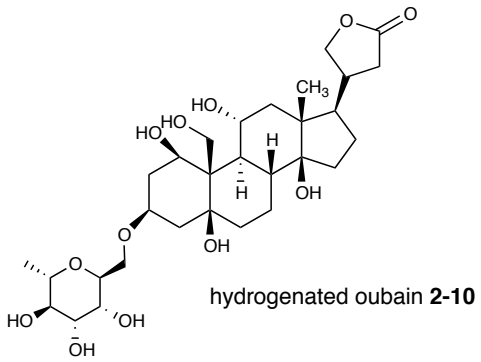

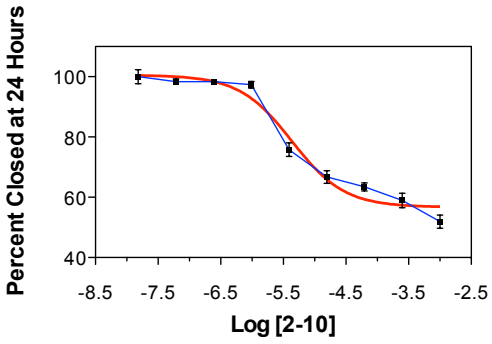

Sigmoidal dose-response (variable slope)	
Best-fit values	
Bottom	56.73
Top	100.5
LogEC50	-5.363
HillSlope	-1.034
EC50	4.333e-006
Std. Error	
Bottom	1.513
Top	1.459
LogEC50	0.07826
HillSlope	0.1766
95% Confidence Intervals	
Bottom	53.71 to 59.74
Top	97.62 to 103.4
LogEC50	-5.519 to -5.207
HillSlope	-1.386 to -0.6814
EC50	3.025e-006 to 6.207e-006
Goodness of Fit	
Degrees of Freedom	77
R^2	0.9028
Absolute Sum of Squares	2888
Sy.x	6.124
Number of points Analyzed	81

Figure A-5. Dose-response curve for ouabain **2-10** effect in MDA-MB-231 wound closure. IC_{50} values were determined by nonlinear regression analysis with GraphPad prism software. It was calculated for inhibition of wound closure at 24 h post-wounding with normalization to parallel controls using at least 5 different subtoxic concentrations in concentration-response experiments. The calculated IC50 value for inhibition of wound closure at 24 h by **2-10** is 4.33 μM.

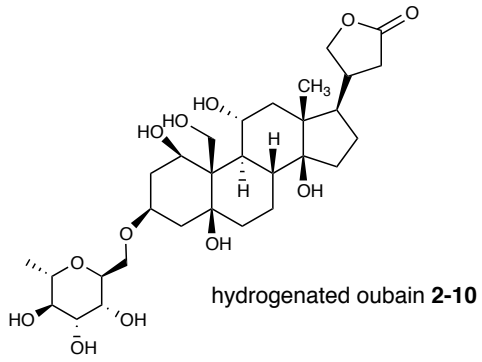

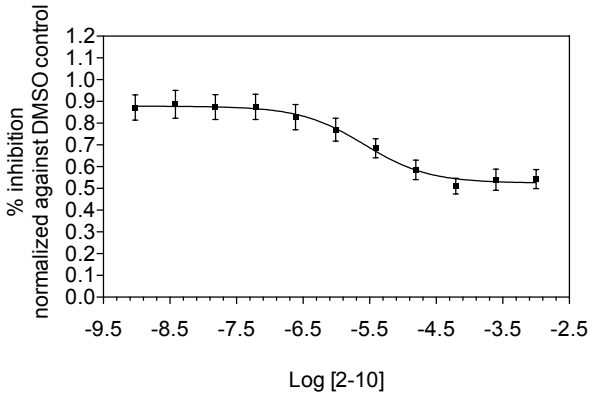

Sigmoidal dose-response (variable slope)	
Best-fit values	
Bottom	0.5248
Top	0.8781
LogEC50	-5.579
HillSlope	-0.8981
EC50	2.638e-006
Std. Error	
Bottom	0.03701
Top	0.02827
LogEC50	0.2544
HillSlope	0.4251
95% Confidence Intervals	
Bottom	0.4512 to 0.5984
Top	0.8219 to 0.9343
LogEC50	-6.084 to -5.073
HillSlope	-1.743 to -0.05282
EC50	8.232e-007 to 8.456e-006
Goodness of Fit	
Degrees of Freedom	95
R^2	0.4974
Absolute Sum of Squares	2.160
Sy.x	0.1508
Number of points	
Analyzed	99

Figure A-6. Dose-response curve for ouabain **2-10** effect in *in vitro* Na^+/K^+ ATPase inhibition. IC_{50} values were determined by nonlinear regression analysis with GraphPad prism software. It was calculated with normalization to DMSO control. The calculated IC_{50} value for inhibition of the Na^+/K^+ ATPase activity by **2-10** is 2.6 μM.

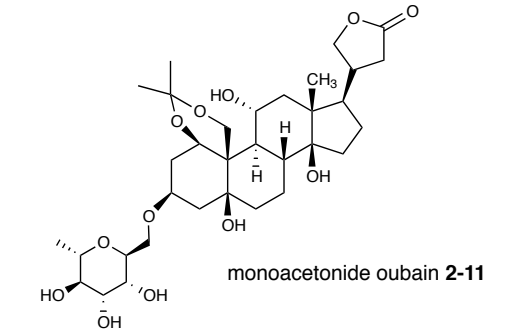

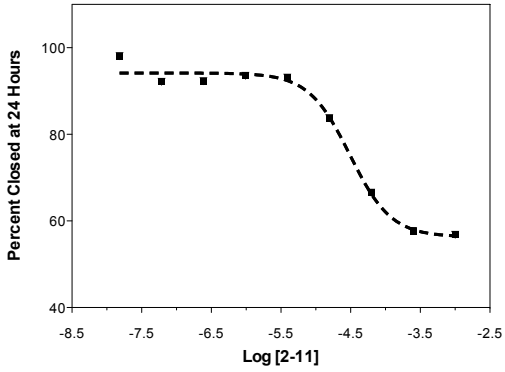

Sigmoidal dose-response (variable slope)	
Best-fit values	
Bottom	56.33
Top	94.16
LogEC50	-4.510
HillSlope	-1.464
EC50	3.093e-005
Std. Error	
Bottom	1.961
Top	1.070
LogEC50	0.07899
HillSlope	0.3143
95% Confidence Intervals	
Bottom	51.28 to 61.37
Top	91.41 to 96.91
LogEC50	-4.713 to -4.307
HillSlope	-2.272 to -0.6554
EC50	1.938e-005 to 4.937e-005
Goodness of Fit	
Degrees of Freedom	5
R^2	0.9891
Absolute Sum of Squares	23.74
Sy.x	2.179
Number of points Analyzed	9

Figure A-7. Dose-response curve for **2-11** effect in MDA-MB-231 wound closure. IC_{50} values were determined by nonlinear regression analysis with GraphPad prism software. It was calculated for inhibition of wound closure at 24 h post-wounding with normalization to parallel controls using at least 5 different subtoxic concentrations in concentration-response experiments. The calculated IC50 value for inhibition of wound closure at 24 h by **2-11** is 30.9 μM.

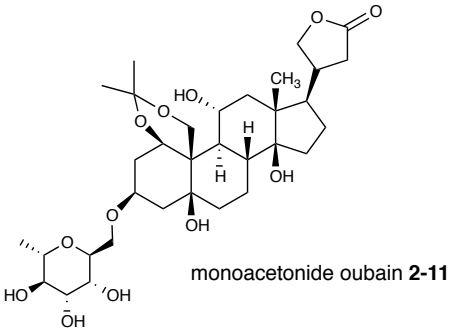

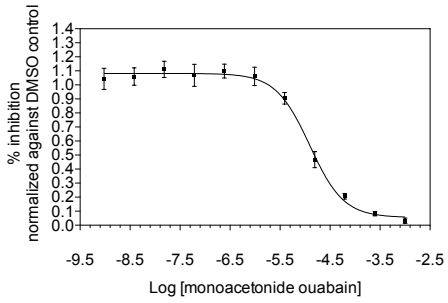

Sigmoidal dose-response (variable slope)	
Best-fit values	
Bottom	0.05538
Top	1.082
LogEC50	-4.905
HillSlope	-1.282
EC50	1.244e-005
Std. Error	
Bottom	0.04106
Top	0.02301
LogEC50	0.07105
HillSlope	0.2375
95% Confidence Intervals	
Bottom	-0.02626 to 0.1370
Top	1.036 to 1.128
LogEC50	-5.047 to -4.764
HillSlope	-1.755 to -0.8099
EC50	8.982e-006 to 1.722e-005
Goodness of Fit	
Degrees of Freedom	95
R^2	0.8842
Absolute Sum of Squares	2.339
Sy.x	0.1569
Number of points Analyzed	99

Figure A-8. Dose-response curve for ouabain **2-11** effect in *in vitro* Na^+/K^+ ATPase inhibition. IC_{50} values were determined by nonlinear regression analysis with GraphPad prism software. It was calculated with normalization to DMSO control. The calculated IC_{50} value for inhibition of the Na^+/K^+ ATPase activity by **2-11** is 12.4 μM.

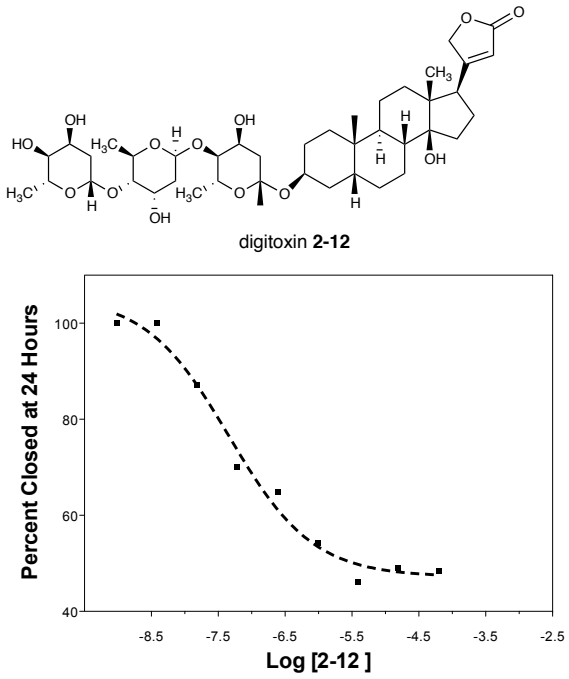

Sigmoidal dose-response (variable slope)	
Best-fit values	
Bottom	47.24
Top	105.7
LogEC50	-7.336
HillSlope	-0.6929
EC50	4.609e-008
Std. Error	
Bottom	3.239
Top	7.263
LogEC50	0.2251
HillSlope	0.2258
95% Confidence Intervals	
Bottom	40.78 to 53.70
Top	91.21 to 120.2
LogEC50	-7.785 to -6.887
HillSlope	-1.143 to -0.2426
EC50	1.639e-008 to 1.296e-007
Goodness of Fit	
Degrees of Freedom	77
R^2	0.7394
Absolute Sum of Squares	11959
Sy.x	12.46
Number of points Analyzed	81

Figure A-9. Dose-response curve for **2-12** effect in MDA-MB-231 wound closure. IC_{50} values were determined by nonlinear regression analysis with GraphPad prism software. It was calculated for inhibition of wound closure at 24 h post-wounding with normalization to parallel controls using at least 5 different subtoxic concentrations in concentration-response experiments. The calculated IC50 value for inhibition of wound closure at 24 h by **2-12** is 46 nM.

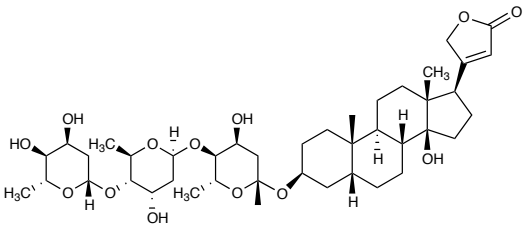

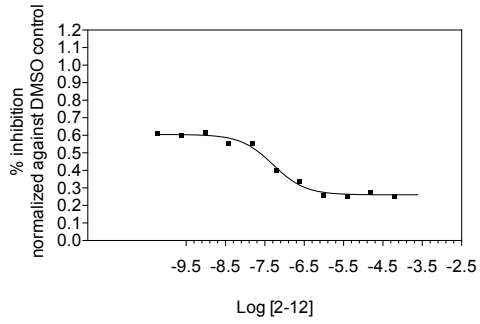

Sigmoidal dose-response (variable slope)	
Best-fit values	
Bottom	0.2608
Top	0.6049
LogEC50	-7.290
HillSlope	-1.061
EC50	5.129e-008
Std. Error	
Bottom	0.01075
Top	0.01286
LogEC50	0.09477
HillSlope	0.2168
95% Confidence Intervals	
Bottom	0.2361 to 0.2856
Top	0.5752 to 0.6345
LogEC50	-7.508 to -7.071
HillSlope	-1.560 to -0.5606
EC50	3.101e-008 to 8.484e-008
Goodness of Fit	
Degrees of Freedom	8
R^2	0.9863
Absolute Sum of Squares	0.003758
Sy.x	0.02167
Number of points Analyzed	12

Figure A-10. Dose-response curve for digitoxin **2-12** effect in *in vitro* Na^+/K^+ ATPase inhibition. IC_{50} values were determined by nonlinear regression analysis with GraphPad prism software. It was calculated with normalization to DMSO control. The calculated IC_{50} value for inhibition of the Na^+/K^+ ATPase activity by **2-12** is 5.13 nM.

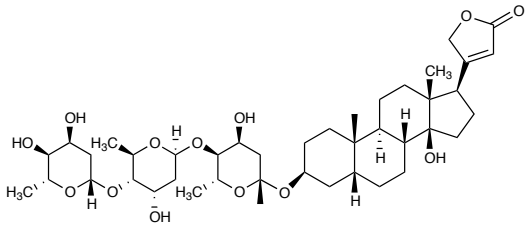

digitoxigenin **2-13**

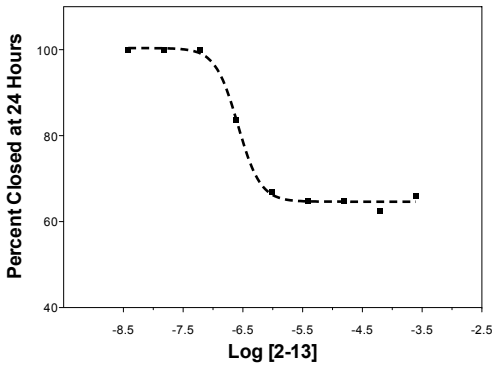

Sigmoidal dose-response (variable slope)	
Best-fit values	
Bottom	64.65
Top	100.4
LogEC50	-6.583
HillSlope	-2.298
EC50	2.614e-007
Std. Error	
Bottom	1.451
Top	1.910
LogEC50	0.06828
HillSlope	1.250
95% Confidence Intervals	
Bottom	61.76 to 67.55
Top	96.58 to 104.2
LogEC50	-6.719 to -6.446
HillSlope	-4.792 to 0.1947
EC50	1.911e-007 to 3.577e-007
Goodness of Fit	
Degrees of Freedom	77
R^2	0.7800
Absolute Sum of Squares	5901
Sy.x	8.754
Number of points Analyzed	81

Figure A-11. Dose-response curve for **2-13** effect in MDA-MB-231 wound closure. IC_{50} values were determined by nonlinear regression analysis with GraphPad prism software. It was calculated for inhibition of wound closure at 24 h post-wounding with normalization to parallel controls using at least 5 different subtoxic concentrations in concentration-response experiments. The calculated IC_{50} value for inhibition of wound closure at 24 h by **2-13** is 261 nM.

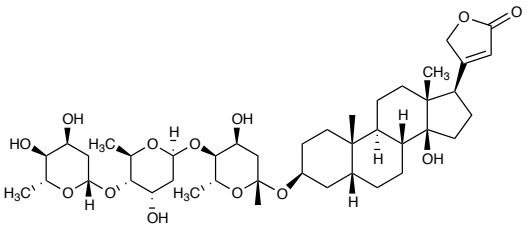

digitoxigenin **2-13**

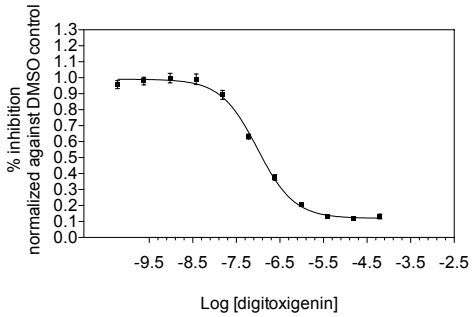

Sigmoidal dose-response (variable slope)	
Best-fit values	
Bottom	0.1201
Top	0.9911
LogEC50	-7.014
HillSlope	-1.031
EC50	9.692e-008
Std. Error	
Bottom	0.01594
Top	0.01240
LogEC50	0.04118
HillSlope	0.08961
95% Confidence Intervals	
Bottom	0.08737 to 0.1528
Top	0.9657 to 1.017
LogEC50	-7.098 to -6.929
HillSlope	-1.215 to -0.8472
EC50	7.978e-008 to 1.177e-007
Goodness of Fit	
Degrees of Freedom	27
R^2	0.9906
Absolute Sum of Squares	0.03968
Sy.x	0.03833
Number of points Analyzed	31

Figure A-12. Dose-response curve for digitoxin **2-13** effect in *in vitro* Na^+/K^+ ATPase inhibition. IC_{50} values were determined by nonlinear regression analysis with GraphPad prism software. It was calculated with normalization to DMSO control. The calculated IC_{50} value for inhibition of the Na^+/K^+ ATPase activity by **2-13** is 97 nM.

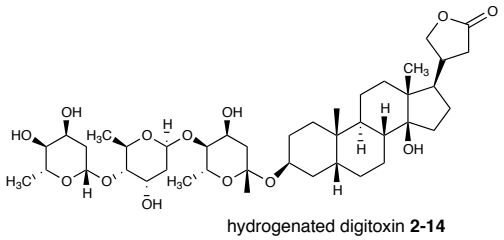

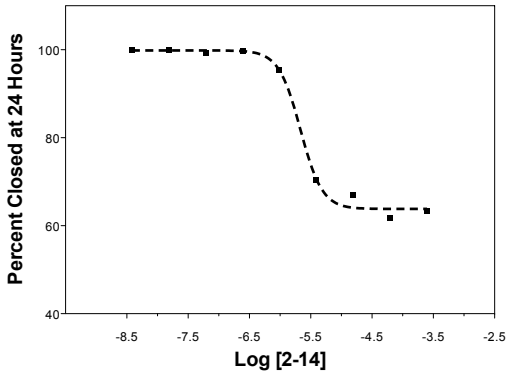

Sigmoidal dose-response (variable slope)	
Best-fit values	
Bottom	63.81
Top	99.85
LogEC50	-5.667
HillSlope	-2.442
EC50	2.154e-006
Std. Error	
Bottom	1.657
Top	1.420
LogEC50	0.08475
HillSlope	0.6761
95% Confidence Intervals	
Bottom	60.51 to 67.12
Top	97.02 to 102.7
LogEC50	-5.836 to -5.498
HillSlope	-3.791 to -1.094
EC50	1.460e-006 to 3.179e-006
Goodness of Fit	
Degrees of Freedom	77
R^2	0.8084
Absolute Sum of Squares	5368
Sy.x	8.349
Number of points Analyzed	81

Figure A-13. Dose-response curve for **2-14** effect in MDA-MB-231 wound closure. IC_{50} values were determined by nonlinear regression analysis with GraphPad prism software. It was calculated for inhibition of wound closure at 24 h post-wounding with normalization to parallel controls using at least 5 different subtoxic concentrations in concentration-response experiments. The calculated IC_{50} value for inhibition of wound closure at 24 h by **2-14** is 2.15 μM.

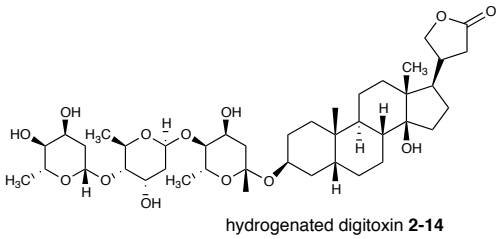

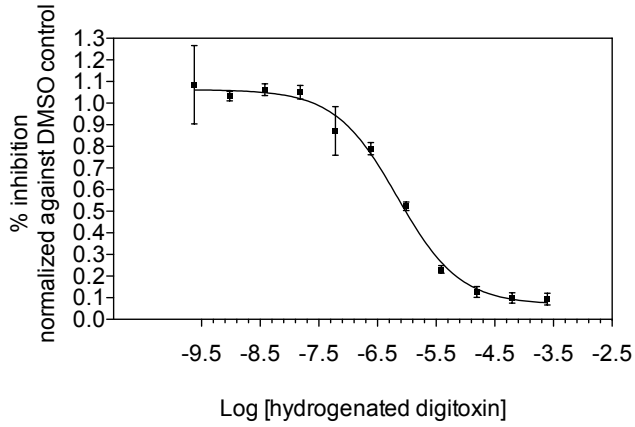

Sigmoidal dose-response (variable slope)	
Best-fit values	
Bottom	0.06876
Top	1.063
LogEC50	-6.161
HillSlope	-0.8172
EC50	6.907e-007
Std. Error	
Bottom	0.04976
Top	0.03670
LogEC50	0.1228
HillSlope	0.1722
95% Confidence Intervals	
Bottom	-0.03300 to 0.1705
Top	0.9877 to 1.138
LogEC50	-6.412 to -5.910
HillSlope	-1.169 to -0.4650
EC50	3.874e-007 to 1.231e-006
Goodness of Fit	
Degrees of Freedom	29
R^2	0.9412
Absolute Sum of Squares	0.3375
Sy.x	0.1079
Number of points Analyzed	33

Figure A-14. Dose-response curve for digitoxin **2-14** effect in *in vitro* Na^+/K^+ ATPase inhibition. IC_{50} values were determined by nonlinear regression analysis with GraphPad prism software. It was calculated with normalization to DMSO control. The calculated IC_{50} value for inhibition of the Na^+/K^+ ATPase activity by **2-14** is 691 nM.

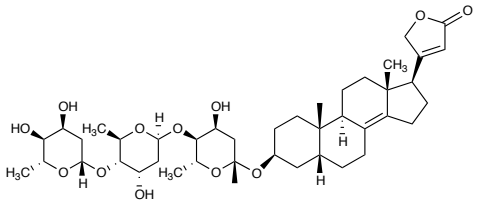

dehydrated digitoxin **2-15a**

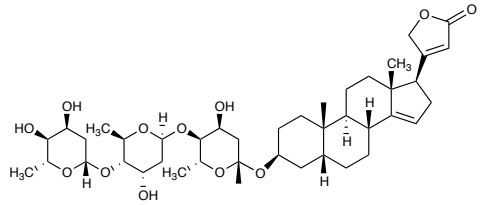

dehydrated digitoxin **2-15b**

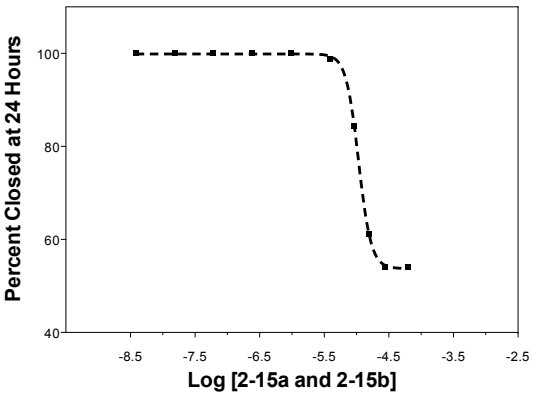

Sigmoidal dose-response (variable slope)	
Best-fit values	
Bottom	53.76
Top	99.88
LogEC50	-4.968
HillSlope	-4.461
EC50	1.077e-005
Std. Error	
Bottom	0.8194
Top	0.4336
LogEC50	0.01024
HillSlope	0.4238
95% Confidence Intervals	
Bottom	52.12 to 55.39
Top	99.01 to 100.7
LogEC50	-4.988 to -4.947
HillSlope	-5.305 to -3.617
EC50	1.028e-005 to 1.129e-005
Goodness of Fit	
Degrees of Freedom	86
R^2	0.9758
Absolute Sum of Squares	847.9
Sy.x	3.140
Number of points Analyzed	90

Figure A-15. Dose-response curve for **2-15a, 2-15b** effects in MDA-MB-231 wound closure. IC_{50} values were determined by nonlinear regression analysis with GraphPad prism software. It was calculated for inhibition of wound closure at 24 h post-wounding with normalization to parallel controls using at least 5 different subtoxic concentrations in concentration-response experiments. The calculated IC_{50} value for inhibition of wound closure at 24 h by **2-15a, 2-15b** is 10.8 μM.

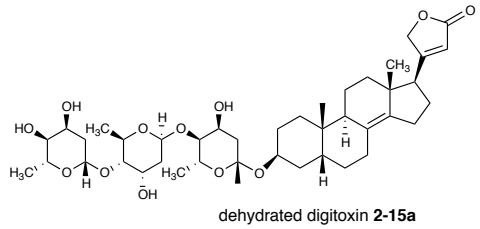

dehydrated digitoxin **2-15a**

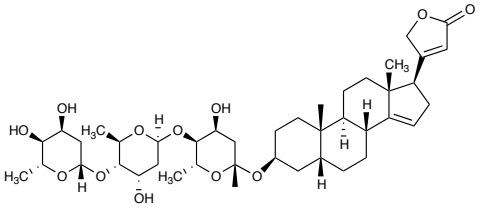

dehydrated digitoxin **2-15b**

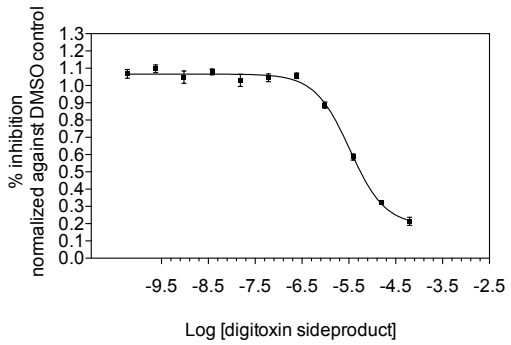

Sigmoidal dose-response (variable slope)	
Best-fit values	
Bottom	0.1898
Top	1.067
LogEC50	-5.477
HillSlope	-1.157
EC50	3.336e-006
Std. Error	
Bottom	0.03112
Top	0.009653
LogEC50	0.04949
HillSlope	0.1264
95% Confidence Intervals	
Bottom	0.1279 to 0.2516
Top	1.047 to 1.086
LogEC50	-5.575 to -5.378
HillSlope	-1.408 to -0.9054
EC50	2.660e-006 to 4.185e-006
Goodness of Fit	
Degrees of Freedom	95
R^2	0.9532
Absolute Sum of Squares	0.4693
Sy.x	0.07029
Number of points Analyzed	99

Figure A-16. Dose-response curve for digitoxin **2-15a, 2-15b** effect in *in vitro* Na^+/K^+ ATPase inhibition. IC_{50} values were determined by nonlinear regression analysis with GraphPad prism software. It was calculated with normalization to DMSO control. The calculated IC_{50} value for inhibition of the Na^+/K^+ ATPase activity by **2-15a, 2-15b** is 3.3 μM.

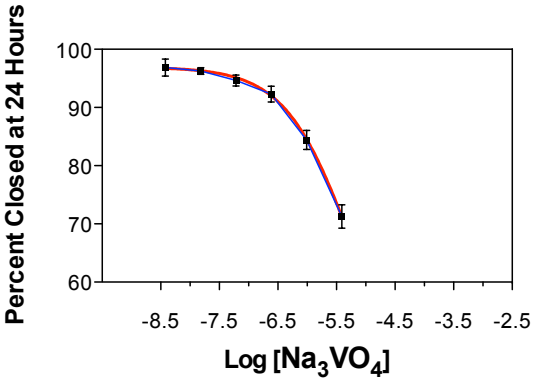

Sigmoidal dose-response (variable slope)	
Best-fit values	
Bottom	37.38
Top	96.91
LogEC50	-5.251
HillSlope	-0.7653
EC50	5.613e-006
Std. Error	
Bottom	78.49
Top	1.473
LogEC50	1.370
HillSlope	0.4393
95% Confidence Intervals	
Bottom	-120.4 to 195.2
Top	93.95 to 99.87
LogEC50	-8.005 to -2.497
HillSlope	-1.648 to 0.1179
EC50	9.892e-009 to 0.003185
Goodness of Fit	
Degrees of Freedom	50
R^2	0.8371
Absolute Sum of Squares	862.1
Sy.x	4.152
Number of points Analyzed	54

Figure A-17. Dose-response curve for Na_3VO_4 **2-16** effect in MDA-MB-231 wound closure. IC_{50} values were determined by nonlinear regression analysis with GraphPad prism software. It was calculated for inhibition of wound closure at 24 h post-wounding with normalization to parallel controls using at least 5 different subtoxic concentrations in concentration-response experiments. The calculated IC_{50} value for inhibition of wound closure at 24 h by **2-16** is 5.6 μM.

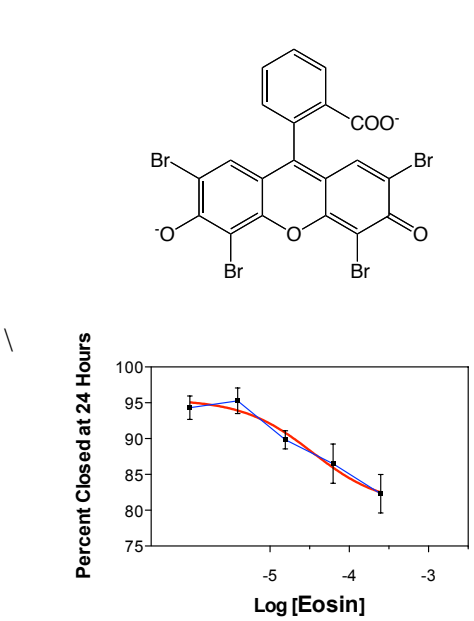

Sigmoidal dose-response (variable slope)	
Best-fit values	
Bottom	80.64
Top	95.49
LogEC50	-4.463
HillSlope	-0.9833
EC50	3.441e-005
Std. Error	
Bottom	6.457
Top	2.935
LogEC50	0.4537
HillSlope	0.9908
95% Confidence Intervals	
Bottom	-1.393 to 162.7
Top	58.21 to 132.8
LogEC50	-10.23 to 1.302
HillSlope	-13.57 to 11.61
EC50	5.914e-011 to 20.03
Goodness of Fit	
Degrees of Freedom	1
R^2	0.9689
Absolute Sum of Squares	3.650
Sy.x	1.910
Number of points	
Analyzed	5

Figure A-18. Dose-response curve for Eosin **2-17** effect in MDA-MB-231 wound closure. IC_{50} values were determined by nonlinear regression analysis with GraphPad prism software. It was calculated for inhibition of wound closure at 24 h post-wounding with normalization to parallel controls using at least 5 different subtoxic concentrations in concentration-response experiments. The calculated IC_{50} value for inhibition of wound closure at 24 h by eosin **2-17** is 34.4 μM.

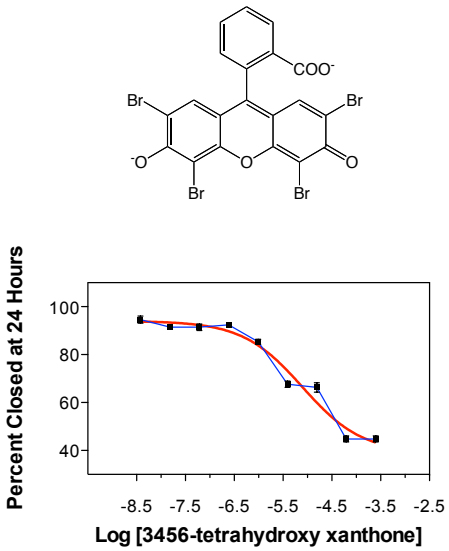

Sigmoidal dose-response (variable slope)	
Best-fit values	
Bottom	38.99
Top	94.03
LogEC50	-5.104
HillSlope	-0.7101
EC50	7.864e-006
Std. Error	
Bottom	3.428
Top	1.234
LogEC50	0.1067
HillSlope	0.1047
95% Confidence Intervals	
Bottom	32.15 to 45.82
Top	91.57 to 96.49
LogEC50	-5.317 to -4.892
HillSlope	-0.9189 to -0.5012
EC50	4.818e-006 to 1.284e-005
Goodness of Fit	
Degrees of Freedom	77
R^2	0.9334
Absolute Sum of Squares	2042
Sy.x	5.150
Number of points Analyzed	81

Figure A-19. Dose-response curve for **2-18** effect in MDA-MB-231 wound closure. IC_{50} values were determined by nonlinear regression analysis with GraphPad prism software. It was calculated for inhibition of wound closure at 24 h post-wounding with normalization to parallel controls using at least 5 different subtoxic concentrations in concentration-response experiments. The calculated IC_{50} value for inhibition of wound closure at 24 h by **2-18** is 7.86 μM.

Table A-1. *Small molecule hits from chemical genetics screening of Analyticon natural product compound library for inhibitors of MDA-MB-231 breast cancer cell migration*

Structure	**Plate number – Well number** **Analyticon Code** **Comments**
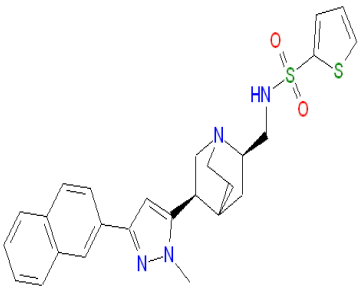	P2-G3 NAT13-338106 Toxic at 50µM
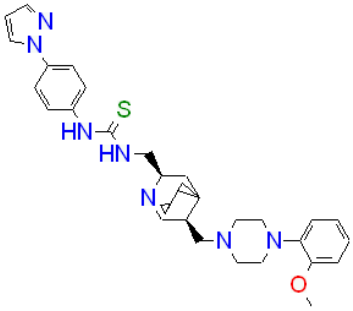	P2-G4 NAT13-339685 Not toxic (still open after 48 hrs)
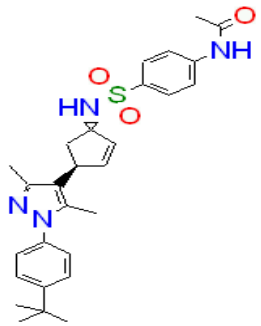	P2-H7 Not toxic (still wide open after 48 hrs)
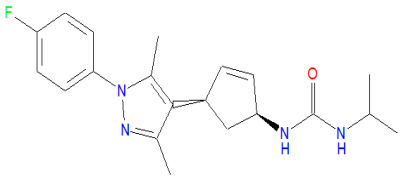	P4-A10 NAT6-321371 Not toxic

	P5-D2 NAT13-339050 Toxic at 50µM
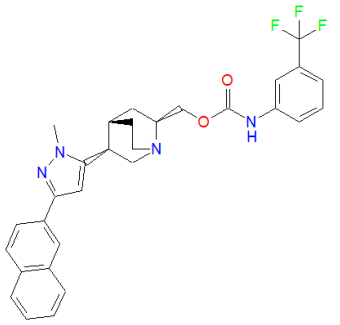	P5-E2 NAT-13338993 Toxic at 50µM
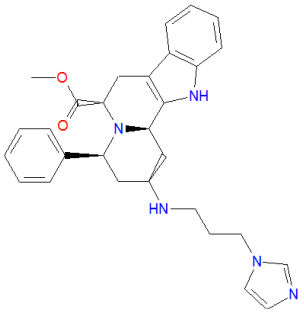	P5-E4 NAT-15-330225 Toxic at 50µM
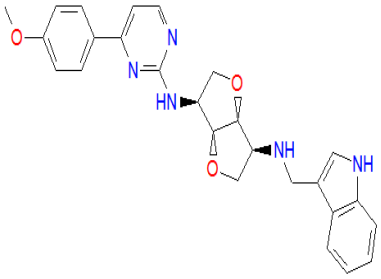	P5-D3 NAT16-653195 Not toxic
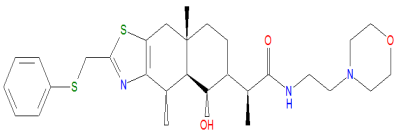	P5-A5 NAT16-653195 Not toxic
	P5-F4 Not toxic (still open after 48 hrs)

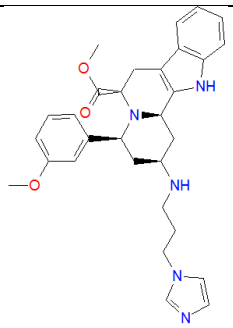	
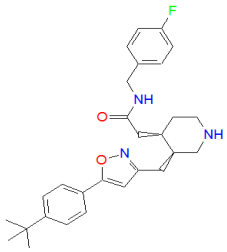	P6-A6 NAT14-350403 MIC – 6.25 µM; MLC – 12.5 µM Toxic at 50µM
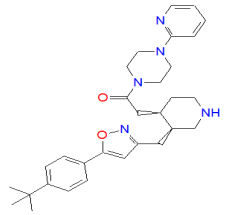	P6-B6 NAT14-350423 MIC – 6.25 µM; IC_{50} – 5.8 µM; MLC – 25 µM Toxic at 50µM
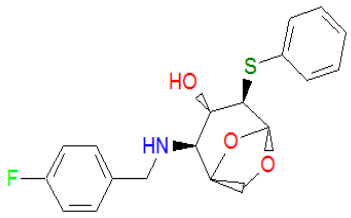	P6-A10 NAT17-346996 Not toxic
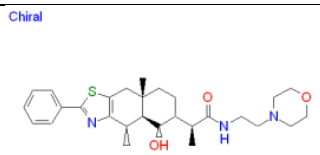	P7-A3 NAT5-257066 Not toxic (still open after 48 hr)

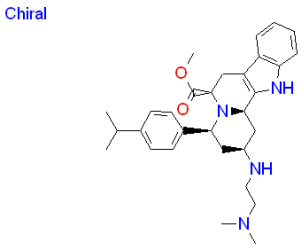	P7-A4 NAT15-330734 Not toxic (still open after 48 hr)
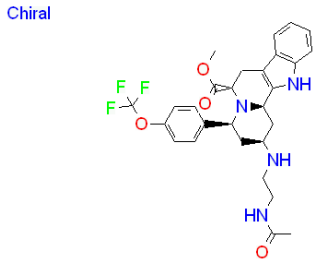	P7-B4 NAT15-330324 Not toxic (still open after 48 hr)
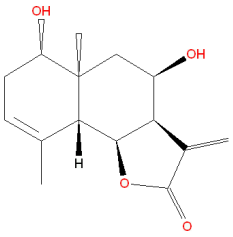	P8-A3 NP-009815 Not toxic
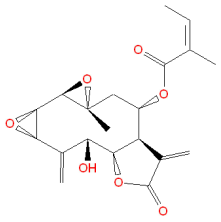	P8-A11 NP-004306 Toxic at 50 µM
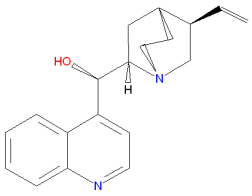	P8-B6 NP-010071 Not toxic (still wide open after 48hrs)
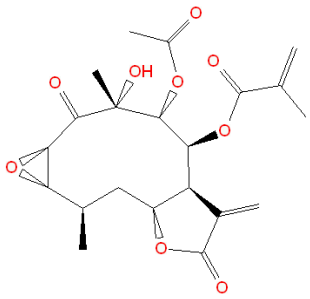	P8-C8 NP-002767 Toxic at 50 µM

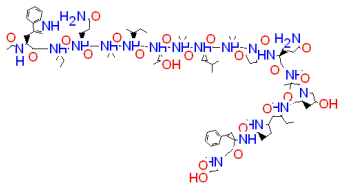	P8-E2 NP-005313 Not toxic
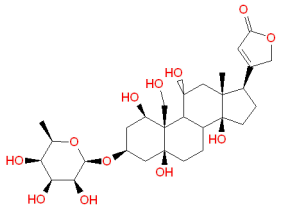	P8-E4 NP-000518; cardiac glycoside (ouabain) MIC – 61 nM; IC50 – 173 nM; MLC - >100µM Not toxic at 50 µM (still wide open after 48hrs)
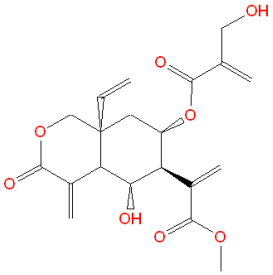	P8-F4 NP-000192 Not toxic (still wide open after 48hrs)
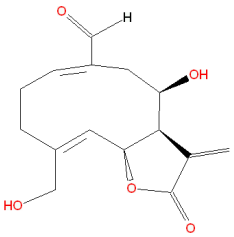	P8-H11 NP-009822 Toxic at 50 µM
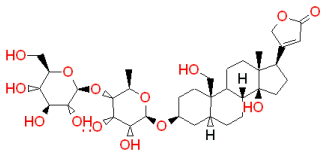	P9-H4 NP-005340; cardiac glycoside Active from 2µM Not toxic at 50µM (still wide open after 48hrs)
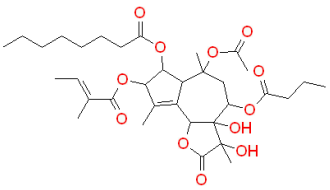	P8-H11 NP-009822 Active from 400 nM Toxic at 10 µM

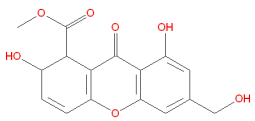	P9-E6 NP-001821 Toxic at 50 µM
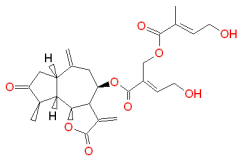	P9-B10 NP-009784 Toxic at 50 µM
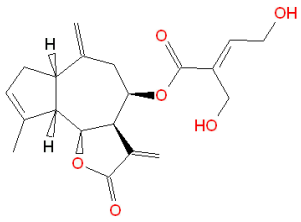	P9-B10 NP-009699 Toxic at 50 µM
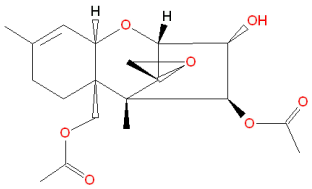	P9-E10 NP-002481 Active from 80 nM Not toxic at 50µM (still wide open after 48hrs)
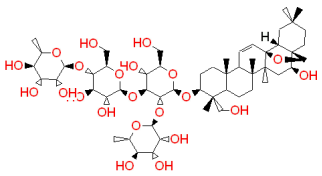	P9-G11 NP-008014 Toxic at 50 µM
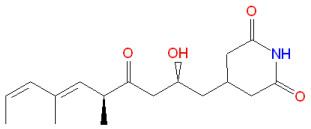	P9-A5 NP-006205 Not toxic
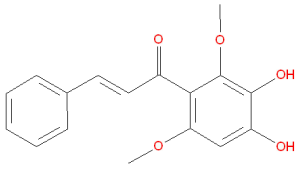	P9-A11 NP-009051 Not toxic (still wide open after 48hrs)
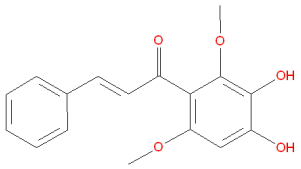	P9-A11 NP-009051 Not toxic (slightly open after 48hrs)

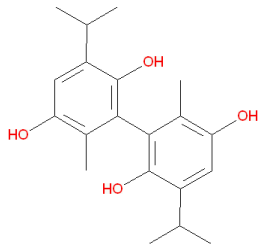	P9-C6 NP-003588 Toxic at 50 µM
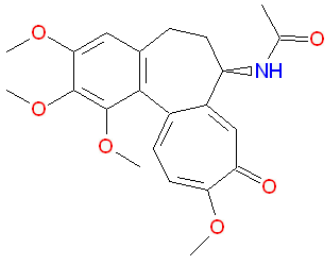	P9-D7 NP-010664; colchicine Active from 2µM Not toxic at 50µM (still open after 48hrs)
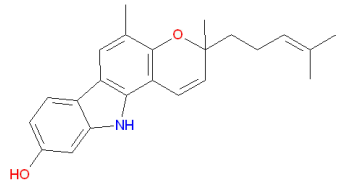	P9-E9 NP-011363 Toxic at 50 µM
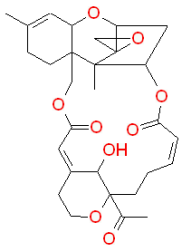	P10-G4 NP-012389 Not toxic (still wide open after 48hrs)
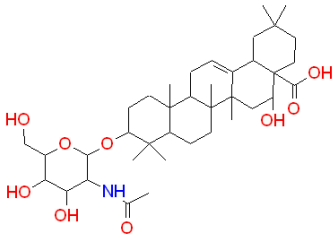	P10-H6 NP-012485 MIC – 1.5625 µM; IC_{50} – 3.8 µM; MLC – 12.5 µM Toxic at 50 µM
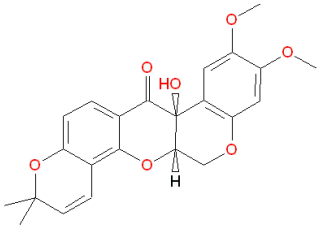	P10-G7 NP-004022 Not toxic (still wide open after 48hrs)

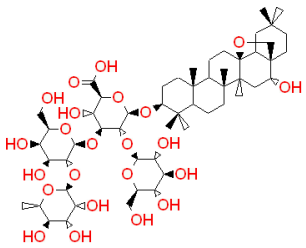	P10-A8 NP-000424 MIC – 3.125 µM; IC_{50} – 5.9 µM; MLC – 25 µM Toxic at 50 µM
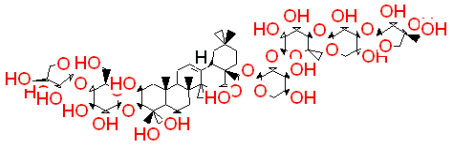	P10-D8 NP-007510 MIC – 3.125 µM; IC_{50} – 7.6 µM; MLC – 25 µM Toxic at 50 µM
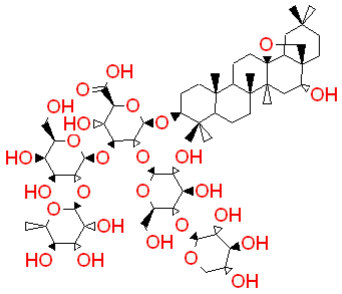	P10-F8 NP-000423 Not toxic (still wide open after 48hrs)
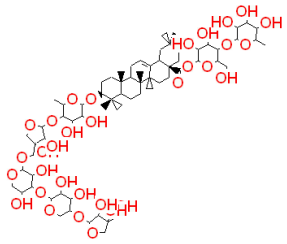	P10-C9 NP-005099; cardiac glycoside MIC - < 1.5625 µM; IC_{50} – 7.2 µM; MLC – 25 µM Toxic at 50 µM
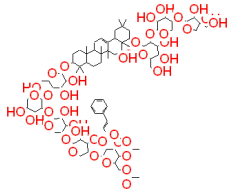	P10-C11 NP-008511; cardiac glycoside MIC - < 1.5625 µM; IC_{50} – 5.4 µM; MLC – 5.4 µM Toxic at 50 µM
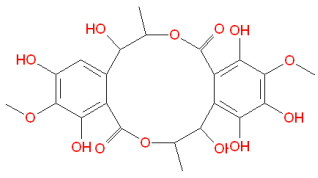	P10-A5 NP-007572 Not toxic

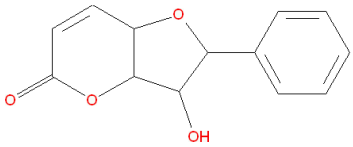	P10-E11 NP-012950 Not toxic (slightly open after 48hrs)
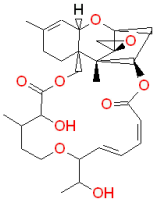	P11-F3 NP-012028 Not toxic (still wide open after 48hrs)
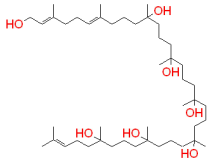	P11-G3 NP-006581 Toxic at 50 µM
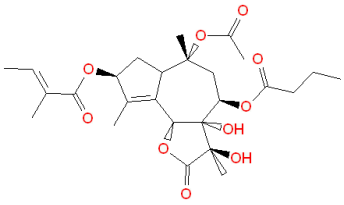	P11-F7 NP-001595 Active from 400 nM Toxic at 50, 10 µM
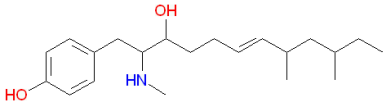	P11-H3 NP-008189 Toxic at 50 µM
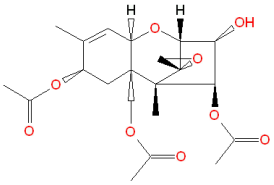	P11-G4 NP-002480 Active from 2µM Not toxic at 50µM (still wide open after 48hrs)
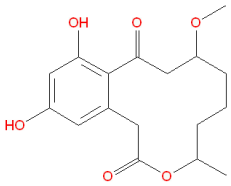	P11-C5 NP-005331; curvularin MIC – 3.125 µM; IC50 – 36 µM; MLC - > 50µM Not toxic at 50 µM (still wide open after 48hrs)

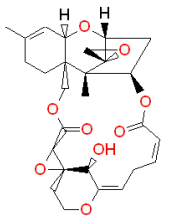	P11-F5 NP-012386 Not toxic (still wide open after 48hrs)
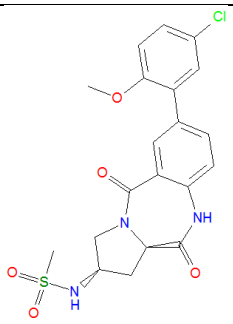	P4-G8 NAT3-210762 Not toxic